ABSTRACT

ELASHEGH, AHLAM E.A. Mathematical and Computational Mixture Models for Cartilage Regeneration in Cell-Seeded Scaffolds. (Under the direction of Dr. Mansoor Haider.)

Articular cartilage is an avascular and aneural biological soft tissue that has a limited capacity for growth and repair, and exhibits a high incidence of osteoarthritis with aging. Osteoarthritis can result in the appearance of osteochondral defects within the tissue layer or severe degradation of the cartilage extracellular matrix (ECM), necessitating joint replacement. Consequently, strategies and techniques for regeneration of cartilage ECM based on tissue engineering approaches are of great interest and potential importance. One common technique involves the seeding of specialized cells in biocompatible, porous scaffold materials. Mathematical models provide a theoretical framework within which coupling between biophysical, biochemical, biomechanical and physiological mechanisms can be quantified and analyzed as an alternative to, or in combination with, tissue engineering experiments which may be time intensive or costly.

A multiphasic continuum mixture model was developed for regeneration of cartilage ECM in the local environment of a single cell seeded within a scaffold. Model variables accounted for spatio-temporal evolution of solid displacement, fluid velocity, pore pressure, (bound) solid phases including scaffold and linked ECM, as well as (unbound) solutes in the interstitial fluid including unlinked ECM and growth factor. The model was specialized to the one-dimensional case of a single spherical cell surrounded by a spherical region that is a highly porous scaffold whose pores accumulate linked ECM as time evolves and the scaffold degrades. A product inhibition hypothesis was used to model cell-mediated biosynthesis of unlinked matrix proteins. Linking required to transform unlinked ECM into linked ECM was assumed to depend on both the growth factor concentration and the evolving porosity of the mixture. The latter relationship was modeled as a nonlinear, Gaussian function of evolving porosity in the extracellular region to account for phenomena of poor linking for very dilute scaffolds, and reductions in pore size with ECM accumulation that inhibit spatial distribution and ECM linking.

The resulting model consists of a system of partial differential equations in both the cell and extracellular regions along with boundary and interface conditions. A finite difference method was used to develop a numerical scheme that was implemented in MATLAB. Accuracy of temporal aspects of the scheme and its implementation were verified by developing an analytical series solution for a special case of the model that corresponds to a reaction-diffusion system on the extracellular region with a time-varying boundary condition capturing dynamic effects of the cell. Cartilage ECM regeneration in the local environment of a single cell was simulated numerically by first distinguishing between biophysical parameters, scaffold design parameters

and physiological parameters. Biophysical and scaffold parameter values were set based on the literature, while physiological values were calibrated to yield ECM regeneration on realistic time scales. Via a parametric analysis, simulations involving perturbations of this baseline case demonstrated sensitivity of tissue outcomes to both the level of initial scaffold porosity and to physiological parameters related to both the ECM linking model and the product inhibition hypothesis for cell-mediated biosynthesis. Based on the parametric analysis, a reduced model was also identified.

Mathematical and Computational Mixture Models for
Cartilage Regeneration in Cell-Seeded Scaffolds

by
Ahlam E.A. Elashegh

A dissertation submitted to the Graduate Faculty of
North Carolina State University
in partial fulfillment of the
requirements for the Degree of
Doctor of Philosophy

Applied Mathematics

Raleigh, North Carolina

2014

APPROVED BY:

_____   _____
Dr. Farshid Guilak   Dr. Ralph Smith

_____   _____
Dr. Zhilin Li   Dr. Mansoor Haider
                                                       Chair of Advisory Committee

DEDICATION

To my soulmate, my spouse, Hussein.

BIOGRAPHY

Ahlam Elashegh was born in Tripoli, Libya on April 12, 1973. She is a wife and a mother of three children. She attended schools in Tripoli, the capital city of Libya, until she received a Bachelor of Science in Mathematics from University of Tripoli. Ahlam worked as a high school teacher for two years before becoming a teacher's assistant in the Mathematics Department in University of Tripoli. In 2005, she was awarded her Master's degree in Mathematics from University of Tripoli and also become a faculty member in the Mathematics department at the University of Tripoli.

In 2007, Ahlam was awarded a scholarship from the Libyan government to purse a Ph.D. in Mathematics, and she chose the United States to be her country of study. She first joined a center focused on teaching English as a second language at the University of Arizona for about one year. In 2009, she moved to Raleigh, NC to join the Ph.D. program in the Mathematics Department at North Carolina State University, where she received another Master's degree in Applied Mathematics in 2010. Ahlam earned her Doctor of Philosophy degree in Applied Mathematics in the Fall of 2014 under the guidance of Dr. Mansoor Haider.

ACKNOWLEDGEMENTS

TABLE OF CONTENTS

LIST OF TABLES

LIST OF FIGURES

Chapter 1

Introduction and Background

1.1 Articular Cartilage

Articular cartilage is a biological soft tissue that is both avascular, in that it contains no blood vessels and aneural since it has no nerve endings. As a result, it has a limited capacity for growth and repair and these processes are predominantly regulated by the cells within the tissue. Articular cartilage is found mainly in diarthrodial joints such as shoulders, hips, and knees (Figure 1.1a). In healthy individuals, articular cartilage provides a resilient load-bearing surface for several decades. Cartilage is a multiphasic tissue in that its structure arises from an extracellular matrix (ECM), occupying roughly 15-20% of the tissue volume (Figure 1.1b). The ECM is saturated with interstitial fluid that comprises most of the remaining tissue volume, and contains dissolved ions, nutrients and other solutes that are vital for tissue health. Via ECM deformation, fluid pressurization, and fluid-sold drag during interstitial flow, this tissue facilitates load support and energy dissipation under compressive mechanical loading in joints [34]. Cartilage ECM consists of a cross-linked network of proteins with an embedded population of sparsely distributed cells, called chondrocytes. These cells occupy between 1-10% of the tissue volume, depending on age and other factors. Chondrocytes regulate their metabolic activity in response to biophysical and biomechanical cues in their local environment within the ECM. The associated physiological processes are of vital importance in cartilage primarily due to the fact that the tissue is avascular and aneural. The two primary ECM constituents are collagen and large macromolecules called proteoglycans (PGs) ($\approx$ 25%-35% by dry weight) that have a net negative charge. The collagen network is comprised of mostly type-II collagen ($\approx$ 60% by dry weight) which is neutrally charged with a fiber arrangement that is isotropic in the mid-zone but more parallel near the synovial interface and more normal near the bone. PGs, which are intertwined within the collagen network, are comprised of a hyaluronic acid protein core with negatively charged side chains consisting of sulfated glycosaminoglycans (GAGs),
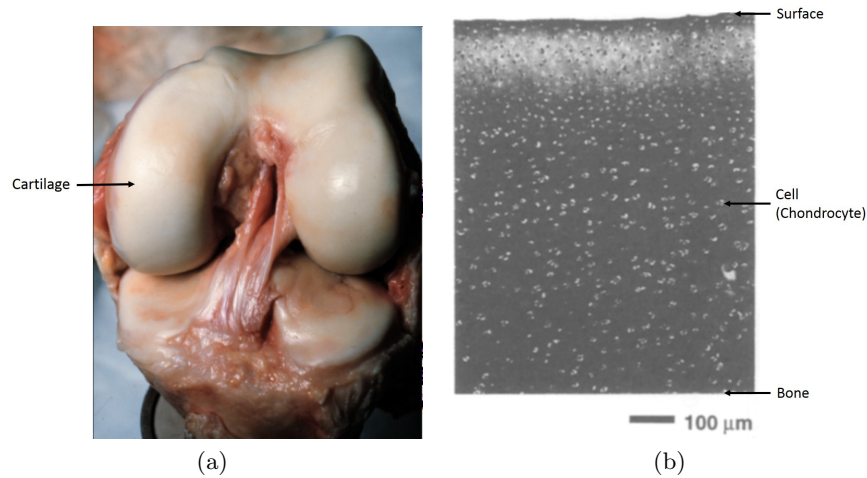
Figure 1.1: (a) Articular cartilage is a biological soft tissue that lines the surfaces of bones in diarthrodial joints, such as the knee. (b) Cross-section of a layer of articular cartilage, indicating the presence of sparsely distributed cells, called chondrocytes, which monitor and maintain the extracellular matrix. (Reprinted from Osteoarthritis and Cartilage, 2/2, Farshid Guilak, B. Christoph Meyer, Anthony Ratcliffe and Van C. Mow, The effects of matrix compression on proteoglycan metabolism in articular cartilage explants, 91-101, Copyright (1994), with permission from Elsevier).

keratin-sulfate, and chondroitin sulfate [12]. At the macroscopic scale of the tissue, the PGs give rise to a negative fixed charge density that enhances load support in compression via charge-to-charge repulsion and other osmotic effects. Since cartilage exhibits a low capacity for direct cellular communication, each chondrocyte is able to alter its metabolic activity using micro-environmental signals such as physical forces or soluble mediators such as growth factors and cytokines [68, 70], that are signaled to the cell via mechanosensitive ion channels or other receptors, such as G-protein coupled receptors [12, 20, 36].

1.2 Osteoarthritis

Millions of Americans each year experience cartilage damage caused by injury or diseases such as osteoarthritis (OA). While OA impacts most of the tissues within articulating joints, it most severely affects the articular cartilage. OA is a painful degenerative disease that is primarily associated with aging and leads to structural ECM degradation and fluid loss resulting in joint stiffness, decreased mobility and painful bone-on-bone contact necessitating joint replacement surgery. In OA, chondrocytes express higher levels of catabolic cytokines, decreasing synthesis of ECM constituents and increasing levels of degradative enzymes such as matrix metallino-

proteinases [51]. Along a joint surface, cartilage defects occurring due to injury or degradation lead to ECM erosion and joint degeneration [16, 39]. Often the ECM deteriorates beyond the point of self-repair as the disease progresses (Figure 1.2) [7].

| Normal | Early Disease | Late Disease |
| (a) | (b) | (c) |
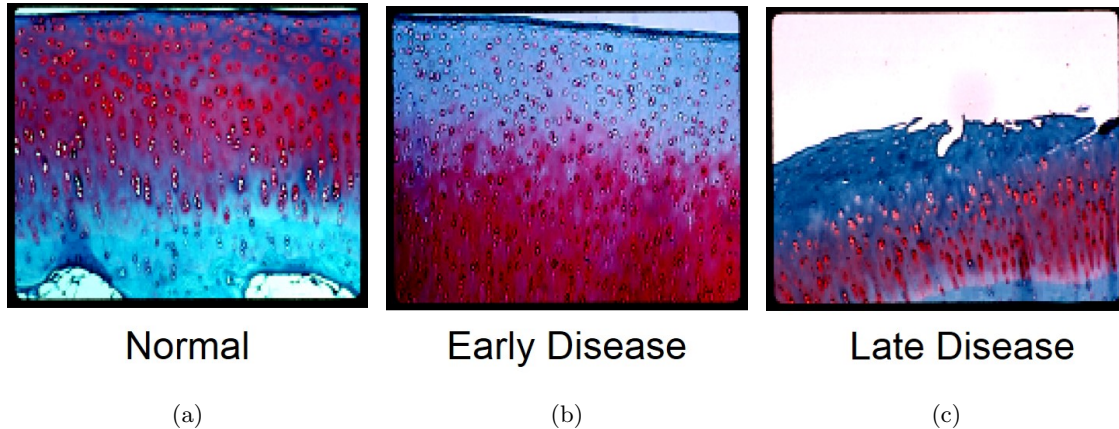
Figure 1.2: (a) In healthy articular cartilage proteoglycans are uniformly distributed in the upper portion of the tissue layer, as indicated by the red-purple staining. (b) In early OA, proteoglycan content decreases from the surface towards the bone, as shown by the loss of red-purple stain and structural degradation of the ECM follows. (c) A later stage of OA in which the tissue degrades beyond a point of self-healing. (Photos courtesy of Dr. Lori Setton, Cartilage Mechanics and Tissue Engineering Laboratory, Duke University.)

1.3 Cartilage Tissue Engineering

Due to the limited natural ability of articular cartilage for self-healing, a few surgical techniques have been developed to aid or stimulate cartilage repair within damaged tissue. Since these techniques are less-invasive surgical methods, they can be considered as an option prior to total joint replacement [38]. Two such techniques are microfracture and autologous chondrocyte implantation (ACI), but limited success has been seen with either therapy. In microfracture, the subchondral bone is drilled to induce migration of mesenchymal progenitor cells from the marrow to the lesion site to initiate ECM repair. In contrast, ACI involves the expansion of chondrocytes harvested from the patient that are expanded in cell culture and then transplanted to the defect site. In both of these therapies, the resulting tissue does not have the correct composition, structure or biomechanical properties, often leading to tissue overgrowth or the formation of a fibrocartilaginous scar tissue that has limited efficacy [1, 5, 38].

The field of cartilage tissue engineering has seen many advances in recent years and the development of associated mathematical models is the focus of this work. Cartilage tissue engineering involves the regeneration of cartilage ECM by seeding cells in a natural or synthetic biomaterial that acts as a three-dimensional scaffold with initial structural support for tissue growth, concurrent with scaffold degradation- see Figure 1.3 for an example. A primary functional outcome is the compressive elastic stiffness modulus of the tissue construct, which transitions from the initial scaffold elastic modulus of a few KPa in most hydrogel systems to a targeted range of approximately 0.5-1.0 MPa that is observed in mature articular cartilage [25, 30, 62]. There are many proposed natural and synthetic scaffold biomaterials that are amenable to initiation of cellular processes of differentiation, proliferation, migration, and degradation by proteolytic enzymes. Important scaffold properties known to influence outcomes include the porosity, affecting cell proliferation and ECM formation, and permeability, which affects convective transport of nutrients and metabolic waste [5, 26, 40, 61, 62].

Once seeded in a biocompatible scaffold, cells will initiate biosynthesis and secretion of proteins that are initially dissolved in the interstitial fluid and serve as the ECM building blocks. These proteins initially become entrapped in the chains of the hydrogel. As the hydrogel begins to degrade, cellular up-regulation of matrix protein biosynthesis occurs, transport of smaller proteins and nutrients is sustained and crosslinked ECM can form [12, 27]. Initially, the soluble side chains of PG are synthesized and then, subsequently cross-linked to other matrix molecules. Similarly, chondrocytes synthesize soluble procollagen as a precursor to later be assembled into the collagen network [12, 21]. Cross-linkers include families of matrilins, small leucine rich proteins, thrombospondins, and transglutaminases [20, 63]. It has been show that a high local PG concentration will exert negative feedback on further matrix production [8], but the process by which the chondrocyte senses local PG concentration is not known and could be mechanical or through a receptor signaling pathway. By culturing cell-seeded scaffolds for many weeks to few months, samples can be extracted at various time points and chemically stained for histological analysis of ECM content and organization. Staining assays include Safranin-O or Alcian Blue for GAG/PG, which can be used in combination with Fast-green FCF/Hematoxylin counterstain or Picrosirius Red to image collagen and cell nuclei [52].

Tissue engineering of functional cartilage, with a correct combination of biomechanical properties, biomechanical content and ECM structure, depends on several diverse factors including scaffold properties, cell type, initial cell seeding density, mechanical stimulation, and chemical stimulation (culture medium and growth factors) [14, 26, 49, 62]. The two main choices for cell type are adult (mature) chondrocytes and stem cells [24]. Chondrocytes exhibit low yield when harvested, can be difficult to culture and when expanded, produce ECM constituents, but often lose their phenotype and chondrogenic potential over time [15, 66]. Mesenchymal stem cells (MSCs) differentiate into chondocytes and are easily accessible and expanded from
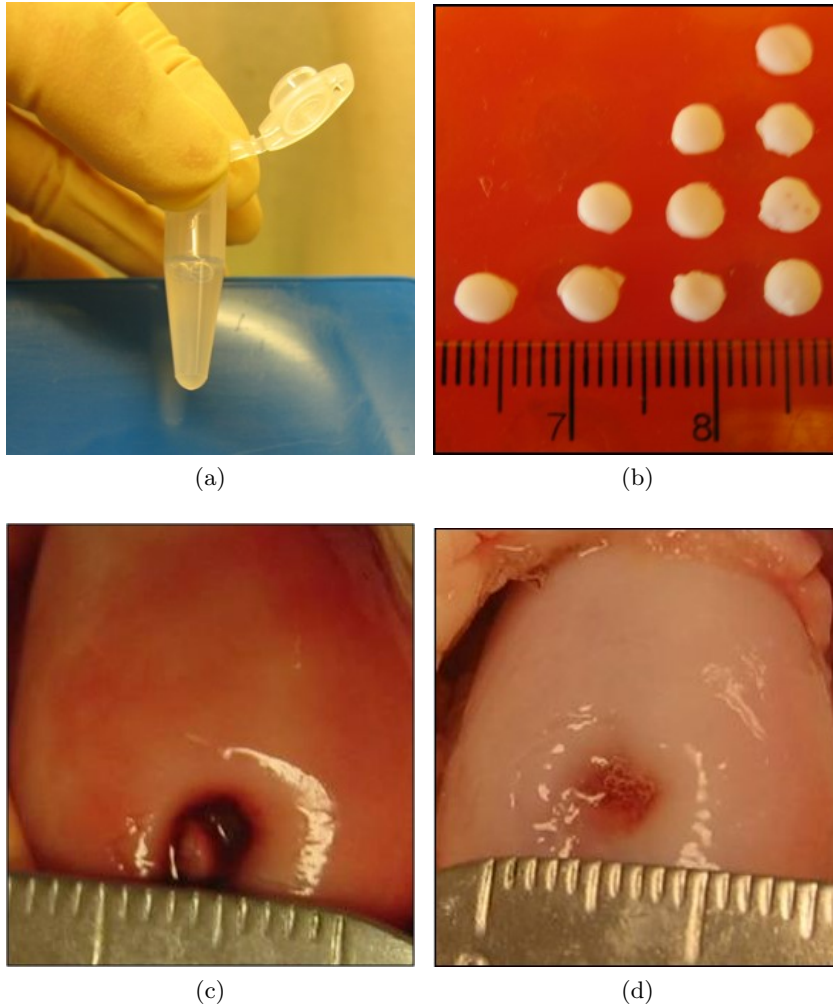
Figure 1.3: Illustration of the tissue engineering process. (a) Cells are mixed into a solution of elastinlike polypeptide (ELP) hydrogel scaffold polymers, (b) Tailored design of the scaffold polymer enables a phase transition from liquid to a gel at physiological temperatures, (c) Image of an osteochondral defect, (d) An osteochondral defect with implanted cell-biomaterial scaffold. (Reprinted from Tissue Engineering Part A, 15/8, Dana L. Nettles, Ashutosh Cilkoti, and Lori A. Setton, Early metabolite levels predict long-term matrix accumulation for chondrocytes in elastin-like polypeptide biopolymer scaffolds, 2113-2121, Copyright (2009), with permission from Mary Ann Liebert, Inc.)

bone marrow, fat, and the synovium [14]. While mechanical properties of MSC-based constructs are often lower than those using primary chondrocytes, MSCs are readily accessible without causing further cartilage damage [23]. Increased mechanical properties could potentially be achieved with an optimal combination of initial scaffold properties, timing of growth factors and mechanical stimulation [25, 36]. Adult stem cells have been successfully grown in multiple types of biomaterials, maintaining chondrocyte phenotype and forming cartilaginous tissue [18].

1.4   Mathematical Modeling Approaches

The potential role of mathematical modeling in the design of engineered cell-scaffold systems has been the subject of several studies [13, 44, 54, 55]. There are some similarities with wound healing models [37, 45, 59, 71], which also consider cell-ECM interactions accounting for angiogenesis, but these interactions are quite different in articular cartilage since it is avascular and exhibits much less cell movement. Similarly, many models of tumor formation simulate developmental growth of new tissue and account for factors such as cell viability and nutrient transport, but these models are also focused on vascular tissue and/or more fluid-based modeling approaches [4, 33, 47, 50, 60]. Properties that are unique to cartilage regeneration include its avascular nature, its stiff and negatively charged ECM, and the macroscopic solid mechanical properties that ultimately determine the success of engineered tissue functional outcomes.

Initial models of ECM accumulation or cell growth in conjunction with degradation of polymeric scaffolds used compartmental (ODE) models [53, 67, 69]. For example, Wilson et al. [69], formulated two elementary, decoupled ODEs to capture ECM synthesis via a logistic-type model for ECM product inhibition and a simple exponential decay model for scaffold degradation. Spatio-temporal partial differential equation (PDE) models have mostly been based on a system of reaction-diffusion equations. These include 1D reaction-diffusion models with one bound and one soluble ECM component in Cartesian coordinates [10], and a 1D radial model of the local chondrocyte environment that incorporated advection [65]. Olson and Haider [46] developed a two-zone reaction-diffusion model of a cartilage defect filled with a scaffold, representing the gel-tissue interface as a moving boundary using a level-set method. Obradovic et al. [44] developed a 2D reaction-diffusion model for a rotating bioreactor with local oxygen and GAG concentrations as primary variables and using Michaelis-Menten kinetics. Similar reaction-diffusion models have been developed to account for cellular consumption of nutrients and synthesis of matrix constituents [43, 56, 57, 58, 65]. In particular, Sengers et al. [57], developed both a compartmental model and a separate model with a single mass balance equation to capture effects of dynamic loading on chondrocyte metabolism via calibration with experimental data for GAG synthesis. Haugh [22] developed a spatio-temporal PDE model combining a level set approach with a system of reaction-diffusion equations for modeling a single cell in

the local environment of a hydrogel scaffold, but did not employ a formulation accounting for mixture effects.

The models outlined above cannot, inherently, account for the role of evolving porosity as cell-synthesized ECM forms and begins to accumulate in the pores of the scaffold. Mixture continuum models provide a natural framework for delineating multiple time-varying system constituents (phases). They also intrinsically distinguish between measures such as dry mass, wet mass, solute concentrations, and intrinsic vs. apparent densities of bound constituents. In this context, mixture approaches to date have included models for tissue growth based on porous flow mixture theory to study cell mobility and aggregation in a porous scaffold [29], as well as a homogenized scalar model for cell growth with advective and diffusive transport [9]. It should also be noted that mixture frameworks have been used in modeling growth of vascular tumors [6], biofilms [72], and in modeling morphogenesis [31, 32] where, in both cases, fluid flow and pressure are the primary quantities of interest. Mixture modeling for cartilage tissue engineering has seen only limited development and is ripe for further investigation. A detailed mixture model of cartilaginous tissue growth was published in 2009 by Ateshian et al. [3]. In its application to cartilage tissue engineering, this model accounted for cell division, and osmotic effects arising due to changes in fixed charge density with proteoglycan (PG) accumulation. However, this study did not account for unbound ECM constituents and its application to cartilage was limited to quasi-static conditions based on an analytical homogenization assumption. In 2011, Haider et al. [19] developed a compartmental model of cartilage regeneration in a cell-seeded scaffold, by extending the much simpler two-variable model of Wilson et al. [69] to the mixture framework. The model developed therein is briefly summarized in section 2.2. This mixture model tracks the average apparent densities (mass of phase/mixture volume) of the three phases: bound scaffold (Sc), unbound unlinked matrix (UM) and bound linked matrix (LM). Since linked ECM apparent density is correlated to tissue elastic stiffness, this model suggests that key functional outcomes depend nonlinearly on initial properties of the cell-biomaterial system and can aid in optimal system design. While this compartmental model, which is summarized in section 2.2, captures some features of cartilage regeneration in cell-seeded scaffolds, many important aspects of the problem were neglected. These include spatial effects, cell growth and proliferation, diffusive and advective transport of nutrients, growth factors and cell-synthesized proteins, and the capacity of deformation to enhance tissue regeneration.

To date, no PDE mixture models accounting for evolution of linked ECM, unlinked ECM and regulation of biosynthetic activities by cells have been developed in the context of cartilage tissue engineering. However, the 2003 modeling study by Mauck et al. [35] and the 1999 modeling study by Sun et al. [64] developed multiphasic continuum mixture models accounting for dissolved solutes. In particular, this model formulation was used in [35] to demonstrate that dynamic compressive loading can enhance the transport of neutral solutes in a porous permeable gel,

i.e. with no cells. While their study did not model active biological phenomena, it provides an excellent starting point for the new mixture models that will serve as the foundation of this dissertation.

The primary goal of this dissertation is to extend the ODE mixture model developed in [19] to the spatio-temporal (PDE) framework within the context of multiphasic continuum mixture theory. The details of this extension are developed in Chapter 2. The general formulation in Chapter 2 is then specialized to a one-dimensional spherical formulation in Chapter 3 and used to develop a model of cartilage ECM regeneration in the local environment of a single cartilage cell (chondrocyte), idealized as a sphere, that is seeded in a porous scaffold material. In Chapter 4, a numerical solution scheme is developed and implemented in MATLAB, based on use of the finite difference method applied to a nondimensionalized form of the governing equations. An analytical solution for a simplified case of the model, that reduces to a reaction-diffusion system, is also developed in Chapter 4 and used to verify accuracy and convergence rate. In Chapter 5, the model and numerical scheme developed in Chapters 3-4 are applied to simulate cartilage ECM regeneration in the local environment of a single cell. Model parameters are delineated into categories of biophysical, scaffold design and physiological parameters and their values are fixed or calibrated to formulate a baseline case representative of cartilage regeneration on realistic time scales. Perturbation of the baseline case is then considered in a parametric analysis to demonstrate a few key effects of scaffold design and physiological parameters on cartilage ECM regeneration, focusing on the effect of porosity. Lastly, based on the results of this parametric analysis, a reduced model is identified.

Chapter 2

Development of a Spatio-Temporal Mixture Model for Cartilage ECM Regeneration

2.1 Introduction

Cartilage structure arises from a dense extracellular matrix (ECM) comprised of collagen fibers and proteoglycan macromolecules that is saturated by interstitial fluid. Biphasic (fluid-solid) continuum mixture models of articular cartilage can account for partitioning between fluid pressurization and ECM deformation, as well as energy loss due to fluid-solid drag that occur during load bearing. While such mixture models describe biomechanical deformation, they do not account for active biological or physiological mechanisms in a natural or a tissue engineered cartilage system.

To date, only a few studies have considered extensions of the mixture modeling approach that account for mechanisms such as active cellular responses or cell-matrix interactions that are needed to model cartilage regeneration. A detailed mixture model of cartilagenous tissue growth was published in 2009 by Ateshian et al. [3]. While this study distinguished between charged and uncharged ECM constituents, it did not account for unbound ECM constituents explicitly. Its application to modeling cartilage growth was also limited to the quasi-static case and based on an analytical homogenization assumption. In 2011, Haider et al. [19] developed a temporal model of cartilage ECM regeneration in a cell-seeded scaffold based on a system of ordinary differential equations (ODEs). This model extended the much simpler two variable model of Wilson et al. [69] to the mixture framework by accounting for mixture volume fractions of bound and unbound ECM constituents in addition to the scaffold.

The primary goal of this work is to extend the temporal ODE model described above to

a spatio-temporal (PDE) model within the framework of continuum mixture theory. Spatio-temporal models have mostly been based on a system of reaction-diffusion equations. These models include 1D reaction-diffusion models with one bound and one soluble ECM component in Cartesian coordinates [10], and a 1D radial model of the local chondrocyte environment that incorporated advection [65]. Olson and Haider [46] developed a two-zone reaction-diffusion model of a cartilage defect filled with a scaffold, representing the gel-tissue interface as a moving boundary using a level-set method. Obradovic et al. [44] developed a 2D reaction-diffusion model for a rotating bioreactor with local oxygen and GAG concentrations as primary variables and using Michaelis-Menten kinetics. Similar reaction-diffusion models have been developed to account for cellular consumption of nutrients and synthesis of matrix constituents [43, 56, 58, 57, 65]. In particular, Sengers et al. [57] developed both a compartmental model and a separate model with a single mass balance equation to capture effects of dynamic loading on chondrocyte metabolism via calibration with experimental data for GAG synthesis. Overall, the PDE models outlined above cannot, inherently, account for the role of evolving porosity in the engineered cartilage system.

One relevant study was published in 2003 by Mauck et al. [35]. In this study, a multiphasic continuum mixture model was formulated to evaluate and demonstrate that dynamic compressive loading can enhance neutral solute transport in a (passive) porous permeable gel. While their study did not account for active biological effects, it provides a starting point for the development of new spatio-temporal PDE models of cartilage regeneration within the framework of continuum mixture theory. In this chapter, the temporal ODE mixture model [19] is briefly reviewed and then its extension to a spatio-temporal setting is developed.

2.2   Temporal Mixture Model of Cartilage Regeneration

This model tracks the (spatially) averaged apparent densities of three phases: bound scaffold (Sc), unbound unlinked matrix (UM) and bound linked matrix (LM) [19], assuming a homogenized mixture of these constituents. As in [69], a simple scaffold degradation model is used but cell-mediated ECM biosynthesis and linking are modeled using two separate differential equations.

2.2.1   Mixture Variables

The mixture volume is denoted by V for a tissue construct that is idealized to be a fluid-solid mixture. The mixture is assumed to be saturated so that $V = V^\omega + V^s$, where V^ω and V^s denote the volume of the fluid and solid phases, respectively. The average solid volume fraction is denoted by $\bar{\phi}^s = V^s/V$ and the average porosity is denoted by $\bar{\phi}^\omega = V^\omega/V$. The volume

occupied by unbound constituents that are dissolved in the interstitial fluid is assumed to be negligible (i.e. $V^{UM} \approx 0$) resulting in the relation:

$$\bar{\phi}^{\omega} + \bar{\phi}^s = 1, \tag{2.1}$$

The (bound) solid phase of the mixture is separated into three sub-phases. These are the linked ECM (LM), the scaffold (Sc) and the cells (c), i.e. $V^s = V^{LM} + V^{Sc} + V^c$. As noted earlier, the volume occupied by the unlinked ECM is neglected ($V^{UM} \approx 0$). This approximation is based on the assumption that the unlinked ECM is a dilute solute within the interstitial fluid solution. As a result, the solid phase volume fraction in the mixture can be expressed as

$$\bar{\phi}^s = \bar{\phi}^{LM} + \bar{\phi}^{Sc} + \bar{\phi}^c, \tag{2.2}$$

where the cell volume fraction $\bar{\phi}^c$ is assumed to be constant. It is also important to note that in mixture models apparent densities within the mixture, denoted by $\bar{\rho}^{\alpha}$, are related to the volume fractions by:

$$\bar{\rho}^{\alpha} = \frac{m^{\alpha}}{V} = \bar{\phi}^{\alpha} \rho_T^{\alpha}, \quad \alpha = c, LM, Sc, \tag{2.3}$$

where ρ_T^{α} and m^{α} are the true density and the mass of constituent α, respectively. Note that $0 \leq \bar{\rho}^{\alpha} \leq \rho_T^{\alpha}$.

2.2.2 Biosynthesis, Degradation and Linking

The degradation of total scaffold mass m^{Sc} is modeled by the equation

$$\frac{dm^{Sc}}{dt} = -k_{Sc} m^{Sc}, \tag{2.4}$$

where k_{Sc} is the scaffold degradation rate.

The cell-scaffold system is assumed to have a constant cell volume fraction $\bar{\phi}^c$ and a continuous mass supply of nutrients or growth factors. In the temporal model, diffusive time scales of these constituents are assumed to be fast relative to other time scales in the system. As a result, the concentration of nutrients or growth factors in the system is modeled to be both spatially and temporally constant, with the value of this concentration denoted as N^*. The following equation was used to model evolution of unlinked ECM mass in the system:

$$\frac{dm^{UM}}{dt} = V^c N^* \bar{\phi}^{\omega} k_{UM} \left(\bar{\rho}_{UM}^{\omega} - \frac{m^{UM}}{V^{\omega}} \right) - f(\bar{\phi}^s) \left(\bar{\rho}_{UM}^{\omega} - \frac{m^{UM}}{V^{\omega}} \right) m^{UM}, \tag{2.5}$$

where k_{UM} is the unlinked ECM synthesis rate that is mediated by the cells. This production of unlinked ECM is assumed to continue until an average critical solute concentration $\bar{\rho}_{UM}^{\omega}$

is reached. This assumption is based on the observation that, in engineered cartilage systems, product inhibition is known to occur and results in slowing down of cell-mediated ECM biosynthesis as ECM accumulates [8]. Based on the mixture formulation, the specific hypothesis used in the temporal model is that the cells detect the concentration of unlinked ECM in the interstitial fluid to regulate ECM biosynthesis. The second term in (2.5) models the removal of unlinked ECM from the system as it is assembled into (bound) linked ECM. This process is also assumed to be regulated by the cells in the identical manner to the biosynthesis of unlinked ECM. The remaining parts of the second term in (2.5) account for the fact that unlinked ECM mass will be removed in proportion to the amount of unlinked ECM mass present in the system, and based on a linking rate f that is assumed to depend only on the evolving porosity in the system.

The evolution of linked ECM mass is assumed to occur only by accumulation, via transformation, of unlinked ECM, leading to the model:

$$\frac{dm^{LM}}{dt} = f(\bar{\phi}^s)\left(\bar{\rho}^{\omega}_{UM} - \frac{m^{UM}}{V^{\omega}}\right)m^{UM}. \tag{2.6}$$

Linking rates in the system are modeled as following a Gaussian distribution with respect to porosity (expressed in terms of solid phase volume fraction):

$$f(\bar{\phi}^s) = k_{UL}e^{\frac{-(\bar{\phi}^s - \bar{\phi}^s_*)^2}{2\sigma^2}}, \tag{2.7}$$

where k_{UL} is the maximum linking rate, occurring when $\bar{\phi}^s = \bar{\phi}^s_*$. The mathematical form in (2.7) was chosen to simultaneously reflect the following properties of the system: (i) that the ability for formation of linked ECM in the system is enhanced as a solid network of fibers forms and facilitates cell attachment and guidance of biopolymer network assembly, and (ii) that as the porosity ($\bar{\phi}^{\omega} = 1 - \bar{\phi}^s$) decreases beyond a critical point, the decreasing average pore size in the network inhibits the ability of unlinked ECM to assemble and form linked ECM within the tissue construct.

2.2.3   Summary of Temporal Mixture Model

Using the relations in (2.3), the governing equations for the temporal (ODE) mixture model of cartilage ECM regeneration are written in terms of the average apparent densities as

$$\frac{d\bar{\rho}^{Sc}}{dt} = -k_{Sc}\bar{\rho}^{Sc}, \tag{2.8}$$

$$\frac{d\bar{\rho}^{UM}}{dt} = \bar{\phi}^C N^* \bar{\phi}^{\omega} k_{UM}\left(\bar{\rho}^{\omega}_{UM} - \frac{\bar{\rho}^{UM}}{\bar{\phi}^{\omega}}\right) - f(\bar{\phi}^s)\left(\bar{\rho}^{\omega}_{UM} - \frac{\bar{\rho}^{UM}}{\bar{\phi}^{\omega}}\right)\bar{\rho}^{UM}, \tag{2.9}$$

$$\frac{d\bar{\rho}^{LM}}{dt} = f(\bar{\phi}^s) \left(\bar{\rho}_{UM}^{\omega} - \frac{\bar{\rho}^{UM}}{\bar{\phi}^{\omega}} \right) \bar{\rho}^{UM}. \tag{2.10}$$

Assuming that ECM synthesis starts at $t = 0$, the initial condition for scaffold density is formulated in terms of the average initial scaffold porosity $\bar{\phi}_0^{Sc}$ and the scaffold polymer true density, resulting in the following set of initial conditions:

$$\bar{\rho}^{UM}(0) = 0, \quad \bar{\rho}^{LM}(0) = 0, \quad \bar{\rho}^{Sc}(0) = \bar{\phi}_0^{Sc} \rho_T^{Sc}. \tag{2.11}$$

Since linked ECM apparent density is correlated to tissue elastic stiffness, this model provides an initial description that quantifies the manner in which a key functional outcome might depend, nonlinearly, on initial properties of the cell biomaterial system. The development of models with this property can contribute to the optimal design of engineered cartilage systems.

While the compartmental model (2.8)-(2.11) captures some essential features of cartilage regeneration in cell-seeded scaffolds, many important aspects of the problem were neglected. These include spatial effects, cell growth and proliferation, diffusive and advective transport of nutrients, growth factors and cell synthesized proteins. An extension of this compartmental mixture model to the spatio-temporal (PDE) case is required for a more detailed characterization of cartilage regeneration in cell-seeded scaffolds.

2.3 Spatio-temporal (PDE) Mixture Model

In this section, a framework for developing mathematical models that govern interactions among biomechanical, biophysical, chemical and physiological phenomena during cartilage regeneration in cell-seeded scaffolds will be provided. Examples of biomechanical mechanisms considered include ECM deformation, interstitial fluid flow, fluid pressurization and energy loss due to fluid-solid drag. Biophysical phenomena considered include diffusive and convective transport of solutes dissolved within the interstitial fluid. Chemical models will account for scaffold degradation and transformation of unlinked ECM into linked ECM, while physiological phenomena include cell-mediated biosynthesis of unlinked ECM constituents as well as regulation of ECM cross-linking.

2.3.1 Mixture Formulation

In extending the mixture formulation to account for spatial effects, denote the mass, volume, and number of moles of phase α by m^α, V^α, and n^α respectively, where α indicates the water (solvent) phase, or a specific phase of a bound solid constituent or an unbound solute within the mixture. The total volume of the mixture is denoted by $V = \sum_\alpha V^\alpha$ and the following quantities are defined in differential form over infinitesimal volumetric regions within a continuum mixture

model of the biomaterial. Following the notation used by Mauck et al. [35], define the volume fractions within the mixture as:

$$\phi^\alpha = \frac{dV^\alpha}{dV}, \quad \alpha = \omega, s, f, \tag{2.12}$$

where the subscripts and superscripts ω, s, and f denote the solvent phase, solid phase, and solute phase, respectively. Apparent densities are defined as the mass of a phase per unit volume of the mixture:

$$\rho^\alpha = \frac{dm^\alpha}{dV}, \quad \alpha = \omega, s, f, \tag{2.13}$$

while the true density of each phase is its mass per unit volume of the same phase:

$$\rho_T^\alpha = \frac{dm^\alpha}{dV^\alpha}, \quad \alpha = \omega, s, f. \tag{2.14}$$

For (unbound) solutes in the mixture, concentrations can be defined based on the mixture volume as:

$$\tilde{c}^\alpha = \frac{dn^\alpha}{dV}, \quad \alpha = \omega, f, \tag{2.15}$$

or based on the solvent volume as:

$$c^\alpha = \frac{dn^\alpha}{dV^\omega}, \quad \alpha = f, \tag{2.16}$$

where n^α represents the number of moles of phase α. The molecular weight of phase α in the mixture is then given by:

$$M_\alpha = \frac{dm^\alpha}{dn^\alpha} \quad \alpha = f. \tag{2.17}$$

The molecular weight and true density are constant for a given phase α and each phase is assumed to be intrinsically incompressible. Based on these properties, the following relations hold among the variables defined above:

$$\sum_\alpha \phi^\alpha = 1, \quad \rho^\alpha = \phi^\alpha \rho_T^\alpha, \quad \tilde{c}^\alpha = \phi^\omega c^\alpha = \frac{\rho^\alpha}{M_\alpha}. \tag{2.18}$$

Therefore, in models developed based on this formulation of mixture variables, concentrations and volume fractions can be used as primary variables as an alternative to apparent densities for each of the phases in the mixture.

2.3.2   Primary Variables

A model is now developed for cartilage regeneration within the framework of the mixture variables outlined in the previous section. A new notation is adopted in which the superscript

14

s indicates the solid phase, the superscript α indicates an unbound solute phase, and the superscript β denotes a bound solid phase. As in the temporal (ODE) model, the mixture is assumed to be saturated, so that $V = V^\omega + V^s$ and $\phi^\omega + \phi^s = 1$, and the solutes are assumed to occupy negligible volume so that $V^\alpha \approx 0$ and $\phi^\alpha \approx 0$.

The primary variables in such a system are now summarized. Biomechanical variables traditionally associated with biphasic continuum mixture models of cartilage deformation include the solid phase displacment $\mathbf{u}^s$, fluid phase velocity $\mathbf{v}^\omega$, pore pressure p of the interstitial fluid and the water volume fraction ϕ^ω. The evolution of bound constituents is tracked by volume fractions ϕ^β, with the choice of specific constituents (number of β's) depending on the desired complexity of the model under consideration. Examples of such constituents include the scaffold, linked ECM constituents (e.g. collagen, PG), and cells attached to the ECM or scaffold. Under deformation, such bound constituents are assumed to move together with the solid phase velocity $\dot{\mathbf{u}}^s \equiv \partial_t \mathbf{u}^s$. Similarly, the number of unbound constituents to be considered (number of α's) depends on the complexity of the model and is tracked via both concentations c^α and velocities $\mathbf{v}^\alpha$ in the mixture. Examples of unbound constituents include nutrients and growth factors, cell-synthesized ECM proteins (prior to assembly and cross-linking), and metabolic waste products subsequent to ECM or scaffold degradation.

2.3.3 Governing Equations

The governing equations are formulated by considering balance of mass, balance of momentum and by assuming that the mixture is saturated and that its phases are intrinsically incompressible.

Mass balance of water, which is a biologically passive constituent, is written in the standard form

$$\partial_t \rho^\omega + \nabla \cdot (\mathbf{v}^\omega \rho^\omega) = 0. \tag{2.19}$$

For each bound constituent β, a mass balance equation is written assuming that the motion follows that of the solid phase s and that biological interactions are governed by a constitutive model F^β involving bound and unbound constituents and porosity so that

$$\partial_t \rho^\beta + \nabla \cdot (\dot{\mathbf{u}}^s \rho^\beta) = F^\beta(\rho^\omega, \{\rho^\beta\}, \{\rho^\alpha\}). \tag{2.20}$$

Similarly, for each unbound constituent α, a mass balance equation is written with inherent advection and a constitutive model F^α with similar dependencies as

$$\partial_t \rho^\alpha + \nabla \cdot (\mathbf{v}^\alpha \rho^\alpha) = F^\alpha(\rho^\omega, \{\rho^\beta\}, \{\rho^\alpha\}). \tag{2.21}$$

Momentum balance is written for the entire mixture in terms of pore pressure of the inter-

stitial fluid and the solid phase elastic stress as follows

$$-\nabla p + \nabla \cdot \sigma^E(\mathbf{u}^s) = \mathbf{0}, \tag{2.22}$$

where σ^E is the solid phase elastic stress. Momentum balance is also written for water and for each unbound phase in terms of the corresponding chemical potentials μ^ω, μ^α, and diffusive drag terms that account for energy dissipation due to relative motion between phases. In such statements of momentum balance, the gradients of the chemical potentials are the motive forces, balanced by the frictional forces occurring as one phase flows past another in the mixture. As in most cartilage models, inertial terms are neglected due to dominance of intrinsic and inter-phase energy dissipation mechanisms and the slow time scales for cartilage regeneration. Thus the momentum equations are

$$-\rho_T^\omega \phi^\omega \nabla \mu^\omega + f^{\omega s}(\dot{\mathbf{u}}^s - \mathbf{v}^\omega) + \sum_\alpha f^{\omega \alpha}(\mathbf{v}^\alpha - \mathbf{v}^\omega) = \mathbf{0}, \tag{2.23}$$

$$-M_\alpha \phi^\omega c^\alpha \nabla \mu^\alpha + f^{s\alpha}(\dot{\mathbf{u}}^s - \mathbf{v}^\alpha) + \sum_{\gamma \neq \alpha} f^{\gamma \alpha}(\mathbf{v}^\gamma - \mathbf{v}^\alpha) = \mathbf{0}, \tag{2.24}$$

where μ^ω and μ^α are the chemical potentials for water and for the unbound phases, respectively. Here, the $f^{\alpha \beta}$'s are frictional coefficients per unit tissue volume between the unbound phases α and bound phases β. As is the case in triphasic mixture theory for articular cartilage, the diffusive drag between phases α and β are assumed to be symmetric, i.e. $f^{\alpha \beta} = f^{\beta \alpha}$.

Lastly, the mixture is assumed to be saturated so that:

$$\phi^s + \phi^\omega = 1, \quad \text{where}: \ \phi^s = \sum_\beta \phi^\beta, \quad \phi^\alpha \approx 0, \tag{2.25}$$

with the porosity being $\phi^\omega = 1 - \phi^s$, where the solid phase volume fraction is the sum of all volume fractions for bound phases, based on the assumption that all unbound, dissolved phases occupy negligible volume.

2.3.4 Constitutive Equations

A key goal of the spatio-temporal PDE model extension considered in this thesis is to develop more realistic models for cartilage regeneration in cell-seeded scaffolds. Ideally, this should be done in coordination with experimental measurements of spatially and temporally evolving constituent volume fractions and mechanical properties at both microscopic and macroscopic levels. Unfortunately, to date, very limited data of this nature is available. Furthermore, the manner in which several key material properties of engineered cartilage (e.g. Young's modulus)

depend on the evolving solid phase variables in system is unknown. Of particular relevance is the analysis of the momentum balance equations (2.22)-(2.24) under quasi-static conditions, i.e. at a time snapshot of experimental testing. When the solid phase is assumed to be linear and isotropic, the fluid phase is considered inviscid, and the predominant energy dissipation mechanism is fluid-solid drag, the constitutive functions in (2.22), (2.23), and (2.24) have the assumed forms: [64]

$$\sigma^E = \lambda tr(\mathbf{e}^s)I + 2\mu\mathbf{e}^s, \tag{2.26}$$

$$\mu^\omega = \frac{p}{RT} - \phi \sum_\alpha c^\alpha, \qquad \alpha \neq f \tag{2.27}$$

$$\mu^\alpha = \gamma_\alpha c^\alpha, \qquad \alpha = f \tag{2.28}$$

In the equations above, $\mathbf{e}^s = 1/2[(\nabla\mathbf{u}^s) + (\nabla\mathbf{u}^s)^T]$ is the infinitesimal strain tensor, (λ, μ) are the elastic Lamé coefficients, R is the universal gas constant, T is the absolute ambient temperature, ϕ is the osmotic coefficient, and γ_α is the activity coefficient of the solute. Note that

$$\lambda = \frac{E\nu}{(1+\nu)(1-2\nu)} \quad \text{and} \quad \mu = \frac{E}{2(1+\nu)}, \tag{2.29}$$

where E is the Young's modulus and ν is the Poisson's ratio.

17

Chapter 3

Spherical Mixture Model in the Local Environment of a Single Cell

3.1 Introduction

The current chapter focuses on specializing the spatio-temporal PDE formulation described in Section 2.3 to model cartilage ECM regeneration in the local environment of a single cartilage cell (chondrocyte) seeded in a scaffold material. Both the cell and the surrounding scaffold are assumed to be spherically symmetric. The assumption of spherical symmetry for the cell and its surrounding environment is more natural for a scaffold, which has a high porosity as compared to mature articular cartilage.

Based on this assumption, all variables in the model depend on only one spatial coordinate (r) and time (t), similar to the study by Dimicco et al. [10]. The resulting one-dimensional spatio-temporal (PDE) model captures interactions among biomechanical mechanisms such as interstitial flow, ECM or cell deformation and fluid pressurization, biophysical phenomena like diffusive and convective transport, chemical degradation of the scaffold, and physiological phenomena such as cell-mediated regulation of ECM biosynthesis and cross-linking. The model assumes that unbound ECM constituents are synthesized inside the cell and transported within both the cellular and extracellular domains by diffusion or convection within the fluid phase, in a circumferentially uniform way. As unlinked ECM accumulates in the extracellular region, the presence of dissolved growth factors allows the ECM to cross-link and form bound and linked ECM while, simultaneously, the scaffold degrades. The interaction of these mechanisms within the framework of this one-dimensional model are illustrated in Figure 3.1.
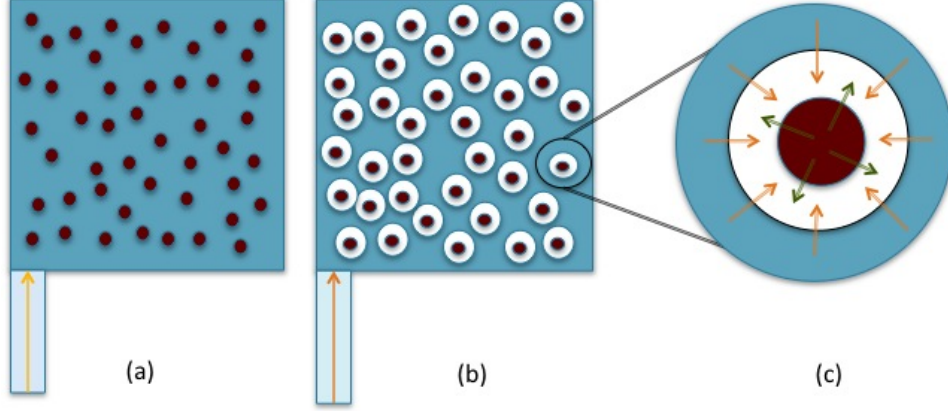
Figure 3.1: (a) A hydrogel scaffold (blue) containing dissolved growth factors (orange) is seeded with sparsely distributed chondrocytes (red). (b) Over time, the chondrocytes synthesize new ECM (white). (c) In this chapter, the model describes interactions in the local environment of a single chondrocyte where cell-synthesized unlinked ECM (green) is transformed into linked ECM (white) using growth factors (orange).

3.2 Primary Variables

The primary variables in this system are now summarized. Biomechanical variables, include the solid phase displacement ($\mathbf{u}^s$), fluid phase velocity ($\mathbf{v}^\omega$), pore pressure (p) of the interstitial fluid and the water volume fraction or porosity (ϕ^ω). The evolution of bound constituents is tracked by volume fractions ϕ^β where the constituents β are chosen to be linked ECM (LM) and scaffold (Sc). Similarly the unbound constituents can be represented by volume fractions ϕ^α where the constituents α are chosen to be unlinked ECM (UM) and growth-factor (G). However, the unbound constituents are dissolved in the interstitial fluid and assumed to occupy negligible mixture volume. Hence, in the model formulation, their evolution is tracked using both concentrations (c^{UM}) and (c^G) and velocities (v^{UM}) and (v^G). Based on the choice of these primary variables and the relations

$$\rho^\beta = \phi^\beta \rho_T^\beta, \ (\beta = \omega, LM, Sc), \text{ and } \rho^\alpha = \phi^\omega c^\alpha M_\alpha, \ (\alpha = UM, G), \tag{3.1}$$

the spatio-temporal PDE model that was presented in section 2.3 can be written as:

Mass Balance

$$\partial_t \phi^\omega + \nabla \cdot (\mathbf{v}^\omega \phi^\omega) = 0, \tag{3.2}$$

$$\partial_t \phi^{LM} + \nabla \cdot (\dot{\mathbf{u}}^s \phi^{LM}) = F^{LM}(\phi^\omega, \phi^{LM}, \phi^{Sc}, c^{UM}, c^G), \tag{3.3}$$

$$\partial_t \phi^{Sc} + \nabla \cdot (\dot{\mathbf{u}}^s \phi^{Sc}) = F^{Sc}(\phi^\omega, \phi^{LM}, \phi^{Sc}, c^{UM}, c^G), \tag{3.4}$$

$$\partial_t \left(\phi^\omega c^{UM} \right) + \nabla \cdot (\mathbf{v}^{UM} \phi^\omega c^{UM}) = F^{UM}(\phi^\omega, \phi^{LM}, \phi^{Sc}, c^{UM}, c^G), \tag{3.5}$$

$$\partial_t \left(\phi^\omega c^G \right) + \nabla \cdot (\mathbf{v}^G \phi^\omega c^G) = F^G(\phi^\omega, \phi^{LM}, \phi^{Sc}, c^{UM}, c^G). \tag{3.6}$$

Saturated Mixture

$$\phi^s + \phi^\omega = 1, \quad \text{where}: \ \phi^s = \phi^{LM} + \phi^{Sc}, \quad \phi^{UM} \approx 0 \ \phi^G \approx 0, \tag{3.7}$$

Momentum Balance

$$-\nabla p + \nabla \cdot \sigma^E(\mathbf{u}^s) = \mathbf{0}, \tag{3.8}$$

$$-\rho_T^\omega \phi^\omega \nabla \mu^\omega(p, c^{UM}, c^G) + f^{\omega s}(\dot{\mathbf{u}}^s - \mathbf{v}^\omega) + f^{\omega(UM)}(\mathbf{v}^{UM} - \mathbf{v}^\omega) + f^{\omega G}(\mathbf{v}^G - \mathbf{v}^\omega) = \mathbf{0}, \tag{3.9}$$

$$-M_{UM} \phi^\omega c^{UM} \nabla \mu^{UM}(c^{UM}) + f^{s(UM)}(\dot{\mathbf{u}}^s - \mathbf{v}^{UM}) + f^{\omega(UM)}(\mathbf{v}^\omega - \mathbf{v}^{UM}) = \mathbf{0}, \tag{3.10}$$

$$-M_G \phi^\omega c^G \nabla \mu^G(c^G) + f^{sG}(\dot{\mathbf{u}}^s - \mathbf{v}^G) + f^{\omega G}(\mathbf{v}^\omega - \mathbf{v}^G) = \mathbf{0}, \tag{3.11}$$

Constitutive Equations

$$\sigma^E(\mathbf{u}^s) = \lambda tr(\mathbf{e}^s)I + 2\mu \mathbf{e}^s, \text{where}: \ \mathbf{e}^s = 1/2\left((\nabla \mathbf{u}^s) + (\nabla \mathbf{u}^s)^t\right) \tag{3.12}$$

$$\mu^\omega(p, c^{UM}, c^G) = \frac{p}{RT} - \phi(c^{UM} + c^G), \tag{3.13}$$

$$\mu^{UM}(c^{UM}) = \gamma_{UM} c^{UM}, \tag{3.14}$$

$$\mu^G(c^G) = \gamma_G c^G. \tag{3.15}$$

The equations as formulated above are now specialized to the case of a one-dimensional spherical model.

3.3 One Dimensional Spherical Model of a Cell Seeded in a Porous Scaffold

In this model two regions are considered (Figure 3.2), an inner spherical region (Region 1) that represents a cell with radius a and an outer spherical ring (Region 2) of dimension b that represents the evolving extracellular region. The extracellular region is initially assumed to contain only scaffold with interstitial fluid and dissolved growth factors while the cell is assumed to contain a solid phase, interstitial fluid and dissolved solutes. Both regions are modeled as saturated continuum mixtures.

A spherically symmetric model is developed by assuming that the kinematic variables. i.e.
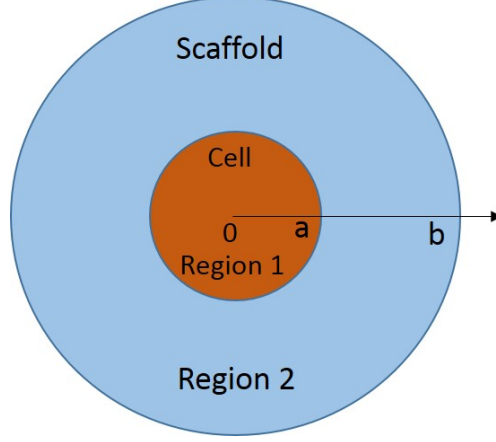
Figure 3.2: Illustration of the initial configuration for one dimensional spherical model of a single cell seeded in a scaffold.

solid displacements and fluid and solute velocities, are exclusively radial and depend on only the radial coordinate (r) and time (t). Hence, in a spherical coordinate system

$$\mathbf{u}^s = (u^s(t,r),0,0), \ \ \mathbf{v}^\alpha = (v^\alpha(t,r),0,0), \ \ (\alpha = w, UM, G), \tag{3.16}$$

3.3.1 Cell Region

The interaction function F^α in section 2.3, equation (2.21), where $\alpha = UM$ is chosen to be

$$F^{UM}(\rho^\omega, \rho^s, \rho^{UM}) = k_{UM} N^* \left(\rho_*^{UM} - \frac{\rho^{UM}}{\phi^\omega} \right) \phi^\omega. \tag{3.17}$$

By using (3.1) and the following relation involving the critical unlinked ECM density within the surrounding interstitial fluid

$$\rho_*^{UM} = c_*^{UM} M_{UM}, \tag{3.18}$$

we obtain

$$F^{UM}(\phi^\omega, \phi^s, c^{UM}) = k_{UM} N^* \left(c_*^{UM} - c^{UM} \right) \phi^\omega. \tag{3.19}$$

Also, the constitutive law for the solid phase elastic stress σ^E in (3.8) is written as:

$$\sigma^E(u^s) = \lambda_c tr(\mathbf{e}^s)I + 2\mu_c \mathbf{e}^s \tag{3.20}$$

where (λ_c, μ_c) are the elastic Lamé coefficients for the cell. Governing equations for the cell region are formulated for $0 < r < a$ and $t > 0$ as follows:

Mass Balance:

$$\partial_t \phi^\omega + \left(\frac{\partial}{\partial r} + \frac{2}{r} \right) (v^\omega \phi^\omega) = 0, \tag{3.21}$$

$$\partial_t \phi^s + \left(\frac{\partial}{\partial r} + \frac{2}{r} \right) (\dot{u}^s \phi^s) = 0, \tag{3.22}$$

$$\partial_t (\phi^\omega c^{UM}) + \left(\frac{\partial}{\partial r} + \frac{2}{r} \right) (v^{UM} \phi^\omega c^{UM}) = k_{UM} N^* (c_*^{UM} - c^{UM}) \phi^\omega. \tag{3.23}$$

Saturated Mixture:

$$\phi^s + \phi^\omega = 1, \quad \phi^{UM} \approx 0, \tag{3.24}$$

Momentum Balance:

$$-\frac{\partial p}{\partial r} + (\lambda_c + 2\mu_c) \frac{\partial}{\partial r} \left(\frac{\partial u^s}{\partial r} + \frac{2}{r} u^s \right) = 0, \tag{3.25}$$

$$-\rho_T^\omega \phi^\omega \frac{\partial}{\partial r} \mu^\omega + f^{\omega s} (\dot{u}^s - v^\omega) + f^{\omega(UM)} (v^{UM} - v^\omega) = 0, \tag{3.26}$$

$$-M_{UM} \phi^\omega c^{UM} \frac{\partial}{\partial r} \mu^{UM} + f^{s(UM)} (\dot{u}^s - v^{UM}) + f^{\omega(UM)} (v^\omega - v^{UM}) = 0. \tag{3.27}$$

In (3.23), $k_{UM}[(\text{s} \cdot \text{mol/L})^{-1}]$ is the unlinked ECM synthesis rate and $N^*[(\text{mol/L})]$ is a saturated nutrient concentration, based on the assumption that diffusive transport of small solutes is fast relative to transport mechanisms of synthesized ECM constituents. Production of unlinked ECM is assumed to proceed until the critical unlinked ECM concentration within the surrounding interstitial fluid c_*^{UM} is reached within the surrounding interstitial fluid.

3.3.2 Extracellular Region

The interaction functions F^β and F^α in section 2.3 where $\beta = LM, Sc$ and $\alpha = UM, G$ are chosen to be

$$F^{LM}(\rho^\omega, \rho^{LM}, \rho^{Sc}, \rho^{UM}, \rho^G) = f(\phi^s) \rho^{UM} \rho^G, \tag{3.28}$$

$$F^{Sc}(\rho^\omega, \rho^{LM}, \rho^{Sc}, \rho^{UM}, \rho^G) = -k_{Sc} \rho^{Sc}, \tag{3.29}$$

$$F^{UM}(\rho^\omega, \rho^{LM}, \rho^{Sc}, \rho^{UM}, \rho^G) = -f(\phi^s) \rho^{UM} \rho^G, \tag{3.30}$$

$$F^G(\rho^\omega, \rho^{LM}, \rho^{Sc}, \rho^{UM}, \rho^G) = -f(\phi^s) \rho^{UM} \rho^G, \tag{3.31}$$

Using the relations in (3.1), these functions can be represented in terms of our primary variables as:

$$F^{LM}(\phi^\omega, \phi^{LM}, \phi^{Sc}, c^{UM}, c^G) = \frac{f(\phi^s) M_{UM} M_G}{\rho_T^{LM}} (\phi^\omega)^2 c^{UM} c^G, \tag{3.32}$$

$$F^{Sc}(\phi^\omega, \phi^{LM}, \phi^{Sc}, c^{UM}, c^G) = -k_{Sc} \phi^{Sc}, \tag{3.33}$$

22

$$F^{UM}(\phi^\omega, \phi^{LM}, \phi^{Sc}, c^{UM}, c^G) = -f(\phi^s)M_G(\phi^\omega)^2 c^{UM} c^G, \tag{3.34}$$

$$F^G(\phi^\omega, \phi^{LM}, \phi^{Sc}, c^{UM}, c^G) = -f(\phi^s)M_{UM}(\phi^\omega)^2 c^{UM} c^G. \tag{3.35}$$

Also, the solid phase elastic stress in the extracellular region (scaffold region) is defined by

$$\sigma^E(u^s) = \lambda_{Sc} tr(\mathbf{e}^s)I + 2\mu_{Sc}\mathbf{e}^s, \tag{3.36}$$

where (λ_{Sc}, μ_{Sc}) are the elastic Lamé coefficients in the scaffold region and this relation for σ^E is used in (3.8). Governing equations for the extracellular region are formulated for $a < r < b$ and $t > 0$ as follows:

Mass Balance:
$$\partial_t \phi^\omega + \left(\frac{\partial}{\partial r} + \frac{2}{r}\right)(v^\omega \phi^\omega) = 0, \tag{3.37}$$

$$\partial_t \phi^{LM} + \left(\frac{\partial}{\partial r} + \frac{2}{r}\right)(\dot{u}^s \phi^{LM}) = \frac{f(\phi^s)M_{UM}M_G}{\rho_T^{LM}}(\phi^\omega)^2 c^{UM} c^G, \tag{3.38}$$

$$\partial_t \phi^{Sc} + \left(\frac{\partial}{\partial r} + \frac{2}{r}\right)(\dot{u}^s \phi^{Sc}) = -k_{Sc}\phi^{Sc}, \tag{3.39}$$

$$\partial_t(\phi^\omega c^{UM}) + \left(\frac{\partial}{\partial r} + \frac{2}{r}\right)(v^{UM}\phi^\omega c^{UM}) = -f(\phi^s)M_G(\phi^\omega)^2 c^{UM} c^G, \tag{3.40}$$

$$\partial_t(\phi^\omega c^G) + \nabla \cdot (\mathbf{v}^G \phi^\omega c^G) = -f(\phi^s)M_{UM}(\phi^\omega)^2 c^{UM} c^G, \tag{3.41}$$

Saturated Mixture:

$$\phi^s + \phi^\omega = 1, \quad \text{where}: \quad \phi^s = \phi^{LM} + \phi^{Sc}, \quad \phi^{UM} \approx 0, \;, \;\phi^G \approx 0, \tag{3.42}$$

Momentum Balance:
$$-\frac{\partial p}{\partial r} + (\lambda_{Sc} + 2\mu_{Sc})\frac{\partial}{\partial r}\left(\frac{\partial u^s}{\partial r} + \frac{2}{r}u^s\right) = 0, \tag{3.43}$$

$$-\rho_T^\omega \phi^\omega \frac{\partial}{\partial r}\mu^\omega + f^{\omega s}(\dot{u}^s - v^\omega) + f^{\omega(UM)}(v^{UM} - v^\omega) + f^{\omega G}(v^G - v^\omega) = 0, \tag{3.44}$$

$$-M_{UM}\phi^\omega c^{UM}\frac{\partial}{\partial r}\mu^{UM} + f^{s(UM)}(\dot{u}^s - v^{UM}) + f^{\omega(UM)}(v^\omega - v^{UM}) = 0, \tag{3.45}$$

$$-M_G\phi^\omega c^G\frac{\partial}{\partial r}\mu^G + f^{sG}(\dot{u}^s - v^G) + f^{\omega G}(v^\omega - v^G) = 0. \tag{3.46}$$

The linking rate $f(\phi^s)$ that appears in (3.38), (3.40), and (3.41) is modeled using as a Gaussian distribution with respect to the solid phase volume fraction ϕ^s, similar to the ODE

model in Section 2.2 as:

$$f(\phi^s) = k_{UL}\exp\left(-\frac{(\phi^s - \phi_*^s)^2}{2\sigma^2}\right), \tag{3.47}$$

where $k_{UL}[(\text{s} \cdot \text{kg/L})^{-1}]$ is the maximum linking rate, occurring when $\phi^s = \phi_*^s$. In (3.47), the parameters ϕ_*^s and σ define regimes in which rates for formation of linked ECM are enhanced or inhibited. At low solid volume fraction ϕ^s, linking is assumed to increase with increasing ϕ^s due to cell-scaffold biocompatibility. However, as ϕ^s increases past ϕ_*^s, the linking rate begins to slow down with decreasing average porosity $\phi^\omega = 1 - \phi^s$, to capture adverse effects on the ability of unlinked ECM to form linked ECM as the pore size in the evolving tissue construct reduces.

The term on the right hand side of (3.38) represents the interaction between the synthesized unlinked ECM and the growth factor that facilitates assembly of the unlinked ECM into linked ECM. Specifically, ECM linking is assumed to be regulated by both product inhibition and a continuous set of linking rates $f[(\text{s} \cdot \text{kg/L})^{-1}]$ that depend on the time-varying average solid volume fraction ϕ^s in the construct, as modeled in (3.47).

In (3.39), $k_{Sc}[\text{s}^{-1}]$ is the scaffold degradation rate. Terms on the right hand side of (3.40) and (3.41) describe how unlinked ECM and growth factors are utilized in the system to produce linked ECM.

3.3.3   Initial, Boundary and Interface Conditions

To complete the model formulation we must specify initial conditions on the two-zone spherical domain $(0 < r < b)$, boundary conditions at $r = 0, b$, and interface conditions along the fixed interface, which corresponds to the cell membrane, at $r = a$. Initially, in a cartilage cell-scaffold system, the cell is seeded within a scaffold of known initial porosity that is assumed to have a uniform concentration of growth factor. Initially, it is also assumed that the system is at rest and free of any unlinked or linked ECM. The resulting initial conditions for $0 < r < b$ are:

$$c^G(0, r) = c_0^G, \quad \phi^{Sc}(0, r) = \phi_0^{Sc}, \tag{3.48}$$

$$p(0, r) = 0, \quad \phi^{LM}(0, r) = 0, \quad c^{UM}(0, r) = 0, \quad u^s(0, r) = 0. \tag{3.49}$$

On the cell boundary $r = a$, interface conditions consist of continuity relations for the solid phase normal stress and the water and unlinked ECM fluxes relative to the solid phase:

$$\sigma_{rr}^E\big|_{r=a^-} = \sigma_{rr}^E\big|_{r=a^+}, \tag{3.50}$$

$$\phi^\omega(v^\omega - \dot{u}^s)\big|_{r=a^-} = \phi^\omega(v^\omega - \dot{u}^s)\big|_{r=a^+}, \tag{3.51}$$

$$\phi^\omega c^{UM}(v^{UM} - \dot{u}^s)\big|_{r=a^-} = \phi^\omega c^{UM}(v^{UM} - \dot{u}^s)\big|_{r=a^+}, \tag{3.52}$$

The cell membrane is assumed to be impermeable to scaffold (Sc), linked ECM (LM), and growth factor (G) present in the extracellular region, leading to the no-flux conditions

$$\frac{\partial \phi^{Sc}}{\partial r}(t, a^+) = 0, \quad \frac{\partial \phi^{LM}}{\partial r}(t, a^+) = 0, \quad \frac{\partial c^G}{\partial r}(t, a^+) = 0. \tag{3.53}$$

Based on symmetry and physical constraints, boundary conditions at the center of the cell are

$$\frac{\partial c^{UM}}{\partial r}(t, 0) = 0, \quad \frac{\partial \phi^\omega}{\partial r}(t, 0) = 0, \quad u^s(t, 0) = 0, \quad \frac{\partial p}{\partial r}(t, 0) = 0. \tag{3.54}$$

The outer boundary of the extracellular region ($r = b$) is assumed to lie in the far-field region of the system. This boundary is assumed to be stress-free and no-flux conditions are prescribed for the scaffold, linked matrix, unlinked matrix, and growth factor leading to the boundary conditions

$$p(t, b) = 0, \quad \sigma_{rr}^E(t, b) = 0, \tag{3.55}$$

$$\frac{\partial \phi^{Sc}}{\partial r}(t, b) = 0, \quad \frac{\partial \phi^{LM}}{\partial r}(t, b) = 0, \quad \frac{\partial c^{UM}}{\partial r}(t, b) = 0, \quad \frac{\partial c^G}{\partial r}(t, b) = 0, \tag{3.56}$$

The resulting one-dimensional spatio-temporal cartilage regeneration model then consists of the equations (3.21)-(3.27) and equations (3.37)-(3.46) subject to the conditions (3.48)-(3.56).

3.4 Model Reduction

The model developed in the previous section can be further reduced. Adding together (3.21) and (3.22) and using the fact the mixture is saturated (3.42), we obtain the reduced equation

$$\frac{\partial}{\partial r}(r^2(\phi^\omega v^\omega + (1 - \phi^\omega)\dot{u}^s)) = 0. \tag{3.57}$$

Integrating with respect to r gives

$$(\phi^\omega v^\omega + (1 - \phi^\omega)\dot{u}^s) = f(t)/r^2, \tag{3.58}$$

where $f(t)$ is an arbitrary function. Since our solutions must be bounded for all time at $r = 0$, we take $f(t) = 0$, giving the relation

$$\phi^\omega v^\omega + (1 - \phi^\omega)\dot{u}^s = 0 \tag{3.59}$$

which will be used in the place of (3.22). Again, using the fact that the mixture is saturated (3.42) and the approximations $\phi^{UM} \approx 0$ and $\phi^G \approx 0$, (3.37) is replaced by the summation of (3.37)-(3.39), leading to the reduced equation:

$$\left(\frac{\partial}{\partial r} + \frac{2}{r}\right)(v^\omega \phi^\omega + \dot{u}^s(1 - \phi^\omega)) = -k_{Sc}\phi^{Sc} + \frac{f(\phi^s)M_{UM}M_G}{\rho_T^{LM}}(\phi^\omega)^2 c^{UM} c^G \tag{3.60}$$

The diffusive drag coefficients between phases in our mixture can be related to solute diffusivities using the relations [64]

$$f^{\omega s} = \frac{\phi^\omega}{k}, \quad f^{\omega(UM)} = \frac{RT\phi^\omega c^{UM}}{D^{\omega(UM)}}, \quad f^{\omega G} = \frac{RT\phi^\omega c^G}{D^{\omega G}}. \tag{3.61}$$

In (3.61), k is the hydraulic permeability constant, $D^{\omega(UM)}$, and $D^{\omega G}$ are the diffusivities of unlinked ECM and growth factor, respectively, in water. $D^{\omega(UM)}$, and $D^{\omega G}$ are assumed to be functions of ϕ^ω as defined in [17] by

$$D^{\omega(UM)} = \frac{D^{UM}(\phi^\omega)^2}{(2 - \phi^\omega)^2}, \quad D^{\omega G} = \frac{D^G(\phi^\omega)^2}{(2 - \phi^\omega)^2}, \tag{3.62}$$

where D^{UM} and D^G are the diffusivity of unlinked matrix ECM and the growth factor, respectively, in free solution. Similar to the approach used in [64], we assume that $f^{s(UM)} \approx 0$ and $f^{sG} \approx 0$.

Based on the transformed relations above, the full 1D model is now re-written in a simpler form. In doing so, we substitute μ^ω from (3.13) in (3.26) and (3.44), μ^{UM} from (3.14) in (3.27) and (3.45), and μ^G from (3.15) in (3.46). Also, substituting the diffusive drag coefficients (3.61) in (3.26), (3.27), (3.44), (3.45), and (3.46), the equations (3.26), (3.27), (3.44), (3.45), and (3.46) become linear equations in v^ω, v^{UM}, and v^G. We solve the linear system (3.26) and (3.27) for v^ω, v^{UM} and the linear system (3.44), (3.45), and (3.46) for v^ω, v^{UM}, and v^G. Lastly, we substitute the relations obtained for v^ω, v^{UM}, and v^G into all relevant equations to eliminate these variables. The reduced model is now summarized for each region in the following two subsections.

3.4.1 Cell Region

In the cell region, the reduced model contains four dependent variables that are the pore pressure (p), solid phase displacement (u^s), water volume fraction (ϕ^ω), and unlinked ECM concentration (c^{UM}). For $0 < r < a$ and $t > 0$, the reduced governing equations are:

$$-\frac{\partial p}{\partial r} + (\lambda_c + 2\mu_c)\frac{\partial}{\partial r}\left(\frac{\partial u^s}{\partial r} + \frac{2}{r}u^s\right) = 0, \tag{3.63}$$

$$\partial_t \phi^\omega + \left(\frac{\partial}{\partial r} + \frac{2}{r}\right)\left[(\phi^\omega - 1)\dot{u}^s\right] = 0, \tag{3.64}$$

$$\dot{u}^s = k\frac{\partial p}{\partial r} - RTk(\phi - 1)\frac{\partial c^{UM}}{\partial r}, \tag{3.65}$$

$$\partial_t(\phi^\omega c^{UM}) + \left(\frac{\partial}{\partial r} + \frac{2}{r}\right)\left[(\phi^\omega - 1)c^{UM}\dot{u}^s - D^{\omega(UM)}\phi^\omega\frac{\partial c^{UM}}{\partial r}\right] =$$
$$k_{UM}N^*(c_*^{UM} - c^{UM})\phi^\omega. \tag{3.66}$$

3.4.2 Extracellular Region

In the extracellular region, the reduced model contains six dependent variables that are the pore pressure (p), solid phase displacement (u^s), linked ECM, and scaffold volume fractions (ϕ^{LM} and ϕ^{Sc}), and unlinked ECM and growth factor concentrations (c^{UM} and c^G). We note that the porosity ϕ^ω can be determined from ϕ^{LM} and ϕ^{Sc} since the mixture is saturated. For $a < r < b$ and $t > 0$, the reduced governing equations are:

$$-\frac{\partial p}{\partial r} + (\lambda_{Sc} + 2\mu_{Sc})\frac{\partial}{\partial r}\left(\frac{\partial u^s}{\partial r} + \frac{2}{r}u^s\right) = 0, \tag{3.67}$$

$$\left(\frac{\partial}{\partial r} + \frac{2}{r}\right)\left[-k\frac{\partial p}{\partial r} + RTk(\phi - 1)\left(\frac{\partial c^{UM}}{\partial r} + \frac{\partial c^G}{\partial r}\right) + \dot{u}^s\right] =$$
$$- k_{Sc}\phi^{Sc} + \frac{f(\phi^s)M_{UM}M_G}{\rho_T^{LM}}(\phi^\omega)^2 c^G c^{UM}, \tag{3.68}$$

$$\partial_t\phi^{LM} + \left(\frac{\partial}{\partial r} + \frac{2}{r}\right)(\dot{u}^s\phi^{LM}) = \frac{f(\phi^s)M_{UM}M_G}{\rho_T^{LM}}(\phi^\omega)^2 c^G c^{UM}, \tag{3.69}$$

$$\partial_t\phi^{Sc} + \left(\frac{\partial}{\partial r} + \frac{2}{r}\right)(\dot{u}^s\phi^{Sc}) = -k_{Sc}\phi^{Sc}, \tag{3.70}$$

$$\partial_t(\phi^\omega c^{UM}) + \left(\frac{\partial}{\partial r} + \frac{2}{r}\right)\left[-kc^{UM}\frac{\partial p}{\partial r} + \left(RTk(\phi - 1)c^{UM} - D^{\omega(UM)}\phi^\omega\right)\frac{\partial c^{UM}}{\partial r} + \phi^\omega c^{UM}\dot{u}^s\right]$$
$$+ \left(\frac{\partial}{\partial r} + \frac{2}{r}\right)\left[RTk(\phi - 1)c^{UM}\frac{\partial c^G}{\partial r}\right] = -f(\phi^s)M_G(\phi^\omega)^2 c^G c^{UM}, \tag{3.71}$$

$$\partial_t(\phi^\omega c^G) + \left(\frac{\partial}{\partial r} + \frac{2}{r}\right)\left[-kc^G\frac{\partial p}{\partial r} + \left(RTk(\phi-1)c^G - D^{\omega G}\phi^\omega\right)\frac{\partial c^G}{\partial r} + \phi^\omega c^G \dot{u}^s\right]$$
$$+ \left(\frac{\partial}{\partial r} + \frac{2}{r}\right)\left[RTk(\phi-1)c^G\frac{\partial c^{UM}}{\partial r}\right] = -f(\phi^s)M_G(\phi^\omega)^2 c^G c^{UM}. \quad (3.72)$$

3.4.3   Initial, Boundary, and Interface Conditions

For the four variables that are present in both the cell and extracellular regions, we have the initial conditions for $0 < r < b$:

$$p(0,r) = 0, \qquad c^{UM}(0,r) = 0, \quad u^s(0,r) = 0, \quad \phi^\omega(0,r) = \begin{cases} (\phi_0^\omega)_c & 0 < r < a \\ (\phi_0^\omega)_{Sc} & a < r < b \end{cases}. \quad (3.73)$$

In the extracellular region $(a < r < b)$, initial conditions for the additional variables are:

$$c^G(0,r) = c_0^G, \qquad \phi^{LM}(0,r) = 0, \quad (3.74)$$

where we note that the initial solid phase volume fraction in the extracellular region is $\phi_0^s = 1 - (\phi_0^\omega)_{Sc}$.

At the cell center $(r = 0)$, the boundary conditions are

$$\frac{\partial c^{UM}}{\partial r}(t,0) = 0, \quad \frac{\partial \phi^\omega}{\partial r}(t,0) = 0, \quad u^s(t,0) = 0, \quad \frac{\partial p}{\partial r}(t,0) = 0, \quad (3.75)$$

and at the interface $(r = a)$ between the cell and the extracellular region, the interface conditions become:

$$(\lambda_c + 2\mu_c)\left(\frac{\partial u^s}{\partial r}\right) + \frac{2\lambda_c}{r}u^s\bigg|_{r=a^-} = (\lambda_{Sc} + 2\mu_{Sc})\left(\frac{\partial u^s}{\partial r}\right) + \frac{2\lambda_{Sc}}{r}u^s\bigg|_{r=a^+}, \quad (3.76)$$

$$-k\frac{\partial p}{\partial r} + RTk(\phi-1)\frac{\partial c^{UM}}{\partial r}\bigg|_{r=a^-} = -k\frac{\partial p}{\partial r} + RTk(\phi-1)\frac{\partial c^{UM}}{\partial r}\bigg|_{r=a^+}, \quad (3.77)$$

$$-kc^{UM}\frac{\partial p}{\partial r} + \left(RTk(\phi-1)c^{UM} - D^{UM}\phi^\omega\right)\frac{\partial c^{UM}}{\partial r}\bigg|_{r=a^-} =$$
$$-kc^{UM}\frac{\partial p}{\partial r} + \left(RTk(\phi-1)c^{UM} - D^{UM}\phi^\omega\right)\frac{\partial c^{UM}}{\partial r}\bigg|_{r=a^+}, \quad (3.78)$$

$$\frac{\partial \phi^{Sc}}{\partial r}(t,a) = 0, \quad \frac{\partial \phi^{LM}}{\partial r}(t,a) = 0 \quad , \frac{\partial c^G}{\partial r}(t,a) = 0. \quad (3.79)$$

Finally, at the outer boundary of the extracellular region $(r = b)$, the boundary conditions

become:

$$\left.(\lambda_{Sc} + 2\mu_{Sc})\left(\frac{\partial u^s}{\partial r}\right) + \frac{2\lambda_{Sc}}{r}u^s\right|_{r=b} = 0, \tag{3.80}$$

$$p(t,b) = 0, \quad \frac{\partial \phi^{Sc}}{\partial r}(t,b) = 0, \quad \frac{\partial \phi^{LM}}{\partial r}(t,b) = 0, \quad \frac{\partial c^{UM}}{\partial r}(t,b) = 0, \quad \frac{\partial c^{G}}{\partial r}(t,b) = 0. \tag{3.81}$$

The system of equations above consists of the simplified equations (3.63)-(3.66) and (3.67)-(3.72) subject to the conditions (3.74)-(3.81). Prior to considering finite difference schemes for the numerical solution of this system, the system of equations is nondimensionalized, as outlined in the next section.

3.5   Nondimensionalization

The system is nondimensionalized to facilitate a parametric analysis of interactions among mechanisms captured in the model and to prevent ill conditioning of the linear algebraic system associated with the discretized governing equations. The following transformations are introduced and all nondimensional variables are indicated using the hat notation $\hat{}$

$$\hat{r} = \frac{r}{a}, \quad \hat{t} = \frac{D_0}{a^2}t, \quad \hat{c}^{UM} = \frac{c^{UM}}{c_0}, \quad \hat{c}^{G} = \frac{c^{G}}{c_0}, \quad \hat{u}^s = \frac{u^s}{a}, \hat{\dot{u}}^s = \frac{a}{D_0}\dot{u}^s, \quad \hat{p} = \frac{p}{H_A^{\alpha}}. \tag{3.82}$$

In the equations above, a, c_0, and D_0 are characteristic scales for the cell radius, concentration, and diffusivity, respectively and

$$H_A^{\alpha} = \lambda_\alpha + 2\mu_\alpha, \tag{3.83}$$

where α represent the cell (c) and the scaffold (Sc). Substituting (3.82) into (3.63)-(3.81) yields the following nondimensionalized model

3.5.1   Cell Region

For $0 < \hat{r} < 1$ and $\hat{t} > 0$, the nondimensionalized governing equations are:

$$-\frac{\partial \hat{p}}{\partial \hat{r}} + \frac{\partial^2 \hat{u}^s}{\partial \hat{r}^2} + \frac{2}{\hat{r}}\frac{\partial \hat{u}^s}{\partial \hat{r}} - \frac{2}{\hat{r}^2}\hat{u}^s = 0, \tag{3.84}$$

$$\partial_{\hat{t}}\phi^{\omega} + \left(\frac{\partial}{\partial \hat{r}} + \frac{2}{\hat{r}}\right)\left[(\phi^{\omega} - 1)\hat{\dot{u}}^s\right] = 0, \tag{3.85}$$

$$\hat{\dot{u}}^s = R_g^c\frac{\partial \hat{p}}{\partial \hat{r}} - K_g(\phi - 1)\frac{\partial \hat{c}^{UM}}{\partial \hat{r}}, \tag{3.86}$$

$$\partial_{\hat{t}}(\phi^\omega \hat{c}^{UM}) + \left(\frac{\partial}{\partial \hat{r}} + \frac{2}{\hat{r}}\right) \left[(\phi^\omega - 1)\hat{c}^{UM}\hat{u}^s - D_r^{UM}\phi^\omega \frac{\partial \hat{c}^{UM}}{\partial \hat{r}}\right] =$$
$$\hat{k}_{UM}N^*(\hat{c}_*^{UM} - \hat{c}^{UM})\phi^\omega. \quad (3.87)$$

3.5.2 Extracellular Region

For $1 < \hat{r} < \hat{b}$ and $\hat{t} > 0$, the nondimensionalized governing equations are:

$$-\frac{\partial \hat{p}}{\partial \hat{r}} + \frac{\partial^2 \hat{u}^s}{\partial \hat{r}^2} + \frac{2}{\hat{r}}\frac{\partial \hat{u}^s}{\partial \hat{r}} - \frac{2}{\hat{r}^2}\hat{u}^s = 0, \quad (3.88)$$

$$\left(\frac{\partial}{\partial \hat{r}} + \frac{2}{\hat{r}}\right)\left[-R_g^{Sc}\frac{\partial \hat{p}}{\partial \hat{r}} + K_g(\phi - 1)\left(\frac{\partial \hat{c}^{UM}}{\partial \hat{r}} + \frac{\partial \hat{c}^G}{\partial \hat{r}}\right) + \hat{u}^s\right] = -\hat{k}_{Sc}\phi^{Sc} + \hat{k}_1(\phi^\omega)^2 \hat{c}^G \hat{c}^{UM},$$
$$(3.89)$$

$$\partial_{\hat{t}}\phi^{LM} + \left(\frac{\partial}{\partial \hat{r}} + \frac{2}{\hat{r}}\right)(\hat{u}^s \phi^{LM}) = \hat{k}_1(\phi^\omega)^2 \hat{c}^G \hat{c}^{UM}, \quad (3.90)$$

$$\partial_{\hat{t}}\phi^{Sc} + \left(\frac{\partial}{\partial \hat{r}} + \frac{2}{\hat{r}}\right)(\hat{u}^s \phi^{Sc}) = -\hat{k}_{Sc}\phi^{Sc}, \quad (3.91)$$

$$\partial_{\hat{t}}(\phi^\omega \hat{c}^{UM}) + \left(\frac{\partial}{\partial \hat{r}} + \frac{2}{\hat{r}}\right)\left[-R_g^{Sc}\hat{c}^{UM}\frac{\partial \hat{p}}{\partial \hat{r}} + \left(K_g(\phi - 1)\hat{c}^{UM} - D_r^{UM}\phi^\omega\right)\frac{\partial \hat{c}^{UM}}{\partial \hat{r}} + \phi^\omega \hat{c}^{UM}\hat{u}^s\right]$$
$$+ \left(\frac{\partial}{\partial \hat{r}} + \frac{2}{\hat{r}}\right)\left[K_g(\phi - 1)\hat{c}^{UM}\frac{\partial \hat{c}^G}{\partial \hat{r}}\right] = -\hat{k}_2(\phi^\omega)^2 \hat{c}^G \hat{c}^{UM}, \quad (3.92)$$

$$\partial_{\hat{t}}(\phi^\omega \hat{c}^G) + \left(\frac{\partial}{\partial \hat{r}} + \frac{2}{\hat{r}}\right)\left[-R_g^{Sc}\hat{c}^G\frac{\partial \hat{p}}{\partial \hat{r}} + \left(K_g(\phi - 1)\hat{c}^G - D_r^G\phi^\omega\right)\frac{\partial \hat{c}^G}{\partial \hat{r}} + \phi^\omega \hat{c}^G \hat{u}^s\right]$$
$$+ \left(\frac{\partial}{\partial \hat{r}} + \frac{2}{\hat{r}}\right)\left[K_g(\phi - 1)\hat{c}^G\frac{\partial \hat{c}^{UM}}{\partial \hat{r}}\right] = -\hat{k}_3(\phi^\omega)^2 \hat{c}^G \hat{c}^{UM}, \quad (3.93)$$

where

$$R_g^c = \frac{kH_A^c}{D_0}, \quad R_g^{Sc} = \frac{kH_A^{Sc}}{D_0}, \quad K_g = \frac{RTkc_0}{D_0}, \quad (3.94)$$

$$D_r^G = \frac{D^{\omega G}}{D_0}, \quad D_r^{UM} = \frac{D^{\omega(UM)}}{D_0}, \quad \hat{k}_{UM} = \frac{a^2}{D_0}k_{UM}, \quad \hat{k}_{Sc} = \frac{a^2}{D_0}k_{Sc}, \quad (3.95)$$

$$\hat{k}_1 = \frac{f(\phi^s)(M_{UM})^2}{\rho_T^{LM}}\frac{c_0^2 a^2}{D_0}, \quad \hat{k}_2 = f(\phi^s)M_G\frac{c_0 a^2}{D_0}, \quad \hat{k}_3 = f(\phi^s)M_{UM}\frac{c_0 a^2}{D_0}. \quad (3.96)$$

3.5.3 Initial, Boundary, and Interface Conditions

For both the cell and extracellular regions, we have the nondimensionalized initial conditions for $0 < \hat{r} < \hat{b}$:

$$\hat{p}(0, \hat{r}) = 0, \quad \hat{c}^{UM}(0, \hat{r}) = 0, \quad \hat{u}^s(0, \hat{r}) = 0, \quad \phi^\omega(0, \hat{r}) = \begin{cases} (\phi_0^\omega)_c & 0 < \hat{r} < 1 \\ (\phi_0^\omega)_{Sc} & 1 < \hat{r} < \hat{b}. \end{cases} \tag{3.97}$$

In the extracellular region ($1 < \hat{r} < \hat{b}$), initial conditions for the additional variables are:

$$\hat{c}^G(0, \hat{r}) = \frac{c_0^G}{c_0}, \quad \phi^{LM}(0, \hat{r}) = 0, \tag{3.98}$$

where $\phi_0^s = 1 - (\phi_0^\omega)_{Sc}$ in the extracellular region.

At the center of the cell ($\hat{r} = 0$), the nondimensionalized boundary conditions are

$$\frac{\partial \hat{c}^{UM}}{\partial \hat{r}}(\hat{t}, 0) = 0, \quad \frac{\partial \phi^\omega}{\partial \hat{r}}(\hat{t}, 0) = 0, \quad \hat{u}^s(\hat{t}, 0) = 0, \quad \frac{\partial \hat{p}}{\partial \hat{r}}(\hat{t}, 0) = 0, \tag{3.99}$$

and at the interface ($\hat{r} = 1$) between the cell and the extracellular region, the nondimensionalized interface conditions become:

$$(\lambda_c + 2\mu_c)\left(\frac{\partial \hat{u}^s}{\partial \hat{r}}\right) + \frac{2\lambda_c}{\hat{r}}\hat{u}^s\bigg|_{\hat{r}=1^-} = (\lambda_{Sc} + 2\mu_{Sc})\left(\frac{\partial \hat{u}^s}{\partial \hat{r}}\right) + \frac{2\lambda_{Sc}}{\hat{r}}\hat{u}^s\bigg|_{\hat{r}=1^+}, \tag{3.100}$$

$$-H_A^c\frac{\partial \hat{p}}{\partial \hat{r}} + RTc_0(\phi - 1)\frac{\partial \hat{c}^{UM}}{\partial \hat{r}}\bigg|_{r=1^-} = -H_A^{Sc}\frac{\partial \hat{p}}{\partial \hat{r}} + RTc_0(\phi - 1)\frac{\partial \hat{c}^{UM}}{\partial \hat{r}}\bigg|_{r=1^+}, \tag{3.101}$$

$$-H_A^c\hat{c}^{UM}\frac{\partial \hat{p}}{\partial \hat{r}} + \left(RTc_0(\phi - 1)\hat{c}^{UM} - \frac{D^{\omega(UM)}}{k}\phi^\omega\right)\frac{\partial \hat{c}^{UM}}{\partial \hat{r}}\bigg|_{\hat{r}=1^-} =$$
$$-H_A^{Sc}\hat{c}^{UM}\frac{\partial \hat{p}}{\partial \hat{r}} + \left(RTc_0(\phi - 1)\hat{c}^{UM} - \frac{D^{\omega(UM)}}{k}\phi^\omega\right)\frac{\partial \hat{c}^{UM}}{\partial \hat{r}}\bigg|_{\hat{r}=1^+}, \tag{3.102}$$

$$\frac{\partial \phi^{Sc}}{\partial \hat{r}}(\hat{t}, 1) = 0, \quad \frac{\partial \phi^{LM}}{\partial \hat{r}}(\hat{t}, 1) = 0, \quad \frac{\partial \hat{c}^G}{\partial \hat{r}}(\hat{t}, 1) = 0. \tag{3.103}$$

At the outer boundary of the extracellular region ($\hat{r} = \hat{b}$), the nondimensionalized boundary conditions become:

$$(\lambda_{Sc} + 2\mu_{Sc})\left(\frac{\partial \hat{u}^s}{\partial \hat{r}}\right) + \frac{2\lambda}{\hat{r}}\hat{u}^s\bigg|_{\hat{r}=\hat{b}} = 0, \tag{3.104}$$

$$\hat{p}(\hat{t}, \hat{b}) = 0, \quad \frac{\partial \phi^{Sc}}{\partial \hat{r}}(\hat{t}, \hat{b}) = 0, \quad \frac{\partial \phi^{LM}}{\partial \hat{r}}(\hat{t}, \hat{b}) = 0, \quad \frac{\partial \hat{c}^{UM}}{\partial \hat{r}}(\hat{t}, \hat{b}) = 0, \quad \frac{\partial \hat{c}^{G}}{\partial \hat{r}}(\hat{t}, \hat{b}) = 0. \quad (3.105)$$

Chapter 4

Numerical Methods and Simplified Analytical Solution for Verification

4.1 Introduction

The finite difference method is used to formulate a numerical scheme for the approximate solution of the nondimensionalized system (3.84)-(3.93) subject to the boundary and interface conditions (3.97)-(3.105). The application of the resulting numerical scheme to the simulation of cartilage ECM regeneration results is discussed in Chapter 5. The spatio-temporal PDE model developed in the previous chapter is formulated in two regions and is comprised of several PDEs formulated in terms of multiple unknowns, along with both boundary and interface conditions. Furthermore, numerical stability conditions for this system of governing equations are unknown. For these reasons, an analytical solution for verification of the numerical scheme is also developed in this chapter and used to evaluate accuracy of both the scheme and its implementation in MATLAB.

4.2 Numerical Scheme

We discretize the spatial and temporal domains using fixed step sizes $\Delta \hat{r}$ and $\Delta \hat{t}$, respectively. In the cell region, the non-dimensional spatial step size is taken as $\Delta \hat{r} = 1/m$, where m is prescribed. In the extracellular region, the same spatial step size $\Delta \hat{r}$ is used and the location of the outer boundary b is adjusted to align with the mesh. The temporal step size is taken to be $\Delta \hat{t} = \hat{t}_f / n$, where the final time in the simulation t_f is prescribed.

To approximate the numerical solutions at every time step of the nondimensionalized equations in the cell region (3.84)-(3.87), let $\hat{p}_i^j = \hat{p}(\hat{t}_j, \hat{r}_i)$, $(\hat{u}^s)_i^j = \hat{u}^s(\hat{t}_j, \hat{r}_i)$, $(\phi^\omega)_i^j = \phi^\omega(\hat{t}_j, \hat{r}_i)$, $(\hat{c}^{UM})_i^j = \hat{c}^{UM}(\hat{t}_j, \hat{r}_i)$ for $i = 1, 2, ..., m - 1$, $j = 1, 2, ..., n$, where $\hat{r}_i = i\Delta \hat{r}$, and $\hat{t}_j = j\Delta \hat{t}$. Note

33

that the numerical solution at the current time is at $\hat{t} = \hat{t}_{j+1}$. The discretization of Equation (3.84), which does not explicitly depend on time, is written as

$$-\frac{\partial \hat{p}^{j+1}}{\partial \hat{r}} + \frac{\partial^2 (\hat{u}^s)^{j+1}}{\partial \hat{r}^2} + \frac{2}{\hat{r}} \frac{\partial (\hat{u}^s)^{j+1}}{\partial \hat{r}} - \frac{2}{\hat{r}^2} (\hat{u}^s)^{j+1} = 0. \tag{4.1}$$

For (3.86) the time discretization is handled using backward Euler (implicit) time stepping so that

$$\frac{(\hat{u}^s)^{j+1} - (\hat{u}^s)^j}{\Delta \hat{t}} = R_g^c \frac{\partial \hat{p}^{j+1}}{\partial \hat{r}} - K_g(\phi - 1) \frac{\partial (\hat{c}^{UM})^{j+1}}{\partial \hat{r}}. \tag{4.2}$$

The remaining two governing equations in the cell region (3.85) and (3.87) also depend explicitly on time, but are nonlinear. The nonlinearity in equation (3.85) arises from a product of the evolving porosity and the solid phase velocity. This equation is discretized to yield a linear equation by using a backward Euler scheme for the solid phase velocity and treating the porosity as an explicit term, i.e. evaluated at the previous time step:

$$\frac{(\phi^\omega)^{j+1} - (\phi^\omega)^j}{\Delta \hat{t}} + \left(\frac{\partial}{\partial \hat{r}} + \frac{2}{\hat{r}} \right) \left[((\phi^\omega)^j - 1) \frac{(\hat{u}^s)^{j+1} - (\hat{u}^s)^j}{\Delta \hat{t}} \right] = 0. \tag{4.3}$$

Similarly, (3.87) has nonlinear terms involving products of evolving porosity, solid phase velocity and unlinked ECM concentration. These terms are also discretized to yield a linear discretized equation. Backward Euler is used for terms involving the solid phase velocity and the gradient of the unlinked ECM concentration, and all porosities are treated explicitly, i.e. evaluated at the previous time step, resulting in the discrete equation:

$$\frac{(\phi^\omega)^j (\hat{c}^{UM})^{j+1} - (\phi^\omega)^j (\hat{c}^{UM})^j}{\Delta \hat{t}}$$
$$+ \left(\frac{\partial}{\partial \hat{r}} + \frac{2}{\hat{r}} \right) \left[((\phi^\omega)^j - 1)(\hat{c}^{UM})^j \frac{(\hat{u}^s)^{j+1} - (\hat{u}^s)^j}{\Delta \hat{t}} - (D_r^{UM})^j (\phi^\omega)^j \frac{\partial (\hat{c}^{UM})^{j+1}}{\partial \hat{r}} \right]$$
$$= \hat{k}_{UM} N^* (\hat{c}_*^{UM} - (\hat{c}^{UM})^{j+1})(\phi^\omega)^j. \tag{4.4}$$

Similarly, the techniques used above for both time discretization and treatment of nonlinear terms are applied to discretize the remaining equations (3.88) through (3.93) resulting in the following numerical scheme scheme for $j = 1, 2, ..., n$ at points outside of the cell, i.e. $i = m+1, m+2, ..., M$ (the spatial discretization scheme is addressed at the end of this section):

$$-\frac{\partial \hat{p}^{j+1}}{\partial \hat{r}} + \frac{\partial^2 (\hat{u}^s)^{j+1}}{\partial \hat{r}^2} + \frac{2}{\hat{r}} \frac{\partial (\hat{u}^s)^{j+1}}{\partial \hat{r}} - \frac{2}{\hat{r}^2} (\hat{u}^s)^{j+1} = 0, \tag{4.5}$$

$$\left(\frac{\partial}{\partial \hat{r}} + \frac{2}{\hat{r}}\right)\left[-R_g^{Sc}\frac{\partial \hat{p}^{j+1}}{\partial \hat{r}} + K_g(\phi - 1)\left(\frac{\partial(\hat{c}^{UM})^{j+1}}{\partial \hat{r}} + \frac{\partial(\hat{c}^G)^{j+1}}{\partial \hat{r}}\right) + \frac{(\hat{u}^s)^{j+1} - (\hat{u}^s)^j}{\Delta \hat{t}}\right]$$
$$= -\hat{k}_{Sc}(\phi^{Sc})^{j+1} + \hat{k}_1((\phi^\omega)^j)^2(\hat{c}^G)^j(\hat{c}^{UM})^{j+1}, \quad (4.6)$$

$$\frac{(\phi^{LM})^{j+1} - (\phi^{LM})^j}{\Delta \hat{t}} + \left(\frac{\partial}{\partial \hat{r}} + \frac{2}{\hat{r}}\right)\left((\phi^{LM})^j\frac{(\hat{u}^s)^{j+1} - (\hat{u}^s)^j}{\Delta \hat{t}}\right)$$
$$= \hat{k}_1((\phi^\omega)^j)^2(\hat{c}^G)^j(\hat{c}^{UM})^{j+1}, \quad (4.7)$$

$$\frac{(\phi^{Sc})^{j+1} - (\phi^{Sc})^j}{\Delta \hat{t}} + \left(\frac{\partial}{\partial \hat{r}} + \frac{2}{\hat{r}}\right)\left((\phi^{Sc})^j\frac{(\hat{u}^s)^{j+1} - (\hat{u}^s)^j}{\Delta \hat{t}}\right) = -\hat{k}_{Sc}(\phi^{Sc})^{j+1}, \quad (4.8)$$

$$\frac{(\phi^\omega)^j(\hat{c}^{UM})^{j+1} - (\phi^\omega)^j(\hat{c}^{UM})^j}{\Delta \hat{t}}$$
$$+ \left(\frac{\partial}{\partial \hat{r}} + \frac{2}{\hat{r}}\right)\left[-R_g^{Sc}(\hat{c}^{UM})^j\frac{\partial \hat{p}^{j+1}}{\partial \hat{r}} + \left(K_g(\phi - 1)(\hat{c}^{UM})^j - D_r^{UM}(\phi^\omega)^j\right)\frac{\partial(\hat{c}^{UM})^{j+1}}{\partial \hat{r}}\right]$$
$$+ \left(\frac{\partial}{\partial \hat{r}} + \frac{2}{\hat{r}}\right)\left[(\phi^\omega)^j(\hat{c}^{UM})^j\frac{(\hat{u}^s)^{j+1} - (\hat{u}^s)^j}{\Delta \hat{t}} + K_g(\phi - 1)(\hat{c}^{UM})^j\frac{\partial(\hat{c}^G)^{j+1}}{\partial \hat{r}}\right]$$
$$= -\hat{k}_2((\phi^\omega)^j)^2(\hat{c}^G)^j(\hat{c}^{UM})^{j+1}, \quad (4.9)$$

$$\frac{(\phi^\omega)^j(\hat{c}^G)^{j+1} - (\phi^\omega)^j(\hat{c}^G)^j}{\Delta \hat{t}}$$
$$+ \left(\frac{\partial}{\partial \hat{r}} + \frac{2}{\hat{r}}\right)\left[-R_g^{Sc}(\hat{c}^G)^j\frac{\partial \hat{p}^{j+1}}{\partial \hat{r}} + \left(K_g(\phi - 1)(\hat{c}^G)^j - D_r^G(\phi^\omega)^j\right)\frac{\partial(\hat{c}^G)^{j+1}}{\partial \hat{r}}\right]$$
$$+ \left(\frac{\partial}{\partial \hat{r}} + \frac{2}{\hat{r}}\right)\left[(\phi^\omega)^j(\hat{c}^G)^j\frac{(\hat{u}^s)^{j+1} - (\hat{u}^s)^j}{\Delta \hat{t}} + K_g(\phi - 1)(\hat{c}^G)^j\frac{\partial(\hat{c}^{UM})^{j+1}}{\partial \hat{r}}\right]$$
$$= -\hat{k}_3((\phi^\omega)^j)^2(\hat{c}^{UM})^j(\hat{c}^G)^{j+1}. \quad (4.10)$$

Time discretization of the boundary conditions at $\hat{r} = 0$ are handed as:

$$\frac{\partial(\hat{c}^{UM})^{j+1}}{\partial \hat{r}}(\hat{t}, 0) = 0, \quad \frac{\partial(\phi^\omega)^{j+1}}{\partial \hat{r}}(\hat{t}, 0) = 0, \quad (\hat{u}^s)^{j+1}(\hat{t}, 0) = 0, \quad \frac{\partial(\hat{p})^{j+1}}{\partial \hat{r}}(\hat{t}, 0) = 0, \quad (4.11)$$

and time discretization of the interface conditions at $\hat{r} = 1$ are:

$$(\lambda_c + 2\mu_c)\left(\frac{\partial(\hat{u}^s)^{j+1}}{\partial \hat{r}}\right) + \frac{2\lambda_c}{r}(\hat{u}^s)^{j+1}\bigg|_{r=1^-} =$$
$$(\lambda_{Sc} + 2\mu_{Sc})\left(\frac{\partial(\hat{u}^s)^{j+1}}{\partial \hat{r}}\right) + \frac{2\lambda_{Sc}}{r}(\hat{u}^s)^{j+1}\bigg|_{\hat{r}=1^+}, \quad (4.12)$$

35

$$-H_A^c \frac{\partial (\hat{p})^{j+1}}{\partial \hat{r}} + RTc_0(\phi-1)\frac{\partial (\hat{c}^{UM})^{j+1}}{\partial \hat{r}}\bigg|_{\hat{r}=1^-} =$$
$$-H_A^{Sc}\frac{\partial (\hat{p})^{j+1}}{\partial \hat{r}} + RTc_0(\phi-1)\frac{\partial (\hat{c}^{UM})^{j+1}}{\partial \hat{r}}\bigg|_{\hat{r}=1^+}, \quad (4.13)$$

$$-H_A^c(\hat{c}^{UM})^j\frac{\partial (\hat{p})^{j+1}}{\partial \hat{r}} + \left(RTc_0(\phi-1)(\hat{c}^{UM})^j - \frac{(D^{\omega(UM)})^j}{k}(\phi^\omega)^j\right)\frac{\partial (\hat{c}^{UM})^{j+1}}{\partial \hat{r}}\bigg|_{\hat{r}=1^-} =$$
$$-H_A^{Sc}(c^{UM})^j\frac{\partial (\hat{p})^{j+1}}{\partial \hat{r}} + \left(RTc_0(\phi-1)(\hat{c}^{UM})^j - \frac{(D^{\omega(UM)})^j}{k}(\phi^\omega)^j\right)\frac{\partial (\hat{c}^{UM})^{j+1}}{\partial \hat{r}}\bigg|_{\hat{r}=1^+}, \quad (4.14)$$

$$\frac{\partial (\phi^{Sc})^{j+1}}{\partial \hat{r}}(\hat{t},1) = 0, \quad \frac{\partial (\phi^{LM})^{j+1}}{\partial \hat{r}}(\hat{t},1) = 0, \quad \frac{\partial (\hat{c}^{G})^{j+1}}{\partial \hat{r}}(\hat{t},1) = 0. \quad (4.15)$$

At the outer boundary of the extracellular region $(\hat{r} = \hat{b})$, the discretized boundary conditions become:

$$(\lambda_{Sc} + 2\mu_{Sc})\left(\frac{\partial (\hat{u}^s)^{j+1}}{\partial \hat{r}}\right) + \frac{2\lambda_{Sc}}{\hat{r}}(\hat{u}^s)^{j+1}\bigg|_{\hat{r}=\hat{b}} = 0, \quad (4.16)$$

$$(\hat{p})^{j+1}(\hat{t},\hat{b}) = 0, \quad \frac{\partial (\phi^{Sc})^{j+1}}{\partial \hat{r}}(\hat{t},\hat{b}) = 0, \quad \frac{\partial (\phi^{LM})^{j+1}}{\partial r}(\hat{t},\hat{b}) = 0, \quad (4.17)$$

$$\frac{\partial (\hat{c}^{UM})^{j+1}}{\partial \hat{r}}(\hat{t},\hat{b}) = 0, \quad \frac{\partial (\hat{c}^{G})^{j+1}}{\partial r}(\hat{t},\hat{b}) = 0. \quad (4.18)$$

It should be noted that, for simplicity of the presentation above, finite difference approximations for the spatial derivatives were not shown. All spatial derivatives above were discretized using a second order difference (central differences) for the second order derivatives and a first-order scheme for all first derivatives.

4.3 Simplified Model for Verification

In this section the full non-dimensional model is reduced to a simplified model that admits an analytical solution. This analytical solution is applied to verify the accuracy and implementation of the numerical scheme that was formulated in the previous section, with an emphasis on temporal aspects of the problem.

For the cell region, both the solid displacement $\hat{u}^s(\hat{t},\hat{r})$ and pore pressure $\hat{p}(\hat{t},\hat{r})$ are assumed to be zero. The unlinked matrix concentration is assumed to depend only on time, so that $\partial \hat{c}^{UM}/\partial \hat{r} = 0$. Based on these assumptions, the equations (3.84) and (3.86) are automatically satisfied. The remaining equations to be solved in the cell region are the reduced versions of

(3.85) and (3.87) which are

$$\frac{\partial \phi^\omega}{\partial \hat{t}} = 0, \tag{4.19}$$

$$\frac{\partial \hat{c}^{UM}}{\partial \hat{t}} = \hat{k}_{UM} N^* (\hat{c}_*^{UM} - \hat{c}^{UM}). \tag{4.20}$$

For the extra-cellular region, both solid displacement and pore pressure are assumed to be zero, i.e. $\hat{u}^s(\hat{t}, \hat{r}) = 0$, and $\hat{p}(\hat{t}, \hat{r}) = 0$. It is also assumed that the growth factor concentration ($\hat{c}^G$) is constant, and that the scaffold does not degrade, i.e. $k_{Sc} = 0$. Lastly, we assume that linked matrix does not form from unlinked matrix by taking $k_{UL} = 0$ and the osmotic coefficient ϕ is taken to be 1. These assumptions lead to satisfaction of (3.88), (3.89), and (3.93) and the remaining equations (3.90), (3.91), and (3.92) reduce to:

$$\frac{\partial \phi^{LM}}{\partial \hat{t}} = 0 \tag{4.21}$$

$$\frac{\partial \phi^{Sc}}{\partial \hat{t}} = 0 \tag{4.22}$$

$$\frac{\partial \hat{c}^{UM}}{\partial \hat{t}} + \left(\frac{\partial}{\partial \hat{r}} + \frac{2}{\hat{r}} \right) \left[-D_r^{UM} \frac{\partial \hat{c}^{UM}}{\partial \hat{r}} \right] = 0 \tag{4.23}$$

The initial conditions and boundary conditions at $\hat{r} = 0$ and $\hat{r} = 1$ are based on those for the non-dimensionlized model in section 3.5. The interface conditions (3.100), (3.101), and (3.103) are automatically satisfied, while the interface condition (3.102) mathematically reduces to:

$$\left. \frac{\partial \hat{c}^{UM}}{\partial \hat{r}} \right|_{\hat{r}=1+} = 0. \tag{4.24}$$

However, since unlinked matrix concentration in the cell region is assumed to depend only on time, the condition for flux continuity across the interface is replaced by a condition for continuity of concentration that supplies cell-synthesized unlinked matrix to the extracellular region via the modified interface condition:

$$\hat{c}^{UM}\big|_{\hat{r}=1+} = \hat{c}^{UM}\big|_{\hat{r}=1-}. \tag{4.25}$$

Lastly, in the reduced model, the outer boundary of the extracellular region $\hat{b}$ is chosen to have the dimensionless value 2. The full set of governing equations for the reduced model is summarized below.

$$\begin{cases} \dfrac{\partial \phi^\omega}{\partial \hat{t}} = 0 & \hat{t} \geq 0, \quad 0 \leq \hat{r} \leq 1 \\ \phi^\omega(0, \hat{r}) = (\phi_0^\omega)^c & 0 \leq \hat{r} \leq 1 \end{cases} \tag{4.26}$$

37

$$\begin{cases} \dfrac{\partial(\hat{c}^{UM})}{\partial \hat{t}} = \hat{k}_{UM}N^*(\hat{c}_*^{UM} - \hat{c}^{UM}) & \hat{t} \geq 0, \quad 0 \leq \hat{r} \leq 1 \\ \hat{c}^{UM}(0, \hat{r}) = 0 & 0 \leq \hat{r} \leq 1 \end{cases} \quad (4.27)$$

$$\begin{cases} \dfrac{\partial \phi^{LM}}{\partial \hat{t}} = 0 & \hat{t} \geq 0, \quad 1 \leq \hat{r} \leq 2 \\ \phi^{LM}(0, \hat{r}) = 0 & 1 \leq \hat{r} \leq 2 \end{cases} \quad (4.28)$$

$$\begin{cases} \dfrac{\partial \phi^{Sc}}{\partial \hat{t}} = 0 & \hat{t} \geq 0, \quad 1 \leq \hat{r} \leq 2 \\ \phi^{Sc}(0, \hat{r}) = \phi_0^{Sc} & 1 \leq \hat{r} \leq 2 \end{cases} \quad (4.29)$$

$$\begin{cases} \dfrac{\partial \hat{c}^{UM}}{\partial \hat{t}} + \left(\dfrac{\partial}{\partial \hat{r}} + \dfrac{2}{\hat{r}}\right)\left[-D_r^{UM}\dfrac{\partial \hat{c}^{UM}}{\partial \hat{r}}\right] = 0 & \hat{t} \geq 0, \quad 1 \leq \hat{r} \leq 2 \\ \hat{c}^{UM}(0, \hat{r}) = 0 & 1 \leq \hat{r} \leq 2 \\ \hat{c}^{UM}|_{\hat{r}=1^+} = \hat{c}^{UM}|_{\hat{r}=1^-}, \quad \dfrac{\partial \hat{c}^{UM}}{\partial \hat{r}}(\hat{t}, 2) = 0 & \hat{t} \geq 0 \end{cases} \quad (4.30)$$

We observe that the reduced model effectively treats the cell region solution as a reaction, i.e. variables are independent of $\hat{r}$, that interacts with a diffusion model for unlinked matrix concentration in the extracellular region.

4.4 Analytical Solution of The Simplified Model

Equations (4.26), (4.27), (4.28), and (4.29) are ODEs that admit the following analytical solutions:

$$\phi^\omega(\hat{t}, \hat{r}) = 1 - \phi_0^s, \quad \hat{c}^{UM}(\hat{t}, \hat{r}) = \hat{c}_*^{UM} - \hat{c}_*^{UM}e^{-N^*k_{UM}\hat{t}}, \quad \phi^{LM}(\hat{t}, \hat{r}) = 0, \quad \phi^{Sc}(\hat{t}, \hat{r}) = \phi_0^{Sc}, \quad (4.31)$$

respectively.

To find the analytical solution of (4.30) the method of separation of variables method was used. For clarity of the presentation, the "hat" notation is dropped for the remainder of this section.

Assume that

$$c^{UM}(t, r) = \frac{u(t, r)}{r} \quad (4.32)$$

Substituting (4.32) into (4.30) we obtain

$$
\begin{cases}
\dfrac{\partial u}{\partial t} - D_r^{UM}\dfrac{\partial^2 u}{\partial r^2} = 0 & t \geq 0, \quad 1 \leq r \leq 2 \\
u(0,r) = 0 & 1 \leq r \leq 2 \\
u(t,1) = c_*^{UM} - c_*^{UM}e^{-N^*k_{UM}t}, \quad 2\dfrac{\partial u}{\partial r}(t,2) - u(t,2) = 0 & t \geq 0
\end{cases}
\tag{4.33}
$$

(4.33) is a diffusion equation with nonhomogeneous boundary conditions. It can be transformed into a diffusion equation with homogeneous boundary conditions via the change of variable

$$
u(t,r) = v(t,r) + (c_*^{UM} - c_*^{UM}e^{-N^*k_{UM}t})r.
\tag{4.34}
$$

Substituting (4.34) into (4.33) we obtain

$$
\begin{cases}
\dfrac{\partial v}{\partial t} - D_r^{UM}\dfrac{\partial^2 v}{\partial r^2} = -(c_*^{UM}N^*k_{UM}e^{-N^*k_{UM}t})r & t \geq 0, \quad 1 \leq r \leq 2 \\
v(0,r) = 0 & 1 \leq r \leq 2 \\
v(t,1) = 0, \quad 2\dfrac{\partial v}{\partial r}(t,2) - v(t,2) = 0 & t \geq 0
\end{cases}
\tag{4.35}
$$

Note that the PDE above is a nonhomogeneous diffusion equation but now has homogeneous boundary conditions. The solution is assumed to be of the form $v(t,r) = R(r)T(t)$. By ignoring the source term in (4.35), we first find the eigenvalues and eigenfunctions of $R(r)$ by solving the problem

$$
\begin{cases}
R'' + \alpha R = 0 & 1 \leq r \leq 2 \\
R(1) = 0, \quad 2R'(2) - R(2) = 0.
\end{cases}
\tag{4.36}
$$

When $\alpha < 0$, we write $\alpha = -\lambda^2$ and the equation for R becomes

$$
R'' - \lambda^2 R = 0,
$$

which has general solution

$$
R(r) = c_1 \cosh(\lambda r) + c_2 \sinh(\lambda r).
$$

The condition $R(1) = 0$ gives

$$
c_1 = -\frac{\sinh(\lambda)}{\cosh(\lambda)}c_2.
$$

The value of c_1 resulting from enforcing the boundary condition $2R'(2) - R(2) = 0$ above gives

$$
c_2[-\sinh(\lambda)(2\lambda\sinh(2\lambda) - \cosh(2\lambda)) + \cosh(\lambda)(2\lambda\cosh(2\lambda) - \sinh(2\lambda))] = 0.
$$

If $c_2 \neq 0$, it can be readily shown (e.g. using MAPLE) that the term inside the bracket is never zero for $\lambda < 0$. Thus, $c_2 = 0$ and the case $\alpha < 0$ yields only trivial solutions.

Similarly in the case $\alpha = 0$, the differential equation reduces to $R'' = 0$ with general solution $R(r) = c_1 r + c_2$. The only way to satisfy the boundary conditions on R is to take $c_1 = c_2 = 0$ which again leads to the trivial solution $R = 0$. In the only remaining case we have

$$\alpha = \lambda^2 > 0.$$

The corresponding boundary value problem in R is

$$
\begin{cases}
R'' + \lambda^2 R = 0 & 1 \leq r \leq 2 \\
R(1) = 0, \quad 2R'(2) - R(2) = 0.
\end{cases}
$$

The general solution of the differential equation is

$$R(r) = c_1 \sin(\lambda r) + c_2 \cos(\lambda r).$$

The condition $R(1) = 0$ gives

$$c_1 = -\frac{\cos(\lambda)}{\sin(\lambda)} c_2$$

Substituting this expression for c_1 into the second boundary condition $2R'(2) - R(2) = 0$ gives

$$c_2 \left[-\cos(\lambda)(2\lambda \cos(2\lambda) - \sin(2\lambda)) - \sin(\lambda)(2\lambda \sin(2\lambda) - \cos(2\lambda)) \right] = 0.$$

Assuming that $c_2 \neq 0$, we obtain the condition

$$-\cos(\lambda)(2\lambda \cos(2\lambda) - \sin(2\lambda)) - \sin(\lambda)(2\lambda \sin(2\lambda) - \cos(2\lambda)) = 0.$$

This equation has an infinite number of positive solutions $\lambda_1, \lambda_2, \dots..$ While we do not have explicit formulas for the λ_n, approximate numerical values of the λ_n's can be determined using MAPLE. Assuming that these eigenvalues can be computed, the solutions $R(r)$ of (4.36) are eigenfunctions that can be written as:

$$R_n(r) = \sin(\lambda_n r) - \tan(\lambda_n) \cos(\lambda_n r), \quad n = 1, 2, \dots,$$

and the solution of (4.35) will be of the form

$$v(t, r) = \sum_{n=1}^{\infty} (\sin(\lambda_n r) - \tan(\lambda_n) \cos(\lambda_n r)) T_n(t). \tag{4.37}$$

40

Substituting (4.37) into (4.35) yields

$$
\sum_{n=1}^{\infty} (\sin(\lambda_n r) - \tan(\lambda_n)\cos(\lambda_n r))T_n'(t) -
$$

$$
D_r^{UM} \sum_{n=1}^{\infty} (-\lambda_n^2 \sin(\lambda_n r) + \lambda_n^2 \tan(\lambda_n)\cos(\lambda_n r))T_n(t) = -(c_*^{UM} N^* k_{UM} e^{-N^* k_{UM} t})r. \quad (4.38)
$$

Assuming that the right hand side of (4.35) has the same series form as $v(t,r)$, we obtain

$$
-(\hat{c}_*^{UM} N^* k_{UM} e^{-N^* k_{UM} t})r = \sum_{n=1}^{\infty} (\sin(\lambda_n r) - \tan(\lambda_n)\cos(\lambda_n r))F_n(t). \quad (4.39)
$$

This implies that

$$
F_n(t) = K_n e^{-N^* k_{UM} t}, \quad (4.40)
$$

where K_n is a constant which can be written as

$$
K_n = \frac{\int_1^2 -(c_*^{UM} N^* k_{UM})r(\sin(\lambda_n r) - \tan(\lambda_n)\cos(\lambda_n r))dr}{\int_1^2 (\sin(\lambda_n r) - \tan(\lambda_n)\cos(\lambda_n r))^2 dr}. \quad (4.41)
$$

Substituting (4.39) into (4.38) gives

$$
\begin{cases} T_n'(t) + D_r^{UM} \lambda_n^2 T_n(t) = F_n(t) & t \geq 0 \\ T_n(0) = 0, \end{cases} \quad (4.42)
$$

which is first a order ordinary differential equation. It can be solved for every positive integer $n \geq 1$ and the solution is

$$
T_n(t) = \frac{K_n(e^{-D_r^{UM} \lambda_n^2 t} - e^{-N^* k_{UM} t})}{D_r^{UM} \lambda_n^2 - N^* k_{UM}}. \quad (4.43)
$$

Then $v(t,r)$, the solution of (4.35), can be written by substituting (4.43) into (4.37) to obtain

$$
v(t,r) = \sum_{n=1}^{\infty} (\sin(\lambda_n r) - \tan(\lambda_n)\cos(\lambda_n r))\frac{K_n(e^{-D_r^{UM} \lambda_n^2 t} - e^{-N^* k_{UM} t})}{D_r^{UM} \lambda_n^2 - N^* k_{UM}}. \quad (4.44)
$$

After finding the $v(t, r)$ we can write $u(t, r)$ as

$$u(t, r) = (c_*^{UM} - c_*^{UM} e^{-N^* k_{UM} t}) r +$$
$$\sum_{n=1}^{\infty} (\sin(\lambda_n r) - \tan(\lambda_n) \cos(\lambda_n r)) \frac{K_n (e^{-D_r^{UM} \lambda_n^2 t} - e^{-N^* k_{UM} t})}{D_r^{UM} \lambda_n^2 - N^* k_{UM}}. \quad (4.45)$$

Lastly, the solution of (4.35) is thus obtained as:

$$c^{UM}(t, r) = (c_*^{UM} - c_*^{UM} e^{-N^* k_{UM} t}) +$$
$$\sum_{n=1}^{\infty} (\sin(\lambda_n r) - \tan(\lambda_n) \cos(\lambda_n r)) \frac{K_n (e^{-D_r^{UM} \lambda_n^2 t} - e^{-N^* k_{UM} t})}{(D_r^{UM} \lambda_n^2 - N^* k_{UM}) r} \quad (4.46)$$

4.5 Verification of Numerical Scheme Using The Simplified Model

(a)   (b)
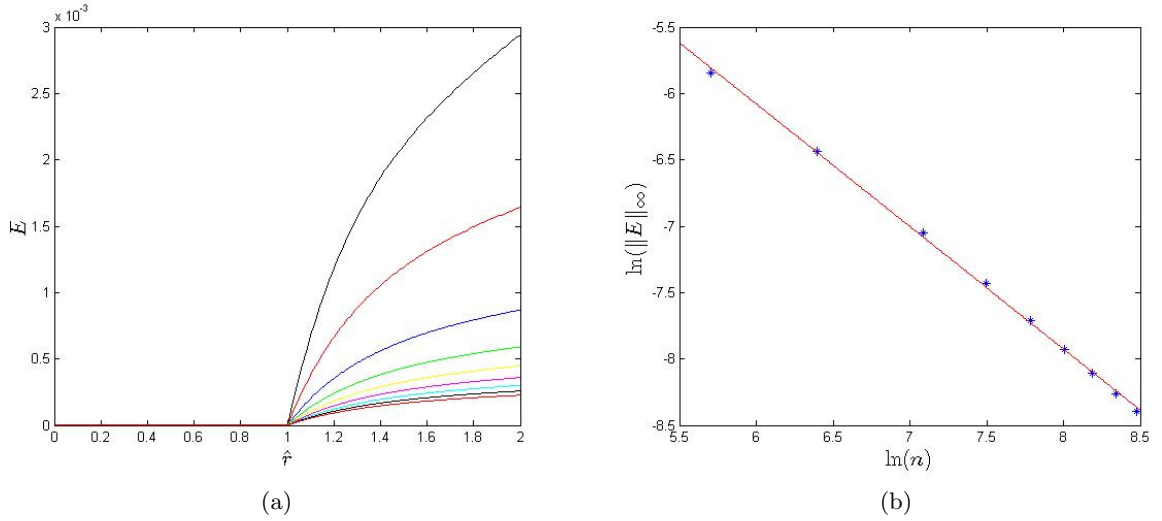
Figure 4.1: Evaluation of the error between the numerical and simplified analytical solutions: (a) Absolute value of the error as the mesh is refined based on the choices in Table 4.1 shown at the time t=23.6 days, (b) a log-log plot of the infinity norm of the error between the numerical and simplified analytical solutions at the time t=23.6 days demonstrating a first-order rate of convergence.

We used the simplified model developed in the previous sections to verify accuracy and implementation of the temporal aspects of the numerical method. The MATLAB code for

Table 4.1: Mesh sizes and infinity-norm error between the numerical and simplified analytical solutions at the time $t = 23.6$ days.

m	color	$||E||_\infty$
50	Black	0.0029
100	Red	0.0016
200	Blue	8.6923×10^{-4}
300	Green	5.9061×10^{-4}
400	Yellow	4.4716×10^{-4}
500	Magenta	3.5976×10^{-4}
600	Cyan	3.0092×10^{-4}
700	Black	2.5863×10^{-4}
800	Red	2.2675×10^{-4}

the full model, that was implemented based on the nondimensionlized model in Section 3.5, was reduced to simulate the simplified model developed in this chapter. Note that the interface conditions in the nondimensionlized model given by (3.100)-(3.103) were replaced by a simplified boundary condition, as outlined in section 4.3, due to the fact the simplified model in the cell region was independent of $\hat{r}$. All model parameters that appear in (4.27) and (4.30) were assumed to have the same values that are used in the baseline case presented in the next chapter (see Section 5.2 and Tables 5.1-5.3).

Let m and n to be the number of steps with respect to space ($\hat{r}$) and time ($\hat{t}$). For the simplified model, the choice $n = 6m$ yielded simulations that all exhibited numerical convergence as the mesh was refined. Let $\hat{c}^{UM}$ and $\tilde{c}^{UM}$ to be the analytic solution and the numerical solution respectively. Define

$$E = \left| \hat{c}^{UM} - \tilde{c}^{UM} \right|$$

and

$$||E||_\infty = \max_{0 \le \hat{r} \le 1} \left| \hat{c}^{UM} - \tilde{c}^{UM} \right|.$$

To illustrate numerical convergence rates of the method, E was found locally when $\hat{t} = 2.5773 \times 10^7$ (i.e. $t = 23.6$ days) and is plotted versus $\hat{r}$ with $n = 6m$ in Figure 4.1a based on the mesh sizes specified in Table 4.1 The numerical discretization in time, developed in section 4.1, exhibits numerical convergence that is first order in time as seen in Figure 4.1b.

Chapter 5

Parametric Analysis and Results

5.1 Introduction

In this chapter, the spatio-temporal PDE continuum mixture model for cartilage extracellular matrix regeneration in the local environment of a single cell is applied in a parametric analysis. The investigation focuses on the effects of evolving scaffold porosity on accumulation of linked ECM in the (extracellular) region surrounding the cell. The associated governing equations, along with the interface and boundary conditions developed in Chapter 3, are solved using the numerical discretization scheme outlined in Sec. 4.2. Results for evolution of the primary variables in the model are illustrated in terms of a baseline set of parameter values. Several of these values are fixed based on known physical or chemical properties of components of the cell-scaffold system. Other parameter values that govern the physiological interactions of system components are calibrated to yield ECM regeneration times that are on realistic scales for tissue engineered articular cartilage. e.g. from a few weeks to several months.

5.2 Baseline Model Parameters

Parameters in the spatio-teporal PDE model described in Chapter 3 can be separated into three main categories: biophysical parameters, scaffold design parameters, and physiological parameters. Although there is a fourth group which are geometric parameters, in a one-dimensional model the primary geometric parameter is the cell radius whose value is well known for chondrocytes, e.g. $a = 5\text{x}10^{-6}$m is a typical radius of a chondrocyte [28]. In the non-dimensional model (Sec. 3.5), this cell radius is used in setting $\hat{r} = 1$ as the location of the cell-scaffold interface. Based on this choice, the (far-field) outer boundary for the extracellular region is taken as $\hat{r} = 2$. Also, there are several constants that have fixed values independent of interactions within the cell-scaffold system. These are the universal gas constant ($R = 8.31432$ J/mol $\cdot$ K),

the absolute ambient temperature taken as $T = 298$ K and the osmotic coefficient ($\phi = 1$) for ideal solutions [41]. In addition, the nutrient concentration required to sustain biosynthesis in living cells is fixed at a value of $N^* = 0.1$ mol/L [19]. Note that diffusion of these nutrients was not modeled explicitly since these solutes are small relative to unlinked ECM and growth factors and, as a result, their diffusion times are relatively fast.

5.2.1 Biophysical Parameters

In our model, biophysical parameters refer to parameters that govern passive material properties of the system constituents and diffusive transport times. In referring to diffusivities of unbound solutes, it is important to note the distinction between values in free solution versus those in a porous mixture. Recall that the parameters D^{UM} and D^{G} denote the diffusivity of unlinked ECM and the growth factor, respectively, in free solution. D_0 is the reference diffusivity used to nondimensionalize the other diffusivity parameters in (3.82) and was chosen to be the same as D^{UM}. In our system, we assume that the diffusivity of the growth factor (D^{G}) is significantly less than the diffusivity of the unlinked ECM (D^{UM}) since diffusivity increases as particle size decreases, and the molecular weight of unlinked ECM (M_{UM}) is assumed to be significantly less than that of the growth factor (M_G). The choice $D_0 = D^{UM}$ was made since unlinked ECM is the smallest diffusing solute modeled in our system and, thus, the characteristic times for slower phenomena such as diffusion of larger solutes, scaffold degradation and ECM linking will occur on a larger time scale than $O(1)$. Specific values for each of the diffusivities were chosen based on values reported by Mauck et al. ([35],Table 1).

The elastic Lamé coefficients of the solid phase (λ, μ) were related to the Young's modulus (E) and the Poisson's ratio (ν) in equation (2.29). For the cell, the values (E_c, ν_c) = (1000 Pa, 0.35) were chosen. The value of the aggregate modulus $H_A^c = \lambda_c + 2\mu_c$ can also be determined using equation (2.29) and (3.83). In the extracellular region, which is initially scaffold, the values (E_{Sc}, ν_{Sc}) = (10E_c, 0.1) were chosen. Lastly, the true density of linked matrix (ρ_T^{LM}) was fixed at a value of 1.3x10^3 kg/L [48]. The choice of all biophysical parameter values in the baseline case is summarized in Table 5.1.

5.2.2 Scaffold Design Parameters

The scaffold design parameters include the initial scaffold solid volume fraction (ϕ_0^{Sc}) as well as the hydraulic permeability (k). The initial scaffold porosity was chosen to be 98% corresponding to a value of $\phi_0^{Sc} = 0.02$ [19]. In the parametric analysis conducted later in this chapter, the effects of varying the value of ϕ_0^{Sc} on the spatial-temporal accumulation of linked ECM in the region around the cell is considered. The hydraulic permeability constant was chosen to have a value $k = 51.4$x10^{-15} m^4/N · s, based on [35] (Table 2). The scaffold design parameter values

Table 5.1: Biophysical parameter values that are used to analyze the spatio-temporal PDE model in the baseline case.

Parameter	Description	Value	Ref.
D^{UM}	Diffusivity of unlinked matrix in free solution	3.16×10^{-10} (m^2/s)	[17],[35]
D^{G}	Diffusivity of the growth factor in free solution	6.97×10^{-11} (m^2/s)	[17],[35]
D_0	Reference diffusivity	D^{UM}	[35]
M_{UM}	Molecular weight of unlinked matrix	20 (kg/mol)	[35]
M_G	Molecular weight of growth factor	67 (kg/mol)	[35]
(E_c, ν_c)	Young's modulus and Poisson's ratio for the cell	$(1000 \, \text{Pa}, 0.35)$	
λ_c	First elastic Lamé coefficient for the cell	$\dfrac{E_c \nu_c}{(1 + \nu_c)(1 - 2\nu_c)}$	
μ_c	Second elastic Lamé coefficient (shear modulus) for the cell	$\dfrac{E_c}{2(1 + \nu_c)}$	
(E_{Sc}, ν_{Sc})	Young's modulus and Poisson's ratio for the scaffold (extracellular region)	$(10E_c, 0.1)$	
λ_{Sc}	First elastic Lamé coefficient for the scaffold (extracellular region)	$\dfrac{E_{Sc} \nu_{Sc}}{(1 + \nu_{Sc})(1 - 2\nu_{Sc})}$	
μ_{Sc}	Second elastic Lamé coefficient (shear modulus) for the scaffold (extracellular region)	$\dfrac{E_{Sc}}{2(1 + \nu_{Sc})}$	
ρ_T^{LM}	True density of linked matrix	1.3×10^3 (kg/L)	[48]

Table 5.2: Parameter values for the scaffold that are used to analyze the spatio-temporal PDE model in the baseline case.

Parameter	Description	Value	Ref.
ϕ_0^{Sc}	Initial scaffold solid volume fraction	0.02	[19]
k	Hydraulic permeability	$51.4\text{x}10^{-15}$ $(\text{m}^4/\text{N}\cdot\text{s})$	[35]

for the baseline case are summarized in Table 5.2.

5.2.3 Physiological Parameters

We refer to physiological parameters in our model as those that govern phenomena regulated by the biological cells in a tissue engineered construct. The first important parameter is the critical unlinked matrix concentration $\hat{c}_*^{UM} = c_*^{UM}/c_0$. This parameter is based on the phenomena of product inhibition in tissue engineered cartilage [8]. In this context, product inhibition refers to the observation that the rate of cell-mediated biosynthesis of ECM components slows down as the total amount produced increases. The specific formulation in our model is based on the hypothesis that the cell detects the concentration of unlinked matrix in the fluid phase within the cell. The choice of $\hat{c}_*^{UM}$ was made by taking the critical unlinked matrix density $(\bar{\rho}_*^{UM})$ in (3.18) and converting it to a concentration in moles of solute per volume of solvent, using the molecular weight of unlinked matrix (M_{UM}), where the solvent is the fluid phase of the mixture. Note that the characteristic unlinked matrix concentration used in our nondimensionalization (3.82) was taken to be $c_0 = 0.1$ M [64].

As was the case for the temporal (ODE) model, the rates for assembly and cross-linking of unlinked matrix dissolved in the fluid phase into bound, linked ECM was modeled as a Gaussian function of the solid phase volume fraction or, equivalently, the evolving porosity in the mixture. Specifically, the parameters ϕ_*^s and σ in (3.47) determine the mean value of the porosity (at which matrix assembly rates are a maximum) and the standard deviation of these rates in a normal distribution, respectively. The values of these parameters were chosen as $\phi_*^s = 0.04$ and $\sigma = 0.01$ for the baseline case. (It is noted that mature, healthy cartilage has a solid phase volume fraction that is roughly 20%.)

Lastly, the scaffold degradation rate (k_{Sc}), the cell-mediated rate for unlinked ECM synthesis (k_{UM}), and the maximum linking rate $(k_{UL}\ (\text{s}\cdot\text{kg/L})^{-1})$ in the ECM linking model (3.47) need to be specified. Like the parameters described in the previous paragraph, these values depend on physiological interactions between the cells and biological macromolecules or biocompatible polymers in the system. Their values are difficult to measure directly via experiments but

Table 5.3: Physiological parameter values that are used to analyze the spatio-temporal PDE model in the baseline case.

Parameter	Description	Value	Ref.
c_*^{UM}	Critical unlinked matrix concentration	$1/M_{UM}$ (mol/L)	[19]
c_0	Basic scale of concentration	0.1 M	[64]
(ϕ_*^s, σ)	Gaussian linking model parameters defining regimes in which rates for formation of linked ECM are enhanced or inhibited	$(0.04, 0.01)$	
k_{Sc}	Scaffold degradation rate	3.858×10^{-7} (s)$^{-1}$	[19]
k_{UM}	Unlinked ECM synthesis rate	8.102×10^{-4} (s $\cdot$ mol/L)$^{-1}$	[19]
k_{UL}	Maximum linking rate	$100 k_{UM}$ (s $\cdot$ kg/L)$^{-1}$	

could, ultimately, be obtained using parameter estimation based on analysis of experimental data for tissue engineered constructs. The choice of values for these parameters was based on an assumption that the processes they model occur on slower time scales relative to diffusive time scales for unbound solutes in the model. The maximum linking rate (k_{UL}) was assumed to be the fastest of all these rates and chosen to be $(100 * k_{UM})$ where $k_{UM} = 8.1019 \times 10^{-4}$ (s $\cdot$ mol/L)$^{-1}$. The scaffold degradation rate (k_{Sc}) was chosen to be 3.858×10^{-7} (s)$^{-1}$ and both k_{UM} and k_{Sc} values are taken from [19]. Note that the nondimensional formulas for (k_{Sc}) and (k_{UM}) are given by (3.95). Dimensional values for all physiological parameters in the baseline case are summarized in Table 5.3.

5.3 Mesh Refinement Study

Prior to conducting a parametric analysis, the numerical solution for the baseline case was evaluated for numerical convergence in a mesh refinement study. The mesh was systematically refined with respect to $\hat{r}$ by taking the associated number of spatial points m to be 50, 100, 200, 400, and 800. In each case, the number of time steps was fixed at $n = 6400$. The numerical solution on the finest mesh, i.e. $m = 800$, was chosen as the "true" solution with respect to which error norms were computed. Specifically, the average L_2 norm error was calculated for the numerical solutions in the cases $m = 50, 100, 200,$ and 400, i.e. relative to the finer-scale solution at $m = 800$. The results are summurized in Table 5.4. The log-log plot of the average L_2 error is observed to exhibit numerical convergence that is roughly second order in space (i.e. with respect to $\hat{r}$).

Table 5.4:   Mesh sizes and average L_2 error between the fine-scale numerical solution at $m = 800$ and the coarser numerical solutions at $m = 50$, 100, 200, and 400, where $n = 6400$.

(m, m)	$(L_2 \text{ error})/mn$
(800,50)	$2.4532\text{x}10^{-6}$
(800,100)	$8.1982\text{x}10^{-7}$
(800,200)	$2.4997\text{x}10^{-7}$
(800,400)	$5.9080\text{x}10^{-8}$

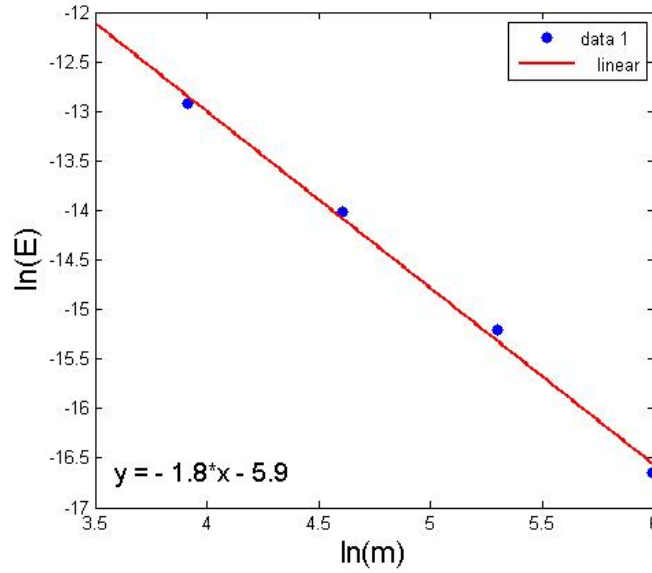
Figure 5.1:   A log-log plot of the average L_2 error between the numerical solution at $m = 800$ and the numerical solutions at $m = 50$, 100, 200, and 400 demonstrating a roughly second order rate of convergence.

5.4 Simulations for the Baseline Case

Based on the mesh refinement study described in the previous section, the value $m = 200$ was chosen for all simulations shown in this chapter. The parameter values summarized in Tables 5.1, 5.2, and 5.3 were used to define the baseline case for the model (3.84)-(3.93) subject to the boundary and interface conditions (3.97)-(3.105). The numerical solution of these governing equations was carried out using the finite difference scheme that was detailed in Section 4.2. Spatio-temporal results for the baseline case are shown for all primary quantities of interest in the model. Specifically, these are the Gaussian model for ECM linking $f(\phi^s)$ (Figure 5.2), linked matrix volume fraction ϕ^{LM} (Figure 5.6), scaffold volume fraction (Figure 5.5), total solid phase volume fraction ϕ^s (Figure 5.3), porosity $\phi^w = 1 - \phi^s$ (Figure 5.4), unlinked matrix concentration $\hat{c}^{UM}$ (Figure 5.7), and the growth factor concentration $\hat{c}^G$ (Figure 5.8).

Figure 5.2a illustrates the relation for dependence of the Gaussian model of ECM linking rate (3.47) on the solid volume fraction ϕ^s. Its variation with spatial location in the extracellular region ($\hat{r} > 1$) is shown in Figure 5.2b, where the arrow indicates the direction of increasing $\hat{r}$. Recall that the Gaussian model was chosen to capture phenomena of low linking rates in the case of very low density scaffold polymer structure and the case of relatively high density polymer structure that may inhibit assembly and cross-linking of ECM constituents. In the baseline case, we observe that the peak rate for formation and accumulation of linked ECM occurs around $\hat{t} = 3\text{x}10^7$ (i.e $t = 27.5$ days) at points closest to the cell. After this time, the Gaussian profile exhibits a front-like propagation away from the cell into the extracellular region as accumulation of ECM increases the value of the solid phase volume fraction ϕ^s behind the front.

The spatial and temporal evolution of the solid volume fraction (ϕ^s) and the mixture porosity ($\phi^w = 1 - \phi^s$) are shown in Figure 5.3 and Figure 5.4, respectively. Spatial profiles indicate that the extracellular porosity, which is initially uniform, begins to decrease rapidly in regions closer to the cell boundary (Figure 5.4a). However, at later times, as the Gaussian front in the linking model advances outward, the porosity returns to being spatially uniform as it decreases to a steady-state value near 92%. Temporal profiles shown in Figure 5.4b demonstrate that the porosity in extracellular regions closest to the cell drops rapidly relative to those further away from the cell boundary, where the arrow indicates the direction of increasing $\hat{r}$. For the solid volume fraction (ϕ^s), spatial (Figure 5.3a) and temporal (Figure 5.3b) evolution profiles exhibit an opposite response due to the relation with porosity $\phi^s = 1 - \phi^w$. It can be observed that the dimensionless time of $\hat{t} \approx 2$ at which the first Gaussian peak is achieved for the linking rate (and closest to the cell boundary) (Figure 5.2b) corresponds roughly to the time at which the temporal profiles of ϕ^s begin to exhibit a dependence on spatial location $\hat{r}$ (Figure 5.3b). The spatial and temporal evolution of the volume fraction of scaffold (ϕ^{Sc}) are shown in Figure 5.5.
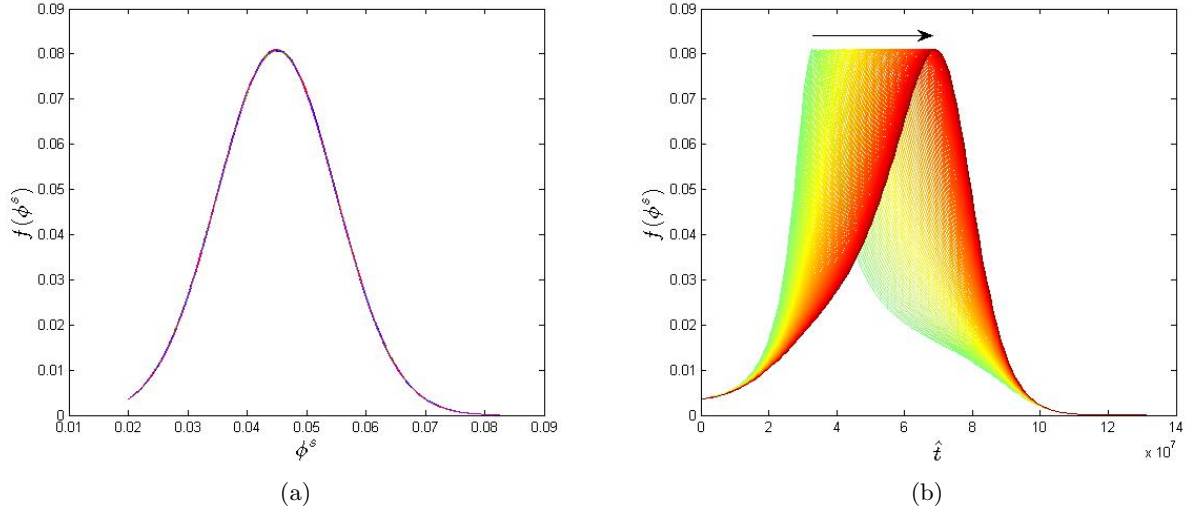
Figure 5.2: Simulations of the Gaussian model for the ECM linking rate $f(\phi^s)$ in the baseline case: (a) plot of $f(\phi^s)$ versus the solid phase volume fraction to ϕ^s, (b) plot of the spatio-temporal evolution of $f(\phi^s)$ where the final time corresponds to a value of 120 days.
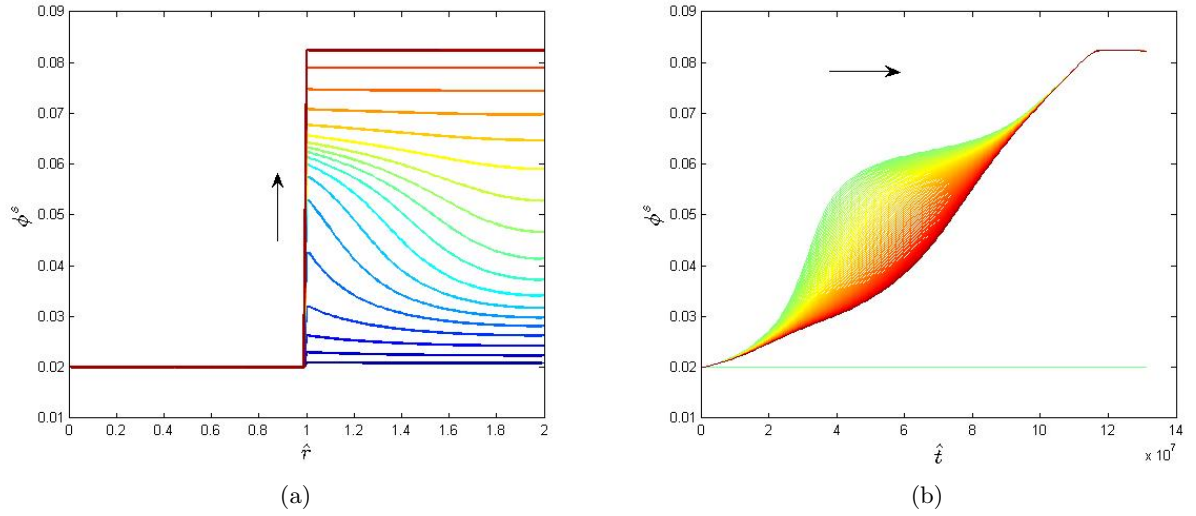
Figure 5.3: Simulations of the mixture solid volume fraction ϕ^s in the baseline case: (a) plot of spatial profiles of ϕ^s at time intervals of six days. Note that the cell boundary is located at $\hat{r} = 1$ and the outer boundary of the scaffold is located at $\hat{r} = 2$, (b) plot of temporal evolution of ϕ^s where the final time corresponds to a value of 120 days.
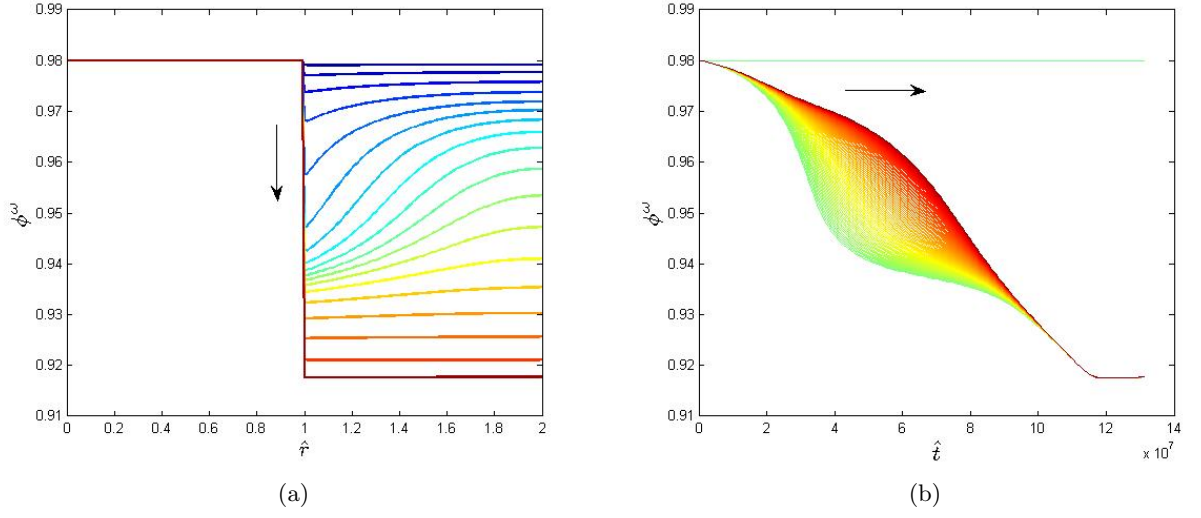
Figure 5.4: Simulations of the mixture porosity ϕ^w in the baseline case: (a) plot of spatial profiles of ϕ^w at time intervals of six days. Note that the cell boundary is located at $\hat{r} = 1$ and the outer boundary of the scaffold is located at $\hat{r} = 2$, (b) plot of temporal evolution of ϕ^w where the final time corresponds to a value of 120 days.
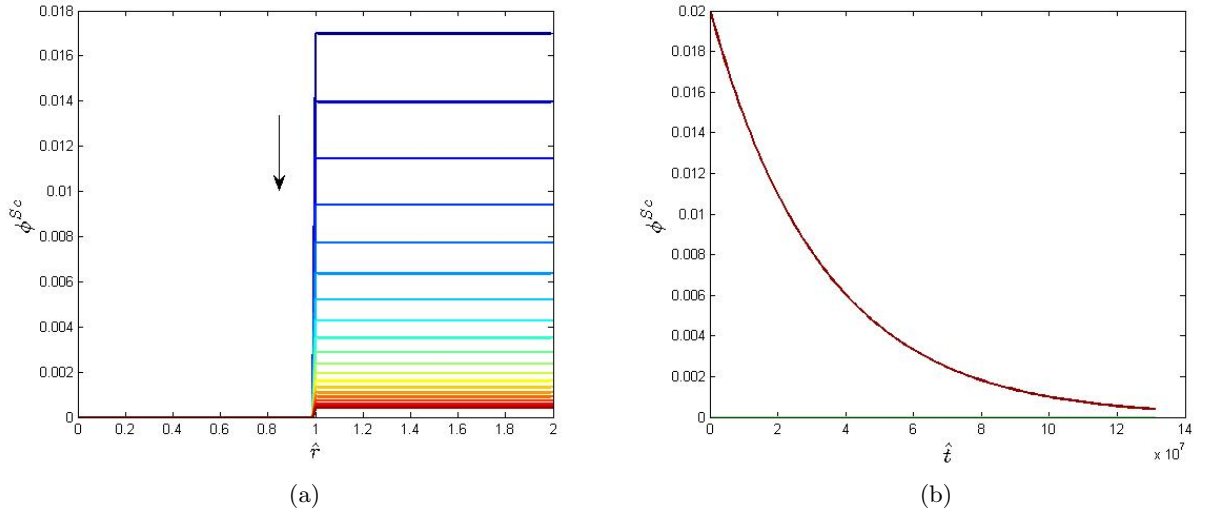
Figure 5.5: Simulations of the scaffold volume fraction ϕ^{Sc} in the baseline case: (a) plot of spatial profiles of ϕ^{Sc} at time intervals of six days. Note that the cell boundary is located at $\hat{r} = 1$ and the outer boundary of the scaffold is located at $\hat{r} = 2$, (b) plot of temporal evolution of ϕ^{Sc} where the final time corresponds to a value of 120 days.
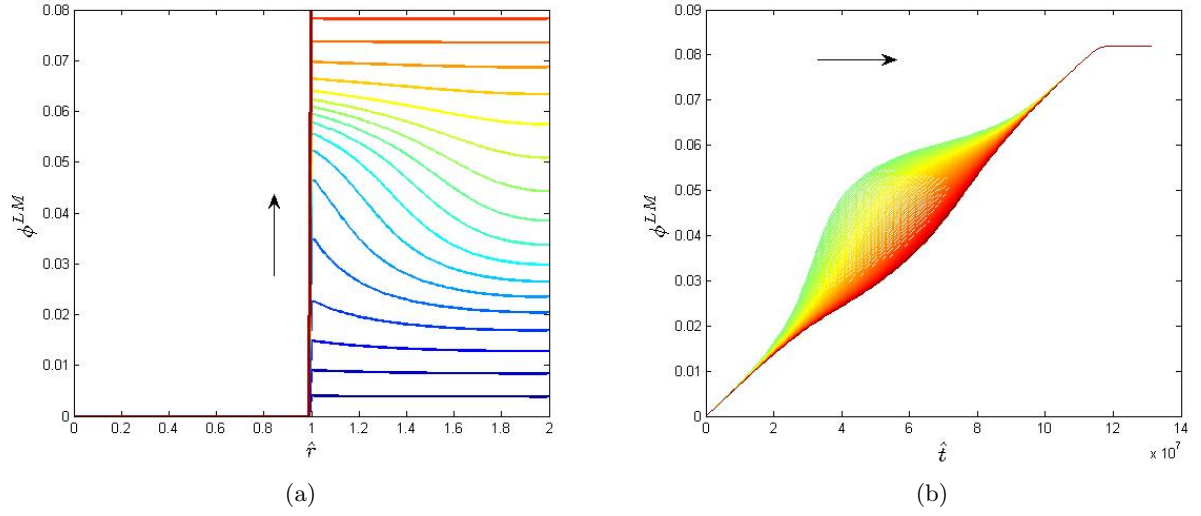
Figure 5.6: Simulations of the linked matrix volume fraction ϕ^{LM} in the baseline case: (a) plot of spatial profiles of ϕ^{LM} at time intervals of six days. Note that the cell boundary is located at $\hat{r} = 1$ and the outer boundary of the scaffold is located at $\hat{r} = 2$, (b) plot of temporal evolution of ϕ^{LM} where the final time corresponds to a value of 120 days.
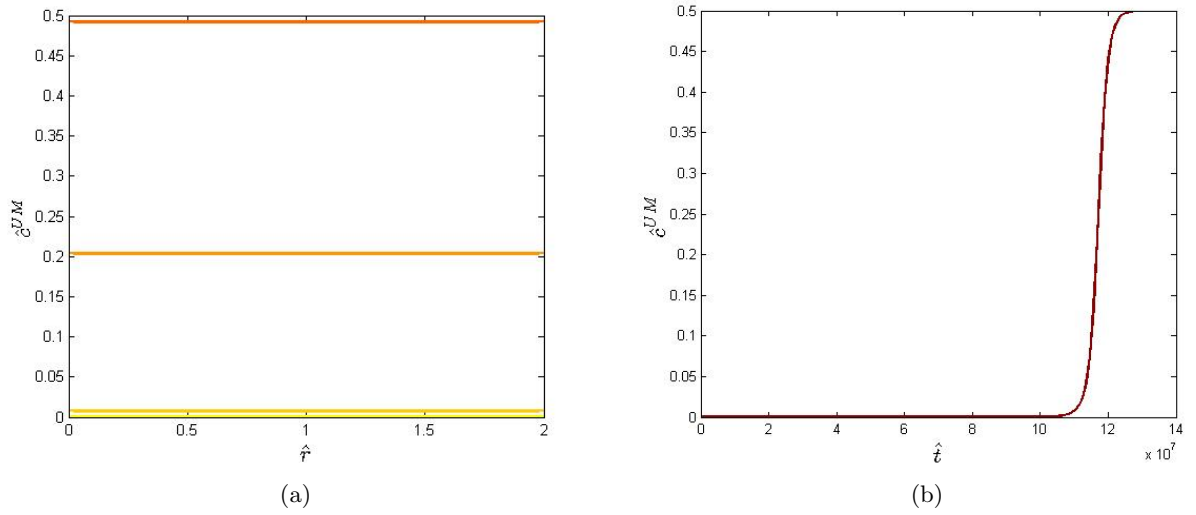
Figure 5.7: Simulations of the unlinked matrix concentration $\hat{c}^{UM}$ in the baseline case: (a) plot of spatial profiles of $\hat{c}^{UM}$ at time intervals of six days. Note that the cell boundary is located at $\hat{r} = 1$ and the outer boundary of the scaffold is located at $\hat{r} = 2$, (b) plot of temporal evolution of $\hat{c}^{UM}$ where the final time corresponds to a value of 120 days.
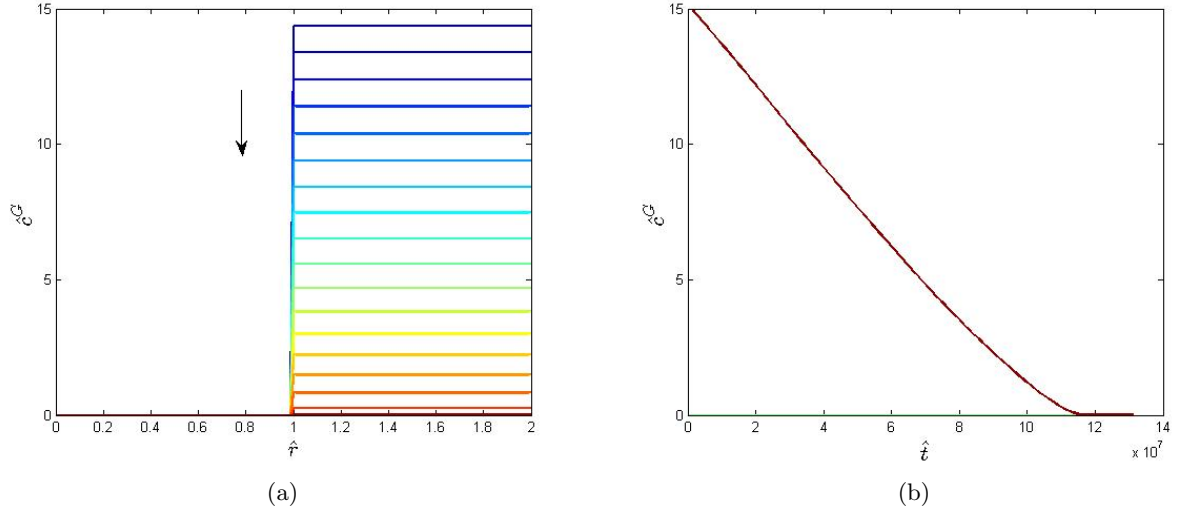
Figure 5.8: Simulations of the growth factor concentration $\hat{c}^G$ in the baseline case: (a) plot of spatial profiles of $\hat{c}^G$ at time intervals of six days. Note that the cell boundary is located at $\hat{r} = 1$ and the outer boundary of the scaffold is located at $\hat{r} = 2$, (b) plot of temporal evolution of $\hat{c}^G$ where the final time corresponds to a value of 120 days.

These profiles exhibit very little spatial dependence, as might be expected due to the simple decay model used for scaffold degradation (3.91). For the linked ECM volume fraction, spatial and temporal profiles (Figure 5.6a-b) are similar to those for the solid phase volume fraction ϕ^s (Figure 5.3). Differences between ϕ^s and ϕ^{LM} are more pronounced at earlier times, prior to the degradation of the scaffold from the engineered cartilage system.

Lastly, spatial and temporal profiles in the baseline case are shown for the unlinked ECM ($\hat{c}^{UM}$) concentration (Figure 5.7) and the growth factor concentration ($\hat{c}^G$) (Figure 5.8). Both sets of profiles are observed to exhibit very little spatial dependence, resulting from the fact that diffusive times scales for unlinked matrix and growth factor in the model are relatively fast compared to time scales for ECM synthesis, linking and scaffold degradation. Figure 5.7 demonstrates that, for a majority of the simulation, unlinked ECM is being consumed to form linked ECM faster than it can be produced by the cell. At much later times, when the Gaussian linking has fully propagated through most of the spatial region, the cell-mediated biosynthesis of unlinked ECM eventually dominates the linking rate. This results in increasing values of c^{UM} that approach the steady-state value based on the product inhibition assumption.

Overall, the baseline case indicates that variables modeling unbound solutes dissolved in the interstitial fluid, i.e. $\hat{c}^{UM}, \hat{c}^G$, as well as the scaffold volume fraction ϕ^{Sc} exhibit predominantly temporal responses. The remaining independent variables, ϕ^s and ϕ^{LM} exhibit more complex

dependencies over both the spatial and temporal domains considered for the baseline case.

5.5   Perturbations of the Baseline Case

In this section, some perturbations of the baseline case are considered to demonstrate sensitivity of the spatio-temporal model to a few key parameters that affect engineered tissue properties and outcomes. Specifically, one parameter relating to design of the initial scaffold is considered along with two parameters that govern physiological interactions in the engineered cartilage system.

5.5.1   Scaffold Porosity

As ECM regeneration proceeds in the engineered tissue construct, the porosity of the bound solid phase ϕ^s provides an outcome measure that is expected to have a strong positive correlation with elastic stiffness of the construct. In 2009, Erickson et al. [11] cultured mesenchymal stem cells (MSCs) in hyaluronic acid scaffolds with varying initial scaffold volume fractions of $1\%, 2\%$ and 5%. Engineered constructs cultured to 6 weeks exhibited higher measures of the elastic Young's modulus in macroscopic mechanical testing for the scaffolds with lower initial scaffold polymer volume fractions. Histological imaging of the samples revealed increasing spatial localization of cell synthesized proteoglycans near the cells as the initial hydrogel volume fraction was increased (Figure 5.9). These findings suggest that transport and cross-linking of a key cell-synthesized ECM constituent may be adversely affected by initial scaffold porosity values above a critical threshold.

Based on these experimental findings, our model enables examination of a hypothesis that the increasing porosity in an engineered system may adversely affect the accumulation of linked ECM volume at later times. To evaluate this hypothesis, perturbations of the baseline case were considered in which the initial scaffold solid volume fraction was varied between the three values $\phi_0^{Sc} = 0.01$, $\phi_0^{Sc} = 0.02$, and $\phi_0^{Sc} = 0.05$. Spatial profiles of the linked ECM volume fraction ϕ^{LM} are shown at time points of 3 days (first row), 7 days (second row) and 14 days (third row), where the columns represent initial scaffold volume fractions of 1%, 2% and 5% (Figure 5.10). We observe spatial profiles (Figure 5.10) that resemble those in the experiment, particularly in the case $\phi_0^{Sc} = 0.05$ (right-most column) where linked ECM is highly localized in space near the periphery of the cell, whereas it is more evenly spread out when the scaffold is designed to be less dense and more porous. Since diffusive transport occurs on relatively fast scales in our model, these simulations indicate that convective transport and the effects of porosity on transformation of unlinked ECM into linked ECM in our model may explain lower values of macroscopic elastic stiffness of the construct for scaffold designs that are not porous enough.
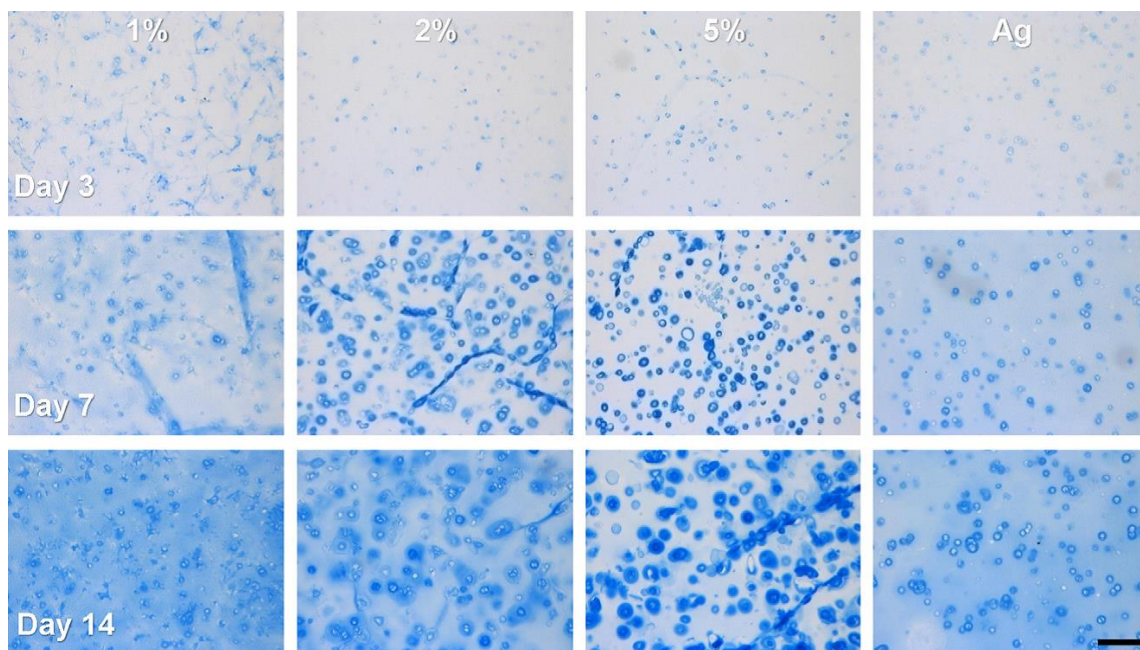
Figure 5.9: Histological (Alcian blue) staining of cell-synthesized proteoglycans (PGs) in MeHA hydrogels seeded with mesenchymal stem cells (MSCs). The columns correspond to initial scaffold volume fractions of 1%, 2%, and 5% and an agarose scaffold (control) after 3 days (top), 7 days (middle), and 14 days (bottom) in chondrogenic culture media. Pericellular accumulation of PGs is evident in MeHA constructs with higher initial scaffold density while a more even spatial distribution of PGs is observed in constructs originating from 1% MeHA scaffolds. (Reprinted from Osteoarthritis and Cartilage, 17/12, I.E. Erickson, A.H. Huang, S. Sengupta, S. Kestle, J.A. Burdick, R.L. Mauck, Macromer density influences mesenchymal stem cell chondrogenesis and maturation in photocrosslinked hyaluronic acid hydrogels, 1639-1648, Copyright (2009), with permission from Elsevier).
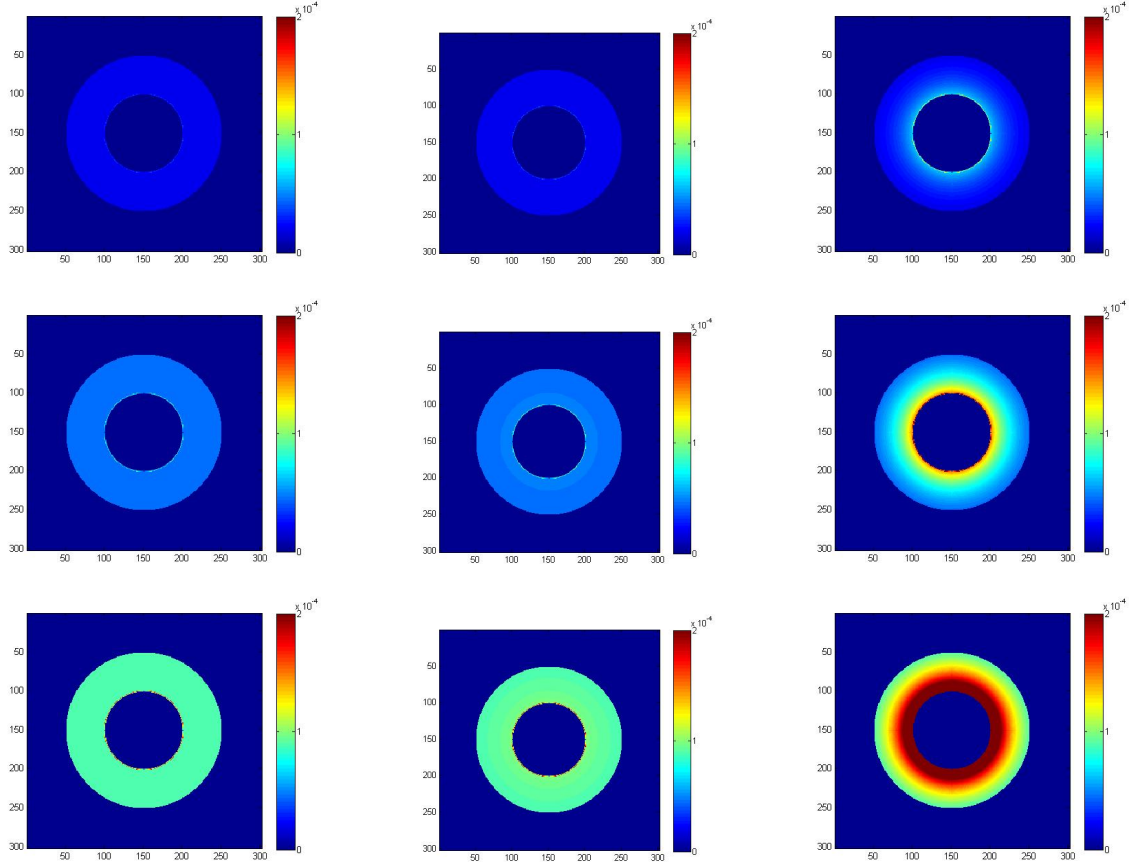
Figure 5.10: Simulations of perturbations to the baseline case for the spatio-temporal cartilage regeneration model to simulate the effects of scaffold porosity on the spatial distribution of linked ECM ϕ^{LM} shown around a single cell. The columns correspond to initial scaffold solid volume fractions ϕ_0^{Sc} of 1% (left column), 2% (middle column), and 5% (right column). Spatial profiles are shown after 3 days (top row), 7 days (middle row), and 14 days (bottom row).

5.5.2 Interaction Mechanisms

As discussed in Section 5.2.3, physiological parameters in our model regulate interactions between the cells and their local environment in our models of cartilage ECM regeneration. This category of parameters is expected to vary from one cell-scaffold system to another and, ultimately, could be used with experimental data to quantitatively characterize differences between engineered biomaterial systems of various types. Perturbations to two physiological parameters were considered to illustrate sensitivity of the model to these interaction mechanisms. The first was the critical porosity ϕ_*^s in the Gaussian models for ECM linking that delineates regimes of increasing versus decreasing linking rate as a function of porosity. The second was the critical unlinked ECM concentration $\hat{c}_*^{UM}$ for regulation of cell-mediated biosynthesis based on the product inhibition hypothesis.

The value of the critical porosity parameter in the baseline case $\phi_*^s = 0.045$ was perturbed to consider the two additional values $\phi_*^s = 0.035$ and $\phi_*^s = 0.055$, and results are shown in Figure 5.11. Increasing ϕ_*^s to 0.055 (Fig. 5.11) significantly delayed achievement of the peak ECM linking rate (Fig. 5.11l), past the time of complete scaffold degradation and until a sufficient amount of linked ECM accumulated in the system. This resulted in a decrease in the steady-state value of the linked ECM volume fraction in the case $\phi_*^s = 0.055$, relative to the baseline case ($\phi_*^s = 0.045$) (Fig.5.11b vs Fig.5.11c). The steady-state values of ϕ^{LM} are also affected by the duration of time during which larger values of growth factor concentration $\hat{c}^G$ (Fig. 5.11d-f) are present in combination with active ECM linking (Fig. 5.11j-l). As a result, the lower steady-state value of ϕ^{LM} in the case $\phi_*^s = 0.055$ is also caused by the delayed ECM linking which occurs in a time frame where the growth factor concentration has decreased significantly.

The critical unlinked ECM concentration $\hat{c}_*^{UM}$ was also perturbed from its baseline value of $\hat{c}_*^{UM} = 0.5$ and the two additional cases $\hat{c}_*^{UM} = 0.4$ and $\hat{c}_*^{UM} = 0.6$ were considered. Results for the linked matrix volume fraction ϕ^{LM}, for $\hat{c}^{UM}$ and for the linking rate $f(\phi^s)$ are shown in Figure 5.12. It is observed that the steady-state value of ϕ^{LM} increases as the value of $\hat{c}_*^{UM}$ is increased from 0.4 to 0.6 (Figure 5.12a,b,c). Recall that the product inhibition hypothesis results in a linearly decreasing cell-mediated rate of unlinked ECM biosynthesis as the concentration $\hat{c}^{UM}$ increases. As a result, lower values of $\hat{c}_*^{UM}$ lead to a longer period of linking due to slower cell-mediated biosynthesis of unlinked ECM (Figure 5.12g,h,i). While linking occurs over a longer duration (Figure 5.12g,h,i), the lack of adequate supply of cell-synthesized unlinked ECM can adversely affect the total amount of linked ECM that accumulates over long time periods. Hence, we observe larger steady-state values of ϕ^s at higher values of $\hat{c}_*^{UM}$ due to both the larger biosynthesis rate, relative to the linking rate, at earlier times as well as interactions with larger concentrations of the (limited supply of) growth factors present in the system, as
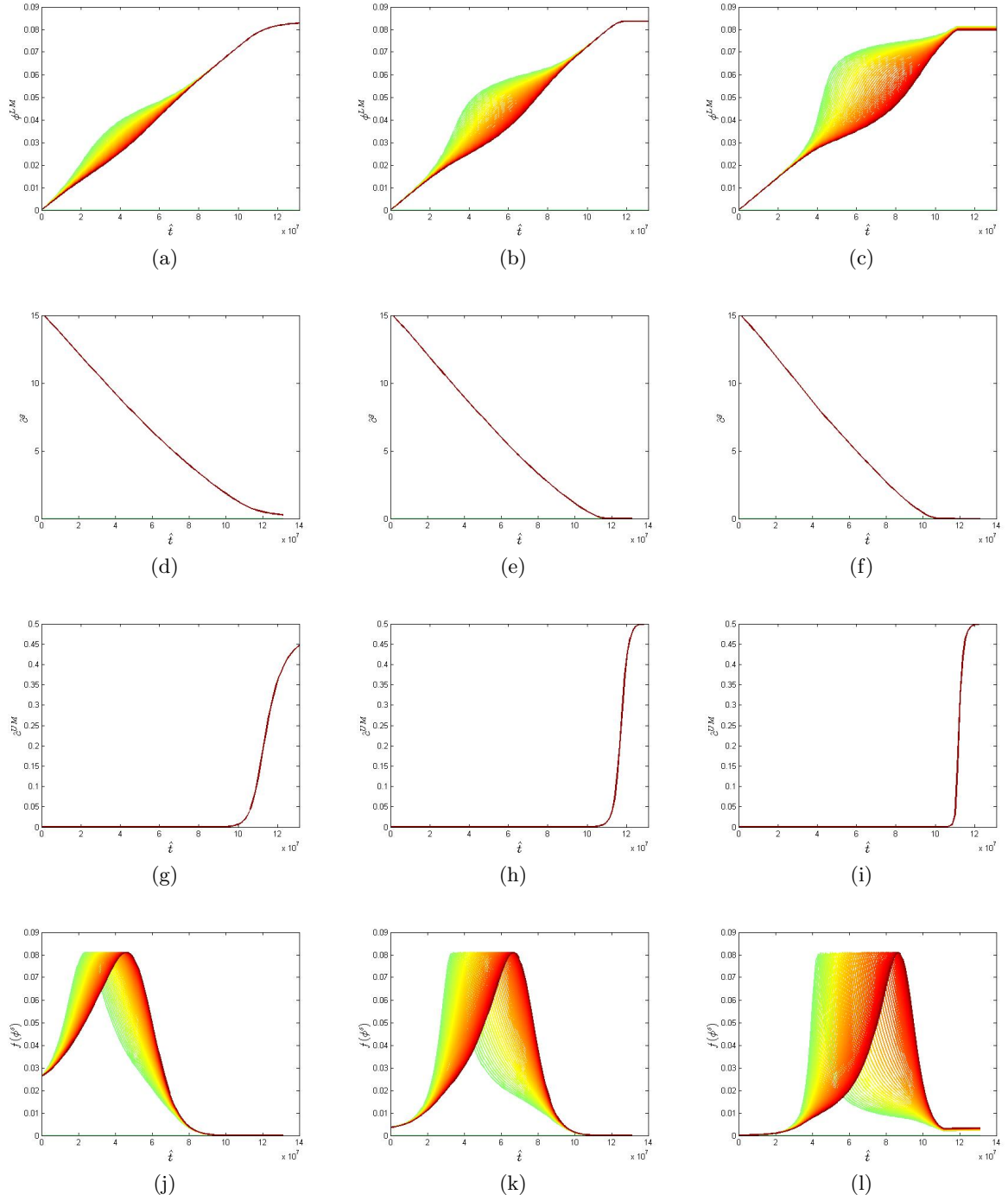
Figure 5.11: Effects of perturbing the critical porosity parameter ϕ_*^s on key variables: the cases shown are $\phi_*^s = 0.035$ (left column), the baseline case $\phi_*^s = 0.045$ (middle column), and $\phi_*^s = 0.055$ (right column). Results are shown for the dependent variables: linked ECM volume fraction ϕ^{LM} (first row), growth factor concentration c^G (second row), unlinked ECM concentration c^{UM} (third row), and ECM linking rate $f(\phi^s)$ (fourth row).

was the case in Figure 5.11.

5.6 Identifying a Reduced Model

All simulations shown in the previous section had some common aspects suggesting that a reduced version of the two-zone spatio-temporal PDE model can be identified. Specifically, all simulations had values of $|\hat{u}^s|$, $|\hat{\dot{u}}^s|$ and $|\hat{p}|$ that were less than 10^{-10}. Hence, we can formulate a reduced model by assuming that $\hat{u}^s \approx 0$, $\hat{p} \approx 0$, and $\hat{\dot{u}}^s \approx 0$. In the cell region, these assumptions imply that ϕ^ω is constant with respect to both $\hat{r}$ and $\hat{t}$, while $\hat{c}^{UM}$ depends only on $\hat{t}$. We now apply these assumptions to the non-dimensional model (Section 3.5), noting that the osmotic parameter ϕ is taken to be 1.

In the cell region, equations (3.84)-(3.86) will be satisfied exactly and equation (3.87) reduces to

$$\frac{d\hat{c}^{UM}}{d\hat{t}} = \hat{k}_{UM} N^* (\hat{c}_*^{UM} - \hat{c}^{UM}), \tag{5.1}$$

where the solution of the above equation with respect to the initial condition $\hat{c}^{UM}(0, \hat{r}) = 0$ is

$$\hat{c}^{UM} = \hat{c}_*^{UM} \left(1 - e^{-N^* k_{UM} \hat{t}}\right). \tag{5.2}$$

Hence, the cell region can be eliminated from the model and replaced by a time-varying boundary condition for $\hat{c}^{UM}$ based on the last formula.

In the extracellular region, the first equation (3.88) will be satisfied automatically but the second equation (3.89) will be reduced to

$$-\hat{k}_{Sc} \phi^{Sc} + \hat{k}_1 (\phi^\omega)^2 \hat{c}^G \hat{c}^{UM} = 0. \tag{5.3}$$

For the baseline case considered in this chapter, we evaluated the left hand side in the equation above and found that its value was less than 10^{-9}. Equations (3.90) and (3.91) reduce to

$$\frac{\partial \phi^{LM}}{\partial \hat{t}} = \hat{k}_1 (\phi^\omega)^2 \hat{c}^G \hat{c}^{UM}, \tag{5.4}$$

which is a PDE since $\hat{k}_1 = f(\hat{t}, \hat{r})$, and

$$\frac{d\phi^{Sc}}{d\hat{t}} = -\hat{k}_{Sc} \phi^{Sc}, \tag{5.5}$$

which is an ODE. Based on the initial condition $\phi^{Sc} = \phi_0^{Sc}$ this ODE has solution

$$\phi^{Sc} = \phi_0^{Sc} e^{-k_{Sc} \hat{t}}. \tag{5.6}$$
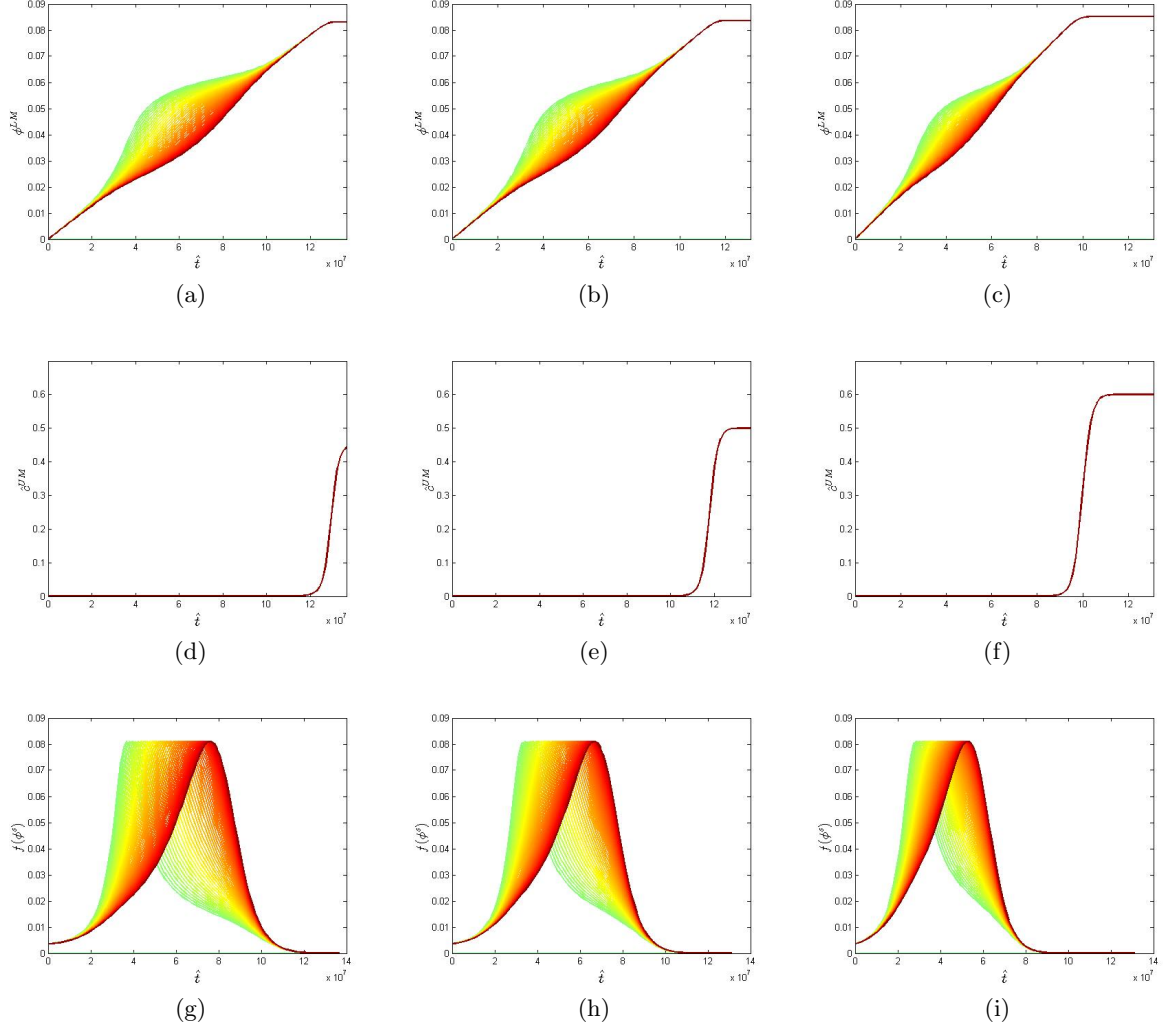
Figure 5.12: Effects of perturbing the critical unlinked ECM concentration $\hat{c}_*^{UM}$ on key variables: the cases shown are $\hat{c}_*^{UM} = 0.4$ (left column), the baseline case $\hat{c}_*^{UM} = 0.5$ (middle column) and $\hat{c}_*^{UM} = 0.6$ (right column). Results are shown for the dependent variables: linked ECM volume fraction ϕ^{LM} (top row), unlinked ECM concentration c^{UM} (middle row), and ECM linking rate $f(\phi^s)$ (bottom row).

The remaining two equations (3.92) and (3.93) are reduced to

$$\partial_{\hat{t}}(\phi^\omega \hat{c}^{UM}) + \left(\frac{\partial}{\partial \hat{r}} + \frac{2}{\hat{r}}\right)\left[(-D_r^{UM}\phi^\omega)\frac{\partial \hat{c}^{UM}}{\partial \hat{r}}\right] = -\hat{k}_2(\phi^\omega)^2 \hat{c}^G \hat{c}^{UM}, \tag{5.7}$$

and

$$\partial_{\hat{t}}(\phi^\omega \hat{c}^G) + \left(\frac{\partial}{\partial \hat{r}} + \frac{2}{\hat{r}}\right)\left[(-D_r^G\phi^\omega)\frac{\partial \hat{c}^G}{\partial \hat{r}}\right] = -\hat{k}_3(\phi^\omega)^2 \hat{c}^G \hat{c}^{UM}. \tag{5.8}$$

Based on these simplifications, the identified reduced model is summarized as $(1 < \hat{r} < \hat{b}, \hat{t} > 0)$:

$$\frac{\partial \phi^{LM}}{\partial \hat{t}} = \hat{k}_1(\phi^\omega)^2 \hat{c}^G \hat{c}^{UM} \tag{5.9}$$

$$\frac{d\phi^{Sc}}{d\hat{t}} = -\hat{k}_{Sc}\phi^{Sc} \tag{5.10}$$

$$\partial_{\hat{t}}(\phi^\omega \hat{c}^{UM}) + \left(\frac{\partial}{\partial \hat{r}} + \frac{2}{\hat{r}}\right)\left[(-D_r^{UM}\phi^\omega)\frac{\partial \hat{c}^{UM}}{\partial \hat{r}}\right] = -\hat{k}_2(\phi^\omega)^2 \hat{c}^G \hat{c}^{UM}, \tag{5.11}$$

$$\partial_{\hat{t}}(\phi^\omega \hat{c}^G) + \left(\frac{\partial}{\partial \hat{r}} + \frac{2}{\hat{r}}\right)\left[(-D_r^G\phi^\omega)\frac{\partial \hat{c}^G}{\partial \hat{r}}\right] = -\hat{k}_3(\phi^\omega)^2 \hat{c}^G \hat{c}^{UM}, \tag{5.12}$$

where the initial conditions are

$$\phi^{LM}(0,\hat{r}) = 0, \quad \phi^{Sc}(0,\hat{r}) = \phi_0^{Sc}, \quad \hat{c}^{UM}(0,\hat{r}) = 0, \quad \hat{c}^G(0,\hat{r}) = c_0^G, \tag{5.13}$$

the boundary conditions at $\hat{r} = 1$ are

$$\frac{\partial \phi^{LM}}{\partial \hat{r}}(\hat{t},1) = 0, \quad \frac{\partial \phi^{Sc}}{\partial \hat{r}}(\hat{t},1) = 0, \quad \hat{c}^{UM}(\hat{t},1) = \hat{c}_*^{UM}\left(1 - e^{-N^* k_{UM}\hat{t}}\right), \quad \frac{\partial \hat{c}^G}{\partial \hat{r}}(\hat{t},1) = 0, \tag{5.14}$$

and the boundary conditions at $\hat{r} = \hat{b}$ are

$$\frac{\partial \phi^{LM}}{\partial \hat{r}}(\hat{t},\hat{b}) = 0, \quad \frac{\partial \phi^{Sc}}{\partial \hat{r}}(\hat{t},\hat{b}) = 0, \quad \frac{\partial \hat{c}^{UM}}{\partial \hat{r}}(\hat{t},\hat{b}) = 0, \quad \frac{\partial \hat{c}^G}{\partial \hat{r}}(\hat{t},\hat{b}) = 0, \tag{5.15}$$

where $\hat{b}$ is the outer boundary of the region.

5.7 Conclusions and Future Directions

Multiphasic continuum mixture models are widely used to describe both biomechanical deformation and transport of water and solutes in articular cartilage [42]. Cartilage is an avascular and aneural biological soft tissue, resulting in a limited capacity for growth and repair, and a high incidence of osteoarthritis with aging [38]. The cartilage extracellular matrix (ECM) is

maintained by a single population of sparsely distributed cells called chondrcytes that regulate their metabolic activity in response to biophysical and biomechanical cues in their local environment. When chondrocytes are seeded into a biomaterial scaffold, these cells recapitulate many of the metabolic events involved in the process of development, providing an excellent in vitro system for studying tissue regeneration. While trial-and-error approaches for developing engineered tissues have led to many early advances, the complexity of the cartilage regeneration process requires a more rational, design-based approach to develop functional cartilage replacements in an optimal manner. Achieving this goal requires the formulation and solution of a continuum mixture model to describe interactions among the biophysical, biomechanical and physiological mechanisms at the cellular scale.

In this dissertation, the ODE mixture model developed in [19] was extended to the spatio-temporal (PDE) case by using the modeling framework of multiphasic continuum mixture theory. This approach allowed for the development of a mathematical model capturing interactions among biophysical, biochemical, biomechanical and physiological phenomena during cartilage ECM regeneration in an evolving tissue engineered construct arising from an initial cell-seeded scaffold. The general formulation, developed in Chapter 2, was based on delineating primary variables into those that are bound to the solid phase of the mixture and those that are unbound in that they are dissolved in the interstitial fluid. In Chapter 3, this formulation was specialized to a one-dimensional spherical model of a single chondrocyte in an extracellular region that is initially scaffold but, over time, evolves into an engineered tissue construct. The primary variables included in this formulation were the solid displacement, fluid velocity, pore pressure, solid volume fractions of scaffold and linked ECM, and concentrations of the (unbound) solutes that are the unlinked matrix and growth factor. This model assumed that unlinked ECM is synthesized within the cell and is transported in the system by both convection and diffusion. Growth factor was assumed to be present in only the extracellular region and was required in modeling the interaction mechanism that transforms unlinked (unbound) ECM into linked (bound) ECM, causing the solid phase volume fraction within the mixture to increase. Linking rates were modeled as depending, in a nonlinear fashion, on the evolving porosity of the mixture. A Gaussian model was used to represent the phenomena of poor linking when the initial scaffold is very dilute or when the pore size within the construct reduces to the point of inhibiting spatial distribution of unlinked ECM and formation of linked ECM. This model was solved, numerically, using a finite difference method that was implemented in MATLAB. The implementation was verified for accuracy by developing an analytical series solution for a reaction-diffusion model arising as a special case of the general model (Chapter 4). The numerical solution was applied to simulate cartilage ECM regeneration in the local environment of a single cell based on delineating model parameters into categories of biophysical, scaffold design and physiological parameters. Values of the biophysical and scaffold parameters were

fixed based on the literature and physiological parameter values were calibrated to formulate a baseline case that modeled regeneration of cartilage ECM on realistic time scales. Perturbation of the baseline case via a parametric analysis demonstrated the sensitivity of tissue outcomes to both the choice of scaffold porosity and to physiological parameters that are expected to vary from one cell-biomaterial system to another. Based on the full set of simulations considered, a reduced model in which the cell region was eliminated and replaced by a time-dependent boundary condition was also identified.

The model developed in this dissertation provides a detailed quantitative framework that captures several key biophysical, physiological, and biomechanical mechanisms that interact within an engineered cartilage system. Trial-and-error approaches to achieving desired or optimal functional outcomes in an engineered cartilage construct can be both time-consuming and costly. The integration of mathematical models into the experimental design process has the potential to accelerate progress along the path to realization of optimal cartilage tissue engineering. For example models calibrated, via parameter estimation, on an initial system design or a data set of smaller size could then be used in simulations that could suggest an improved design to manufacture and test in the lab. Use of a mixture modeling approach can facilitate this process, since natural distinctions between various experimental measures such as dry mass versus wet mass, density versus volume fraction, and diffusivities in free solution versus a mixture are built into the modeling framework.

While the mixture model developed in this dissertation is a spatio-temporal extension of the previously published ODE mixture model [19], it was limited to one spatial dimension based on idealizing the cell and its surrounding ECM as having spherical geometry. Extensions to higher dimensions are needed to more accurately represent realistic cell geometries for engineered cartilage cell-scaffold systems. Such extensions would naturally require a reformulation of the numerical methods in terms of finite elements which more naturally conform to cell shapes in two and three-dimensions. The model also assumed fixed values for the elastic material properties in the extracellular region, even though the properties of the solid phase are changing significantly with time. This assumption was reasonable for the modeling applications considered in this work as they were focused on biosynthesis and transport. Consequently, throughout all simulations, solid displacements and the pore pressure were negligibly small, resulting in automatic satisfaction of the mixture momentum equation which is the equation involving the elastic material parameters. Use of the modeling framework to simulate biomechanical deformation, e.g. via the application of external loading, will require an extension to include a model for the evolution of the elastic Young's modulus and Poisson's ratio with accumulating linked ECM density. To date, the nature of such relations is not well understood. It should also be noted that the model is highly sensitive to the Gaussian form that was chosen to represent the relation between ECM linking rate and porosity of the mixture. Ideally, as more data from

experiments that image accumulating ECM content in engineered cartilage become available, the mathematical form of this term would need to be assessed for its validity and refined as needed.

The model developed in this work focuses on cell-matrix interactions at the scale of individual cells. Relating biophysical, biochemical, biomechanical and physiological phenomena that occur at this microscopic scale with related phenomena at the macroscopic scale of a tissue layer requires approaches to bridging models at these two diverse scales. Models at the scale of individual cells can serve as useful tools for identifying relationships between primary variables that can be averaged and upscaled to formulate constitutive laws for cellular effects in models at the macroscopic tissue scale. Viability of this approach was demonstrated for a reaction-diffusion model of diffusive nutrient transport and uptake in a cell-seeded scaffold in [2] where a numerical homogenization approach was used to bridge scales. In future studies this multiscale modeling approach could be extended to models formulated within the mixture framework, including the one developed in this dissertation, to develop more detailed, realistic models for cell-matrix interactions in tissue engineered articular cartilage at the macroscopic scale.

BIBLIOGRAPHY

[1] T.A.E. Ahmed and M.T. Hincke. Strategies for articular cartilage lesion repair and functional restoration. Tissue Engineering Part B, 16(3):305–329, 2010.

[2] A.C. Aristotelous and M.A. Haider. Use of hybrid discrete cellular models for identification of macroscopic nutrient loss in reactiondiffusion models of tissues. International Journal for Numerical Methods in Biomedical Engineering, 30(8):767–780, 2014.

[3] G.A. Ateshian, K.D. Costa, E.U. Azeloglu, B. Morrison, and C.T. Hung. Continuum modeling of biological tissue growth by cell division, and alteration of intracellular osmolytes and extracellular fixed charge density. Journal of Biomechanical Engineering, Transactions of the ASME, 131(10):101001, 2009.

[4] A.L. Bauer, T.L. Jackson, and Y. Jiang. A cell-based model exhibiting branching and anastomosis during tumor induced angiogenesis. Biophysical Journal, 92(9):3105–3121, 2007.

[5] F. Berthiaume, T.J. Maguire, and M.L. Yarmush. Tissue engineering and regenerative medicine: history, progress, and challenges. Annual Review of Chemical and Biomolecular Engineering, 2(1):403–30, 2011.

[6] C.J.W. Breward, H.M. Byrne, and C.E. Lewis. A multiphase model describing vascular tumour growth. Bulletin of Mathematical Biology, 65(4):609–640, 2003.

[7] J.A. Buckwalter and N.E. Lane. Athletics and osteoarthritis. The American Journal of Sports Medicine, 25(6):873–881, 1997.

[8] M.D. Buschmann, Y.A. Gluzband, A.J. Grodzinsky, J.H. Kimura, and E.B. Hunziker. Chondrocytes in agarose culture synthesize a mechanically functional extracellular matrix. Journal of Orthopaedic Research, 10:745–758, 1992.

[9] C.A. Chung, C.W. Yang, and C.W. Chen. Analysis of cell growth and diffusion in a scaffold for cartilage tissue engineering. Biotechnology and Bioengineering, 94(6):1138–1146, 2005.

[10] M.A. Dimicco and R.L. Sah. Dependence of cartilage matrix composition on biosynthesis, diffusion, and reaction. Transport In Porous Media, 50(1):57–73, 2003.

[11] I.E. Erickson, A.H. Huang, S. Sengupta, S. Kestle, J.A. Burdick, and R.L. Mauck. Macromer density influences mesenchymal stem cell chondrogenesis and maturation in photocrosslinked hyaluronic acid hydrogels. Osteoarthritis and Cartilage, 17(12):1639–1648, 2009.

[12] H. Fernandes, L. Moroni, V.C. Blitterswijk, and D.J. de Boer. Extracellular matrix and tissue engineering applications. Journal Of Materials Chemistry, 19(31):5474–5484, 2009.

[13] L.E. Freed, G. Vunjak-Novakovic, J.C. Marquis, and R. Langer. Kinetics of chondrocyte growth in cell-polymer implants. Biotechnology and Bioengineering, 43(7):597–604, 1994.

[14] A.M. Freyria and F. Mallein-Gerin. Chondrocytes or adult stem cells for cartilage repair: the indisputable role of growth factors. Injury, 43(3):259–265, 2012.

[15] P. Giannoni and R. Narcisi. Nano-approaches in cartilage repair. Journal of Applied Biomaterials and Biomechanics, 7(1):1–12, 2009.

[16] M.B. Goldring and S.R. Goldring. Osteoarthritis. Journal of Cellular Physiology, 213(3):626–634, 2007.

[17] W.Y. Gu, H. Yao, A.L. Vega, and D. Flagler. Diffusivity of ions in agarose gels and intervertebral disc: effect of porosity. Annals of Biomedical Engineering, 32(12):1710–1717, 2004.

[18] F. Guilak, B.T. Estes, B.O. Diekman, F.T. Moutous, and J.M. Gimble. Multipotent adult stem cells from adipose tissue for musculoskeletal tissue engineering. Clinical Orthopaedics and Related Research, 468(9):2530–2540, 2010.

[19] M.A. Haider, J.E. Olander, R.F. Arnold, D.R. Marous, A.J. McLamb, K.C. Thompson, W.R. Woodruff, and J.M. Haugh. A phenomenological mixture model for biosynthesis and linking of cartilage extracellular matrix in scaffolds seeded with chondrocytes. Biomechanics and Modeling in Mechanobiology, 10:915–924, 2011.

[20] L. Han, A.J. Grodzinsky, and C. Ortiz. Nanomechanics of the Cartilage Extracellular Matrix. Annual Review of Materials Research, 41:133–168, 2011.

[21] R. Hardmeier, H. Redl, and S. Marlovits. Effects of mechanical loading on collagen propeptides processing in cartilage repair. Journal of Tissue Engineering and Regenerative Medicine, 4(1):1–11, 2010.

[22] J. Haugh. Mathematical modeling of cartilage regeneration in cell-seeded scaffold. NCSU, 2010.

[23] A.H. Huang, M.G. Farrell, and R.L. Mauck. Mechanics and mechanobiology of mesenchymal stem-cell based engineered cartilage. Journal of Biomechanics, 43(1):128–136, 2010.

[24] M. Keeney, J.H. Lai, and F. Yang. Recent progress in cartilage tissue engineering. Current Opinion in Biotechnology, 22(5):734–740, 2011.

[25] I.L. Kim, R.L. Mauck, and J.A. Burdick. Hydrogel design for cartilage tissue engineering: A case study with hyaluronic acid. Journal of Biomechanics, 32(34):8771–8782, 2011.

[26] L. Kock, C.C. Van Donkelaar, and K. Ito. Tissue engineering of functional articular cartilage: the current status. Cell and Tissue Research, 347(3):613–627, 2012.

[27] J.D. Kretlow and A.G. Mikos. From material to tissue: biomaterial development, scaffold fabrication, and tissue engineering. AiChE Journal, 54(12):3048–3067, 2008.

[28] W. M. Lai, D. D. Sun, G. A. Ateshian, X. E. Guo, and V. C. Mow. Electrical signals for chondrocytes in cartilage. Biorheology, 39:39–45, 2002.

[29] G. Lemon, J.R. King, H. Byrne, O.E. Jensen, and K.M. Shakesheff. Mathematical modelling of engineered tissue growth using a multiphase porous flow mixture theory. Journal of Mathematical Biology, 52(5).

[30] C.J. Little, N.K. Bawolin, and X. Chen. Mechanical properties of natural cartilage and tissue engineered constructs. Tissue Engineering: Part B, 17(4):213–227, 2011.

[31] S.R. Lubkin and T. Jackson. Multiphase Mechanics of Capsule Formation in Tumors. Journal of Biomechanical Engineering, 124(2):237–243, 2002.

[32] S.R. Lubkin, S. Schnell, P.K. Maini, and S.A. Newman. Branched organs: Mechanics of morphogenesis by multiple mechanisms. Current Topics in Developmental Biology, 81:249–268, 2007.

[33] P. Macklin, S. McDougall, A.R.A. Anderson, M.A. Chaplain, V. Cristini, and J. Lowengrub. Multiscale modeling and nonlinear simulation of vascular tumor growth. Journal of Mathematical Biology, 58(4):765–798, 2009.

[34] A.F. Mak. The apparent viscoelastic behavior of articular cartilage - the contributions from the intrinsic matrix viscoelasticity and interstitial fluid flows. Journal of Biomechanical Engineering, 108(2):123–130, 1986.

[35] R.L. Mauck, C.T. Hung, and G.A. Ateshian. Modeling of neutral solute transport in a dynamically loaded porous permeable gel: implications for articular cartilage biosynthesis and tissue engineering. Journal of Biomechanical Engineering, 125(5):602–614, 2003.

[36] S.D. McCullen, C.M. Haslauer, and E.G. Loboa. Musculoskeletal mechanobiology: interpretation by external force and engineered substratum. Journal Of Biomechanics, 43(1):119–127, 2010.

[37] S. McDougall, J. Dallon, J. Sherratt, and P. Maini. Fibroblast migration and collagen deposition during dermal wound healing: mathematical modeling and clinical implications. Philosophical Transactions of the Royal Society A, 364(1843):1385–1405, 2006.

[38] A. Mobasheri, C. Csaki, A.L. Clutterbuck, M. Rahmanzadeh, and M. Shakibaei. Mesenchymal stem cells in connective tissue engineering and regenerative medicine: applications in cartilage repair and osteoarthritis therapy. Histology And Histopathologyl, 24(3):347–366, 2009.

[39] J.A. Mollenhauer. Perspectives on articular cartilage biology and osteoarthritis. Injury, 39(1):5–12, 2008.

[40] J.K. Mouw, N.D. Case, R.E. Guldberg, A.H.K. Plaas, and M.E. Levenston. Variations in matrix composition and GAG fine structure among scaffolds for cartilage tissue engineering. 13(9):828–836, 2005.

[41] V.C. Mow, G.A. Ateshian, W.M. Lai, and WY. GU. Effects of fixed charges on the stress-relaxation behavior of hydrated soft tissues in a confined compression problem. International Journal of Solids and Structures, 35(34):4945–4962, 1998.

[42] V.C. Mow and X.E. Guo. Mechano-electrochemical properties of articular cartilage: their inhomogeneities and anisotropies. Annual Review of Biomedical Engineering, 4(1):175–109, 2002.

[43] N.I. Nikolaev, B. Obradovic, H.K. Versteeg, G. Lemon, and D.J. Williams. A validated model of GAG deposition, cell distribution, and growth of tissue engineered cartilage cultured in a rotating bioreactor. Biotechnology and Bioengineering, 105(4):842–853, 2010.

[44] B. Obradovic, J.H. Meldon, L.E. Freed, and G. Vunjak-Novakovic. Glycosaminoglycan (GAG) deposition in engineered cartilage: experiments and mathematical model. American Institute of Chemical. AICh Engineers Journal , 46(9):1860–1871, 2000.

[45] L. Olsen, J.A. Sherratt, P. Maini, and F. Arnold. A mathematical model for the capillary endothelial cell-extracellular matrix interactions in wound-healing angiogenesis. Journal of Mathematics Applied in Medicine and Biology, 14(4):261–281, 1997.

[46] S.D. Olson and M.A. Haider. A level set reaction diffusion model for tissue regeneration in a cartilage-hydrogel aggregate. International Journal of Pure and Applied Mathematics, 53(3):333–353, 2009.

[47] H. Perfahl, H.M. Byrne, V. Estrella, T. Alarcon, A. Lapin, R.A. Gatenby, R.J. Gillies, M.C. Lloyc, P.K. Maini, M. Reuss, and M.R. Owen. Multiscale modeling of vascular tumor growth in 3D: the role of domain size and boundary conditions. PLoS ONE, 6(4):1–17, 2011.

[48] V. Podrazky and V. Sedmerova. Densities of collagen dehydrated by some organic solvents. Cellular and Molecular Life Sciences, 22(12):792, 1966.

[49] A.H. Reddi, J. Becerra, and J.A. Andrades. Nanomaterials and hydrogel scaffolds for articular cartilage regneration. Tissue Engineering Part B, 17(5):301–305, 2011.

[50] K.A. Rejniak, S.E. Wang, N.S. Bryce, H. Chang, B. Parvin, J. Jourquin, L. Estrada, J.W. Gray, C.L. Arteaga, A.M. Weaver, V. Quaranta, and A.R.A. Anderson. Linking changes in epithelial morphogenesis to cancer mutations using computational modeling. PLoS Computational Biology, 6(8):e1000900, 2010.

[51] S.M. Richardson, J.A. Hoyland, R. Mobasheri, C. Csaki, M. Shakibaei, and A. Mobasheri. Mesenchymal stem cells in regenerative medicine: opportunities and challenges for articular cartilage and intervertebral disc tissue engineering. Journal of Cellular Physiology, 222(1):23–32, 2010.

[52] M. Rutgers, M.J.P. van Pelt, W.J.A. Dhert, L.B. Creemers, and D.B.F. Saris. Evaluation of histological scoring systems for tissue-engineered, repaired, and osteoarthritic cartilage. Osteoarthritis and Cartilage, 18(1):12–23, 2010.

[53] A.K. Saha, J.R Mazumdar, and S.S. Kohles. Prediction of growth factor effects on engineered cartilage composition using deterministic and stochastic modeling. Annals of Biomedical Engineering, 32(6):871–879, 2004.

[54] B.C. Sengers, C.C. Donkelaar, C.W. Oomens, and F.P.T. Baaijens. Computational study of culture conditions and nutrient supply in cartilage tissue engineering. Biotechnology Progress, 21(4):1252–1261, 2005.

[55] B.G. Sengers, H.K. Heywood, D.A. Lee, C.W.J. Oomens, and D.L. Bader. Nutrient utilization by bovine articular chondrocytes: a combined experimental and theoretical approach. Journal Of Biomechanical Engineering, 127(5):758–766, 2005.

[56] B.G. Sengers, C.W.J. Oomens, and F.P.T. Baaijens. An Integrated finite element approach to mechanics, transport and biosynthesis in tissue engineering. Journal of Biomechanical Engineering, 126(1):82–91, 2004.

[57] B.G. Sengers, C.W.J. Oomens, T.Q.D. Nguyen, and D.L. Bader. Computational modeling to predict the temporal regulation of chondrocyte metabolism in response to various dynamic compression regimes. Biomechanics and Modeling in Mechanobiology, 5(2):111–122, 2006.

[58] B.G. Sengers, M. Taylor, C.P. Please, and R.O.C. Oreffo. Computational modeling of cell spreading and tissue regeneration in porous scaffolds. Biomaterials, 28(10):1926–1940, 2007.

[59] J.A. Sherratt and J.C. Dallon. Theoretical models of wound healing: past successes and future challenges. Comptes Rendus Biologies, 325(5):557–564, 2002.

[60] A. Shirinifard, J.S. Gens, B.L. Zaitlen, N.J. Poplawski, M. Swat, and J.A. Glazier. 3D Multi-cell simulation of tumor growth and angiogenesis. PLoS ONE, 4(10):1–11, 2009.

[61] B.V. Slaughter, S.S. Khurshid, O.Z. Fisher, A. Khademhosseini, and N.A. Peppas. Hydrogels in regenerative medicine. Advanced Materials, 21(32):3307–3329, 2009.

[62] K.L. Spiller, S.A. Maher, and A.M. Lowman. Hydrogels for the repair of articular cartilage defects. Tissue Engineering Part B, 17(4):281–299, 2011.

[63] B.T. Summey, R.D. Graff, T.S. Lai, C.S. Greenberg, and G.M. Lee. Tissue transglutaminase localization and activity regulation in extracellular matrix of articular cartilage. Journal of Orthopaedic Research, 20(1):76–82, 2002.

[64] D.N. Sun, W.Y. Gu, X.E. Guo, W.M. Lai, and V.C. Mow. A mixed finite element formulation of triphasic mechano-electrochemical theory for charged, hydrated biological soft tissues. International Journal for Numerical Methods in Engineering, 45(10):1375–1402, 1999.

[65] A.J. Trewenack, C.P. Please, and K.A. Landman. A continuum model for the development of tissue-engineered cartilage around a chondrocyte. Mathematical Medicine and Biology, 26(4):241–262, 2009.

[66] C. Vinatier, D. Mrugala, C. Jorgensen, J. Guicheux, and D. Noel. Cartilage engineering: a crucial combination of cells, biomaterials, and biofactors. Trends in Biotechnology, 27(5):307–314, 2009.

[67] G. Vunjak-Novakovic, B. Obradovic, I. Martin, P.M. Bursac, R. Langer, and L.E. Freed. Dynamic cell seeding of polymer scaffolds for cartilage tissue engineering. Biotechnology Progress, 14(2):193–202, 1998.

[68] J.H.C. Wang and B.P. Thampatty. An introductory review of cell mechanobiology. Biomechanics and Modeling in Mechanobiology, 5(1):1–16, 2006.

[69] C.G. Wilson, L.J. Bonassar, and S.S. Kohles. Modeling the dynamic composition of engineered cartilage. Archives of Biochemistry and Biophysics, 408(2):246–254, 2002.

[70] M. Wong and D.R. Carter. Articular cartilage functional histomorphology and mechanobiology: a research perspective. Bone, 33(1):1–13, 2003.

[71] C. Xue, A. Friedman, and C.K. Sen. A mathematical model of ischemic cutaneous wounds. Proceedings of the National Academy of Sciences, 106(39):16782–16787, 2009.

[72] T. Zhang, N. Cogan, and Q. Wang. Phase-field models for biofilms II. Simulations of biofilm-flow interaction. Communications in Computational Physics, 4(1):72–101, 2008.